

Synthesis of nanocomposite thin films and its ion irradiation induced modifications

Submitted in

Fullfillments of the requirements for the degree of

Doctor of Philosophy

by

Himanshu Sharma

ID: 2013RPH9508

Under the supervision of

Dr. Rahul Singhal



Department of Physics

MALAVIYA NATIONAL INSTITUTE OF TECHNOLOGY JAIPUR

December 2018

© Malaviya National Institute of Technology Jaipur - 2018

All Rights Reserved.

Dedicated to My Family

DECLARATION

I, **Himanshu Sharma**, declare that this thesis titled, “**Synthesis of nanocomposite thin films and its ion irradiation induced modifications**” and the work presented in it, are my own. I confirm that:

- This work was done wholly or mainly while in candidature for a research degree at this university.
- Where any part of this thesis has previously been submitted for a degree or any other qualification at this university or any other institution, this has been clearly stated.
- Where I have consulted the published work of others, this is always clearly attributed.
- Where I have quoted from the work of others, the source is always given. With the exception of such quotations, this thesis is entirely my own work.
- I have acknowledged all main sources of help.
- Where the thesis is based on work done by myself, jointly with others, I have made clear exactly what was done by others and what I have contributed myself.

Date:

Himanshu Sharma
(2013RPH9508)

CERTIFICATE

This is to certify that the thesis entitled “**Synthesis of nanocomposite thin films and its ion irradiation induced modifications**” being submitted by **Himanshu Sharma (2013RPH9508)** is a bonafide research work carried out under my supervision and guidance in fulfillment of the requirement for the award of the degree of **Doctor of Philosophy** in the **Department of Physics**, Malaviya National Institute of Technology, Jaipur, India. The matter embodied in this thesis is original and has not been submitted to any other University or Institute for the award of any other degree.

Place: Jaipur

Date:

(Dr. Rahul Singhal)

Assistant Professor

Department of Physics

MNIT Jaipur

Acknowledgement

I would first like to express my sincere gratitude and the best regards to my supervisor Dr. Rahul Singhal, for his guidance during my Ph.D. His knowledge and dedication towards the work always motivate me. He was always available to solve my problems with his kind behaviour. I am very thankful to him to encourage and support me during my journey of research.

I wish to express my sincere gratitude to Dr. Asokan Kandasami Scientist, Inter University Accelerator Centre New Delhi and Dr. D.K. Avasthi Director, Amity Institute of Nanotechnology, Noida for their consistent, valuable discussions.

I, sincerely thank the Head, Department of Physics for giving me this opportunity to work in this laboratory and also thanks all the Faculty members and Dr. Ritu Vishnoi, Department of Physics, for their suggestions during my research work and their kind support.

I express my heartiest thanks to my friends and labmates Veeresh Kumar, Shushant Kumar Singh, Trupti Sharma and Pooja (Optical material lab) for their unconditional support and making the journey memorable, Department of physics, MNIT Jaipur for their co-operation and encouragement. I would also like to thank all research scholars, Department of Physics, MNIT Jaipur, especially Dr. Yogita Kumari, Dr. Vikas Sharma, Mr. Arun Vinod, Mr. Satyaveer Singh, Mr. Mahendra Singh and Mr. Rajesh Kumar for their moral support and help.

From deep of my heart, I am thankful to my parents, and my in-laws, who always encouraged me to pursue my goals and for always being my strength to face every difficulty or challenge in my life.

I especially acknowledge the Material Research Centre, MNIT Jaipur for providing research facility and IUAC New Delhi for providing me financial assistance under the project to carry out my research work. All the faculty and staff members of the Department of Physics, MNIT, Jaipur for their support during my Ph.D.

Abstract of the thesis

In the present investigation, Ag-TiO₂ nanocomposite thin films were synthesized by RF co-sputtering with a high concentration of Ag (24%, 33%, 45%, 56% at.). The effect of Ag concentration on the phase of the host matrix was studied. The morphological, structural and optical properties of nanocomposite thin films were also studied. The band gap was tuned from 3.05 eV to 2.25 eV in Ag-TiO₂ thin films. The nanocomposite thin film was also synthesized by ion implantation technique. In this work, the formation of Ag nanoparticle in the TiO₂ matrix was observed.

Further, the nanocomposite thin films with high concentrations of Ag (45%, 56%)-TiO₂ was irradiated by 90 MeV Ni ion beam at different irradiation fluence. The SHI irradiation plays an important role for the modifications of optical and morphological properties of the thin film. For both cases (Ag 45, 56 at.%), we have reported the formation of Ag nanoparticle. The emergence of LSPR after SHI irradiation is due to increased number of nanoparticle and reduced interparticle plasmonic coupling effects act as the main reason for LSPR at such high concentration of Ag. A broad LSPR was observed in the visible region after ion irradiation. The enhancement in interparticle separation with the fluence is also discussed in this work. The results were also supported by FDTD simulation results.

RF co-sputtering deposited thin films (Ag-TiO₂) were further sequentially annealed at 200 °C, 400 °C and 600 °C for 1 hour. Optical and structural properties of these thin films were studied with annealing temperature variation. The structural modification and enhancement in crystallinity of Ag nanoparticle were reported in this work, which was not obtained by SHI irradiation technique. The silver nanoparticle agglomerate and form bigger particles. Mixed phases (anatase and rutile) of TiO₂ observed in the thermal annealing process. The combined effect of crystalline TiO₂ and silver nanoparticle size directly affect the position and intensity of LSPR. The optical and structural modification was discussed with the annealing temperature. Sublimation of Ag nanoparticle was observed for all the concentration after annealing at 600 °C.

Table of content

Declaration	i
Certificate.....	iii
Acknowledgement	v
Abstract of the thesis.....	vii
Table of content	ix
List of Tables	xiii
List of Figures	xv
List of Abbreviations	xix
Chapter One	1
Introduction.....	1
1.1 Nanoscience.....	1
1.2 Nanomaterials and nanocomposites	2
1.2.1 Concept of Nanomaterials.....	2
1.2.2 Concept of nanocomposites	4
1.2.3 Nanocomposite classification	5
1.2.4 Surface Plasmon Resonance in nanocomposite thin film.....	6
1.3 Noble metal/ Metal oxide-based nanocomposite.....	9
1.3.1 Selection of host matrix	9
1.3.2 Selection of filler.....	11
1.4 Modifications of properties of nanocomposite thin films	11
1.4.1 Swift heavy ion induced modifications.....	11
1.4.2 Thermal annealing	13
Chapter Two.....	15
Literature Review	15
2.1 Introduction	15
2.2 Literature	15
Chapter Three	27
Materials and Methods.....	27

3.1 Introduction	27
3.2 Synthesis of nanocomposite thin film	27
3.2.1 RF Magnetron sputtering	27
3.2.2 Ion implantation	29
3.3 Modifications techniques for nanocomposite thin film.....	30
3.3.1 Swift Heavy Ion Beam Irradiation	30
3.3.2 Thermal annealing	32
3.4 Characterization techniques.....	33
3.4.1 Rutherford Backscattering Spectroscopy.....	33
3.4.2 X-ray diffraction spectroscopy	35
3.4.3 UV-visible absorption spectroscopy	36
3.4.4 Fluorescence spectroscopy.....	37
3.4.5 Transmission electron microscopy	38
3.4.6 X-ray Photoelectron spectroscopy	40
3.4.7 Finite difference time domain simulation	42
Chapter Four	43
Synthesis of Ag-TiO₂ nanocomposite	43
4.1 Introduction	43
4.2 Synthesis of nanocomposite thin film by RF sputtering	43
4.2.1 Experimental detail	44
4.2.2 Composition and Structural Studies.....	45
4.2.3 Morphological Studies using HR-TEM	48
4.2.4 Optical Properties.....	50
4.2.5 X-Ray Photoelectron Spectroscopy	54
4.3 Synthesis of nanocomposite thin film by Ion implantation.....	57
4.3.1 Experimental detail	57
4.3.2 Composition and Structural Studies.....	58
4.3.3 Absorption and fluorescence spectroscopy.....	60
4.3.4 X-Ray Photo-electron Spectroscopy.....	61
4.4 Conclusion.....	64
Chapter Five	67
Modifications in Ag-TiO₂ thin film by ion irradiation	67

5.1 Introduction	67
5.2 SHI irradiation of Ag (45 at.%) -TiO_2 nanocomposite thin film.....	67
5.2.1 Experimental detail	67
5.2.2 Compositional, structural and morphological studies.....	68
5.2.3 Absorption spectroscopy and FDTD simulation.....	71
5.3 SHI irradiation of Ag (56 at.%) -TiO_2 nanocomposite thin film.....	75
5.3.1 Experimental detail	76
5.3.2 Compositional, structural and morphological studies.....	76
5.3.3 Absorption spectroscopy and FDTD simulation.....	79
5.4 Conclusions	85
Chapter Six	87
Modification in Ag-TiO_2 thin film by thermal annealing.....	87
6.1 Introduction	87
6.2 Thermal annealing of nanocomposite thin film.....	87
6.2.1 Experimental detail	87
6.2.2 Thermal annealing of Ag(24%) -TiO_2 thin film	87
6.2.3 Thermal annealing of Ag(33%) -TiO_2 thin film	90
6.2.4 Thermal annealing of Ag(45%) -TiO_2 thin film	92
6.2.5 Thermal annealing of Ag(56%) -TiO_2 thin film	95
6.3 Conclusion	98
Chapter Seven	99
Conclusion and future aspects	99
7.1 Conclusion.....	99
7.2 Future aspects	100
References.....	103

List of Tables

Table 1.	Structural characteristics of TiO ₂ crystalline phase	10
Table 2.	Lattice constant calculated from XRD.....	48
Table 3.	Bandgap value with variation of Ag content	52
Table 4.	Ti 2p XPS fitting parameters	54
Table 5.	XPS analysis for core spectra of Ti and O.....	64
Table 6.	Temperature dependence of LSPR position for all concentration.....	98

List of Figures

Fig 1.1 Classification of Nanomaterials	3
Fig 1.2 Schematic illustration for the synthesis of Nanomaterial.....	3
Fig 1.3 Chart of properties enhancement by nanocomposite in various fields.....	5
Fig 1.4 Nano structurally classified nanocomposite.....	5
Fig 1.5 Classification of Nanocomposites	6
Fig 1.6 Schematic diagram of the oscillation of electron cloud interacting with the electric vector of the electromagnetic wave.....	7
Fig 1.7 Schematic representation of plasmon oscillation for metallic sphere and shows conduction electron displacement	7
Fig 1.8 Structure of TiO ₂ phases in a ball and stick model (a) Anatase (b) Rutile	10
Fig 1.9 Stopping power in eV/A for Ni 90 MeV in TiO ₂ by SRIM program.	13
Fig 3.1 Illustration setup of RF sputtering machine	28
Fig 3.2 Schematic diagram for magnetron sputtering mechanism	28
Fig 3.3 Schematic representation of Ion implantation technique.	29
Fig 3.4 Schematic diagram of pelletron accelerator	31
Fig 3.5 Total path length R and projected range R _p representation.....	31
Fig 3.6 Schematic diagram for furnace setup used for annealing nanocomposite thin film	32
Fig 3.7 Schematic representation of experimental setup of RBS	33
Fig 3.8 Schematic of scattered nuclei energy difference with thickness in RBS	34
Fig 3.9 Schematic layout for X-ray diffraction instrument	35
Fig 3.10 Schematic representation of X-ray diffraction from sample.....	35
Fig 3.11 Layout of UV-visible absorption spectrometer.....	37
Fig 3.12 Schematic of fluorescence setup, excitation and fluorescence process diagram.....	38
Fig 3.13 TEM instrument setup block diagram.....	40
Fig 3.14 Schematic representation of XPS apparatus setup	41
Fig 3.15 Ejection of core level electron from X-ray and dependencies on binding energy	42
Fig 4.1 RBS simulation and depth profiles of TiO ₂ and Ag-TiO ₂ . The simulation showed with symbol and experimental data with the line. (i) TiO ₂ , (ii) Ag-	

24%- TiO ₂ , (iii) Ag-33%- TiO ₂ and (iv) Ag-45%- TiO ₂ (d) Ag-45%- TiO ₂ and (e) Ag-56%- TiO ₂	47
Fig 4.2 XRD pattern of TiO ₂ and Ag-TiO ₂ , showing the anatase phase and affect of Ag concentrations on its phase (i) TiO ₂ , (ii) Ag-24%- TiO ₂ ,(iii) Ag-33%- TiO ₂ and (iv) Ag-45%- TiO ₂ (v) Ag-56%- TiO ₂	48
Fig 4.3 Plan view, bright field TEM images with SAED pattern and histogram of particle size distribution. (i) Ag-24%- TiO ₂ (ii) Ag-33%- TiO ₂ (iii) Ag-45%- TiO ₂	49
Fig 4.4 Bright field images showing the effect on inter-particle separation distance with concentration of Ag (i) Ag-24%- TiO ₂ (ii) Ag-33%- TiO ₂ (iii) Ag-45%- TiO ₂ (iv) Ag-56%- TiO ₂	50
Fig 4.5 Optical absorption spectra of TiO ₂ and TiO ₂ with varying Ag concentration. (i) pure TiO ₂ (ii) Ag-24%- TiO ₂ (iii) Ag-33%- TiO ₂ (iv) Ag-45%- TiO ₂ (v) Ag-56%- TiO ₂ . In the inset is TiO ₂ absorption subtracted in others.	52
Fig 4.6 Tauc plot using the Tauc relation of obtained optical absorption spectra. (i) TiO ₂ (ii) Ag-24%- TiO ₂ , (iii) Ag-33%- TiO ₂ , and (iv) Ag-45%- TiO ₂	53
Fig 4.7 XPS (a) Full scan (b) Peak fitting of Ti 2p XPS of pure TiO ₂ and Ag (45%)-TiO ₂ thin films with inset of Ti 2p from full scan (c) O 1s XPS spectra and (d) Ag 3d spectra Ag (45%)-TiO ₂ thin films with inset of Ag 3d from full scan.....	55
Fig 4.8 Evaluated depth profiles of distribution of Ag ⁻ ions implantation in TiO ₂ relative to depth.....	59
Fig 4.9 RBS simulation of pure TiO ₂ thin film deposited on quartz substrate.....	59
Fig 4.10 XRD pattern of pristine and implanted TiO ₂ at different fluences	60
Fig 4.11 UV-visible absorption spectroscopy of TiO ₂ and implanted composite thin film.....	60
Fig 4.12 Fluorescence spectroscopy of pristine and implanted thin film fluence 3×10^{14} , 1×10^{15} , 3×10^{15} , 1×10^{16} , 3×10^{16} ions/cm ²	61
Fig 4.13 XPS of pristine thin film and implanted thin film for the fluence 3×10^{16} ions/cm ² . (a) Ti 2p core spectra, (b) O 1s core spectra (c) Ag 3d spectra for fluence 3×10^{16} ions/cm ²	63
Fig 5.1 (a) RBS of Ag (45 at.%) -TiO ₂ , simulation shown with line and experimental data with the symbol. (b) Depth profile of nanocomposite thin film.....	69

Fig 5.2 XRD of as-deposited and 90 MeV Ni ion irradiated thin film at different fluences	69
Fig 5.3 Planer view, bright field TEM images are shown in (a),(b) with SAED pattern in (e),(f) and (c),(d) show a histogram of particle size distribution .	70
Fig 5.4 Optical absorption spectra of 90 MeV Ni ion irradiation of nanocomposite thin film.....	72
Fig 5.5 fluorescence spectroscopy of pristine and irradiated thin films at different fluences	72
Fig 5.6 FDTD simulation of pristine and 3×10^{13} ions/cm ² irradiated thin film at 530 nm and absorption graph of 3×10^{13} ions/cm ² irradiated thin film.....	73
Fig 5.7 FDTD simulation of pristine and 3×10^{13} ions/cm ² irradiated thin film at 350 nm and 750 nm.....	74
Fig 5.8 (a) RBS of Ag(56%)-TiO ₂ , simulation shown with line and experimental data with symbol. (b) Depth profile of Ag(56%)-TiO ₂ nanocomposite thin film.	77
Fig 5.9 XRD of 90 MeV Ni ion irradiated thin film at different fluences.....	77
Fig 5.10 (a,b) Plan view, bright field TEM images with (e,f) SAED pattern and (c,d) histogram of particle size distribution.....	78
Fig 5.11 Bright field images showing the effect of ion irradiation on inter-particle separation	79
Fig 5.12 Optical absorption spectra of 90 MeV Ni ion irradiation of nanocomposite thin film.....	80
Fig 5.13 Distribution of electric field intensity around silver nanoparticles (a) simulation for pristine thin film (b) simulation or irradiated thin film at fluence 1×10^{13} ions/cm ² at 550 nm (c) absorption spectra from the simulation.....	82
Fig 5.14 Distribution of electric field intensity (a) simulation for the pristine thin film at 350 nm and 750 nm (b) simulation for the irradiated thin film at fluence 1×10^{13} ions/cm ² at 350 nm and 750 nm.....	83
Fig 5.15 The schematic diagram shows colour/absorption depending on nanoparticle size and inter-particle separation	83
Fig 6.1 XRD of Ag(24%)-TiO ₂ nanocomposite thin film as-deposited and annealed at 200 °C, 400 °C, 600 °C.....	88

Fig 6.2 UV-visible absorption spectroscopy of Ag(24%)-TiO ₂ nanocomposite thin film as-deposited and annealed at 200 °C, 400 °C, 600 °C.	89
Fig 6.3 XPS of Ag(24%)-TiO ₂ nanocomposite thin film as-deposited and annealed at 600 °C.	89
Fig 6.4 XRD of Ag(33%)-TiO ₂ nanocomposite thin film as-deposited and annealed at 200 °C, 400 °C, 600 °C.....	90
Fig 6.5 UV-visible absorption spectroscopy of Ag(33%)-TiO ₂ nanocomposite thin film as-deposited and annealed at 200 °C, 400 °C, 600 °C.	91
Fig 6.6 XPS of Ag(33%)-TiO ₂ nanocomposite thin film as-deposited and annealed at 600 °C.	91
Fig 6.7 XRD of Ag(45%)-TiO ₂ nanocomposite thin film of as-deposited and annealed at 200 °C, 400 °C, 600 °C.....	93
Fig 6.8 UV-visible absorption spectroscopy of Ag(45%)-TiO ₂ nanocomposite thin film as-deposited and annealed at 200 °C, 400 °C, 600 °C.	94
Fig 6.9 XPS of Ag(45%)-TiO ₂ nanocomposite thin film as-deposited and annealed at 600 °C.	94
Fig 6.10 XRD of Ag(56%)-TiO ₂ nanocomposite thin film as-deposited and annealed at 200 °C, 400 °C, 600 °C.....	96
Fig 6.11 UV-visible absorption spectroscopy of Ag (56%)-TiO ₂ nanocomposite thin film as-deposited and annealed at 200 °C, 400 °C, 600 °C.	97
Fig 6.12 XRD of Ag(56%)-TiO ₂ nanocomposite thin film of as-deposited and annealed at 200 °C, 400 °C, 600 °C.....	97

List of Abbreviations

Ag	Silver
at. %	Atomic percentage
FDTD	Finite difference time domain
HR-TEM	High-resolution Transmission electron microscope
LSPR	Localized Surface plasmon resonance
RBS	Rutherford backscattering
SAED	Selective area electron diffraction
SHI	Swift heavy ion
SPR	Surface plasmon resonance
TEM	Transmission electron microscope
TiO ₂	Titanium dioxide
UV-visible	Ultraviolet-visible
XPS	X-ray photoelectron spectroscopy
XRD	X-ray diffraction

Chapter One

Introduction

1.1 Nanoscience

Nanoscience fundamentally manages blend, representation, investigation, and exploitation of nanostructured materials. The nanomaterials are described by a dimension < 100 nm. A nanometer (nm) is one billionth of a meter or 10^{-9} m. One nanometer is around the length identical to 10 hydrogen or 5 silicon particles adjusted in a line.

An insurgency in materials science appears as analysts discover approaches to design and characterize materials at the nanometer length scale. New materials with exceptional electrical, optical, attractive and mechanical properties^{1,2} are synthesized for use in information technology, bioengineering, also, vitality and natural applications.

On the nanoscale dimensions, some physical, mechanical and chemical properties can contrast fundamentally. From the bulk to the small dimensional material, quantum properties play an essential role³⁻⁶. Crystals show the low melting point at nanometer scale and diminished lattice constants since the quantity of surface atoms or ions turns into a massive part of the aggregate number of atoms or ions and the surface energy assumes a considerable part in the thermal stability. Therefore, the properties of many materials show drastic change due to increment in the surface to volume (S/V) proportion, which is related to the decrease in material size to the nanoscale, regularly prominently affecting material performance. In any case, as nanofabrication propels proceed with these bulk properties are never again adequate to foresee performance when devices are manufactured with little basic dimensions. Nanoscience along these is the complex interdisciplinary science, nanochemistry, nanophysics, nanomaterials, nanocomposites, optoelectronics, nanobiotechnology.

Nanomaterials and nanocomposite have shown great potential in the various application due to their diverse properties⁷⁻¹⁰. The bottom-up synthesis of these materials and their potential utilization of functionalized structures show significant impact on nanoscience and nanotechnology.

1.2 Nanomaterials and nanocomposites

1.2.1 Concept of Nanomaterials

As nanomaterials show great potential in various applications in the last few decades, the size of the device based on nanotechnology decreased up to 10 nm from micrometre. The nanomaterials show dependency on size and mass of the materials¹¹⁻¹³. Reducing the size of materials results in increasing the surface to volume ratio and quantum properties of nanomaterials.

for the sphere of radius r
$$S/V = 4\pi r^2 / \left(\frac{4}{3}\pi r^3\right) = \frac{3}{r} \quad (1)$$

for a cube of side r
$$S/V = 6r^2 / (r^3) = \frac{6}{r} \quad (2)$$

So, the research and technological development aim to scale down the device size, this is called as miniaturization, which results, improvement in smaller, lighter, faster, cheaper and high-end devices with great functionality. The reduction in materials dimension directly affects its optical properties such as absorption, optical band gap, reflectance, luminescence, refractive index, and also magnetic, electronics and mechanical properties¹²⁻¹⁴. Nanomaterials have a remarkable impact from the commercial point of view, which will increase in future. Nanomaterials can occur naturally and can be produced and engineered easily. These were used commercially and can be found in sporting goods, tires, electronics, cosmetics, textiles, paints, optics, etc.

Nanomaterials Classification

The nanomaterials were classified into three categories on the basis of quantum confinement¹⁵.

- **1-Dimensional materials**

Materials having only one dimension in the order of nanometer is called 1 Dimensional material. Examples thin films (order of a nanometer), multilayers.

- **2-Dimensional materials**

Materials having only two dimensions in the order of nanometer is called 2 Dimensional materials. Examples nanotubes, nanofibers, nanowires.

- **3-Dimensional materials**

Materials having all dimension in the order of nanometer is called as 3 Dimensional materials. Examples nanoparticles, quantum dots.

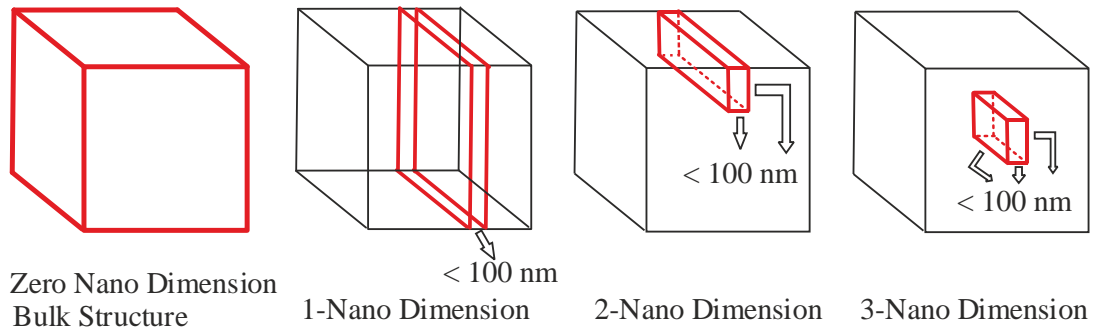


Fig 1.1 Classification of Nanomaterials

Nanomaterials Synthesis

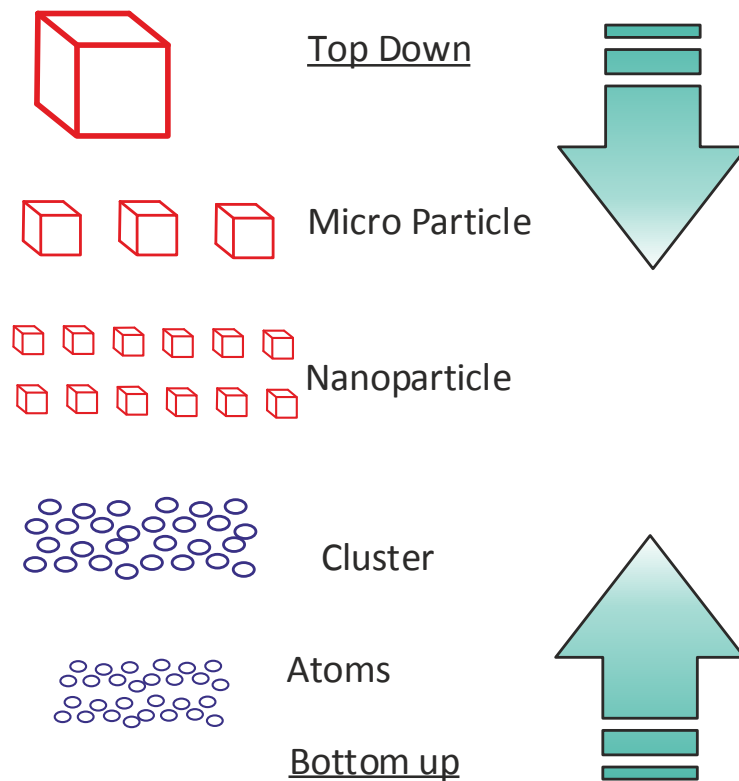


Fig 1.2 Schematic illustration for the synthesis of Nanomaterial

There are two approaches to synthesize nanomaterials bottom up and top down. Bulk solid pieces breakdown to finer pieces until they have nano dimension and assembly of

atoms or molecules together to form nanometer dimension nanomaterial. The colloidal dispersion is an example of bottom-up, and lithography is a case of the top-down method. Both these methods play a significant role in synthesizing of nanomaterials in the nanotechnology industry.

1.2.2 Concept of nanocomposites

There is a rapid development of science and technologies in the last decades, with an aim to increase the performance of materials, but materials made from one type of atom were not capable of matching the quality. This problem can be solved by mixing the two or more material in a specific manner and synthesize new material which contains performance better than single element materials. As this was proved by studies that these kinds of materials have the potential to remove the shortcomings faced before¹⁶⁻²⁰.

The nanocomposites are new kind of the composite materials which can be formed by mixing of two or more materials but have a dimension of the order of nanometer known as filler and contained in a three-dimensional substrate which is referred as a matrix. This kind of structure (nanocomposite) promotes the properties like optical, magnetic and electrical (can be multifunctional) due to increment to a high surface area to volume ratio and short diffusion distance and quantum effects. That is why these are reported as materials of this century to possess unique properties, which are not obtained in conventional composites. Nanocomposite nanotechnology is not limited to optical, magnetic and electrical only but it shows functionality in the area of mechanical properties²¹⁻²⁴ like mechanical strength, toughness, hardness, elastic modulus, improved wear resistance, friction properties. This property is also essential to work in harsh environmental condition.

As the nano-sized mass can tailor the nanocomposites properties, which has demonstrated by various interdisciplinary fields, some of the examples of these kinds of nanocomposites designs occurred naturally. Here in fig 1.3 shows the block diagram for the tuning of properties of nanocomposites in the various stream going from bulk to nano dimensions.

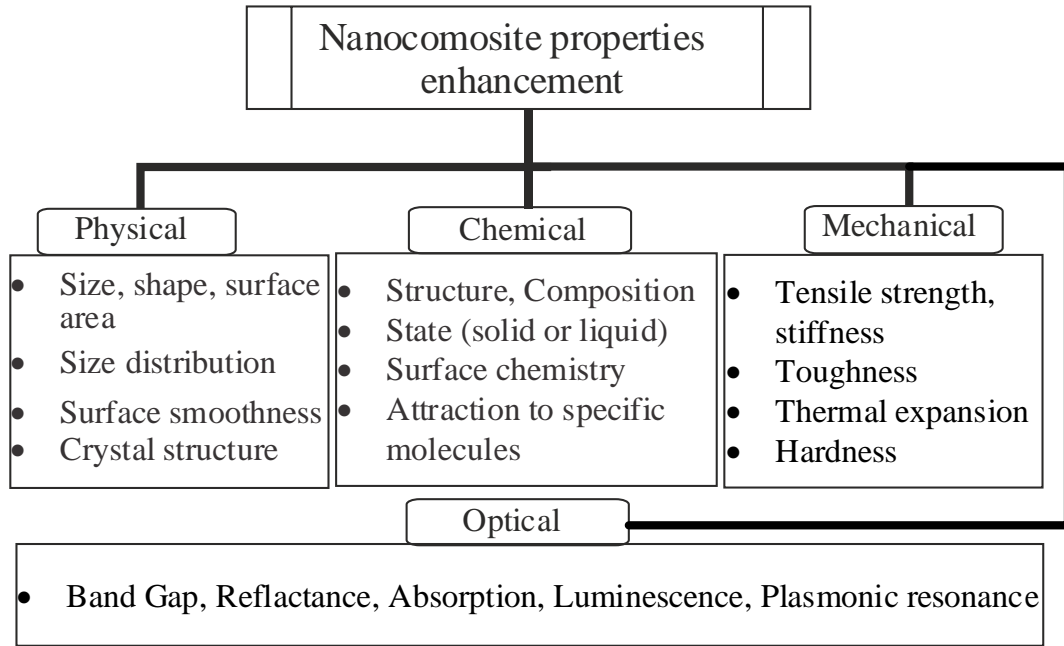


Fig 1.3 Chart of properties enhancement by nanocomposite in various fields

1.2.3 Nanocomposite classification

The nanocomposites which are being used technologically and developed consist of commonly two phases. On behalf of nanostructure they are classified into three categories as shown in fig 1.4 (a) Nanolayered composite contains layers of a thickness of nanoscale order (b) Nanofibril composite embedded in a matrix (c) Nanoparticles composed in a matrix.

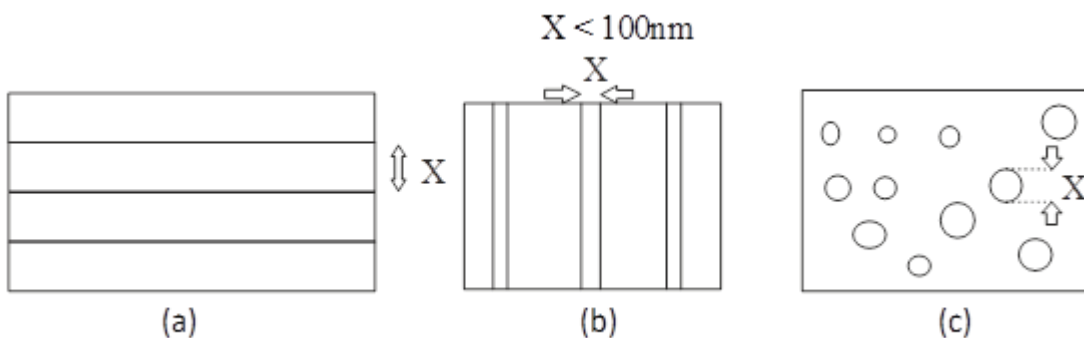


Fig 1.4 Nano structurally classified nanocomposite

Based on the type of material for matrix and filler, nanocomposites are classified in various categories as shown in Fig 1.5. Matrix and filler material can be a metal, polymer, and ceramic. Among all the nanocomposite, metal-ceramic (metal oxide) nanocomposite possess interesting properties such as non-linear optical properties,

improved mechanical strength, better tuning over electrical resistivity, high refractive index, etc. The contribution of these nanocomposites is not limited to the above properties, while they are contributing their part to the communication system^{25,26}, sensing devices^{27,28}, resistive switching²⁹, catalysis^{30,31}, solar cell³², coating³³ application also. Thus the aim of present work is based on the metal-metal oxide nanocomposite thin film to synthesize and modify the optical properties of nanocomposite thin film, especially surface plasmon resonance (SPR).

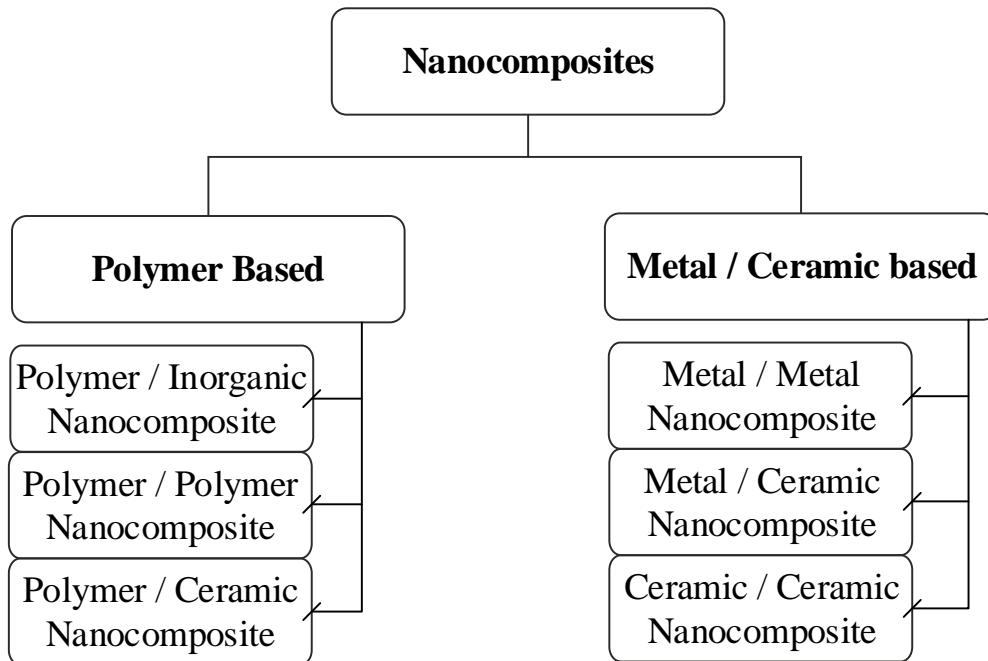


Fig 1.5 Classification of Nanocomposites

1.2.4 Surface Plasmon Resonance in nanocomposite thin film

SPR is an oscillation of electrons in conduction band with the fluence of electromagnetic wave³⁴⁻³⁶. A systematic representation is given in fig 1.6, which shows an interaction between electromagnetic wave and electron cloud. The electric force acts on the electron cloud and it moves against the direction of the electric field. Thus one side gets charged with negative and to counter that, another side was also charged with positive with the same amount and acts as an electric dipole. This electric dipole oscillates with the electric field of electromagnetic wave known as plasmon oscillation. When the oscillating frequency matches with the natural frequency of the electron cloud, the displacement is maximum. This property of metallic nanosphere make them more interesting and show the diverse application in the field of nanotechnology³⁷⁻⁴⁰.

As this plasmon resonance is bound to the finite matter (Metallic sphere), so it is also known as localized surface plasmon resonance (LSPR). SPR oscillations lead by these factors

- **Displacement of an electron in conduction band by an electric field.**
- **Restoring force due to coulomb attraction**
- **The dimension of the electron cloud is smaller than incident wave wavelength.**

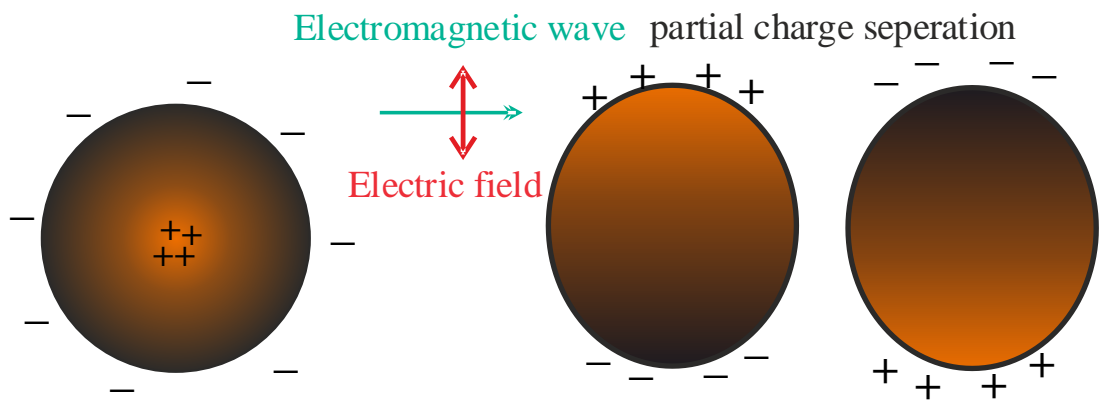


Fig 1.6 Schematic diagram of the oscillation of electron cloud interacting with the electric vector of the electromagnetic wave

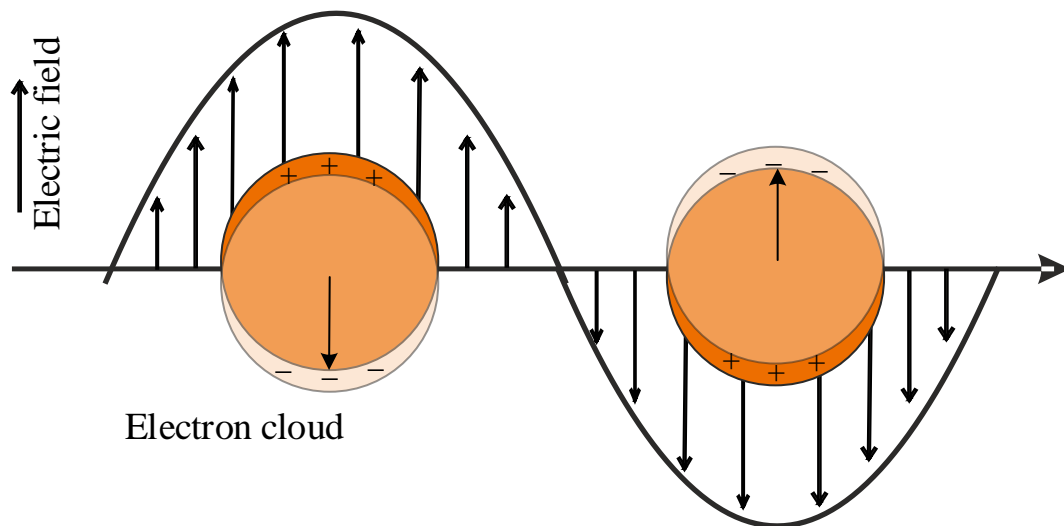


Fig 1.7 Schematic representation of plasmon oscillation for metallic sphere and shows conduction electron displacement

The electron cloud displaced by the electric field of electromagnetic wave and thus a restoring force produced due to the Coulomb attraction which results into the oscillations of electron cloud with a characteristic frequency as given in fig 1.7. This resonant frequency is called SPR frequency. During the oscillatory motion, an opposite polarization is induced in the surrounding medium which reduces the restoring force and shifts the SPR to lower frequency. Thus the SPR is affected by surrounding medium also. The factors that affect the SPR are

- **Size, shape, distribution of the metallic sphere**
- **Dielectric constant of the metallic sphere**
- **Dielectric constant of the surrounding medium**

First, Gustav Mie⁴¹ studied the interaction between metal nanoparticles and electromagnetic wave and presented the theoretical explanation of scattering dependent on the resonance of conduction electron. The relation and interaction between the metal nanoparticle and the electromagnetic wave were explained by Maxwell's classical electromagnetic theory^{41,42}. The extinction and scattering equation from Mie theory is given in equation (3-7). Discrete dipole approximation was used to understand the non-spherical metal nanoparticles with varying the surrounding medium dielectric constant. Several studies have been done on absorption and scattering of the electromagnetic wave. Some features of this phenomenon are given here:

- Absorption and scattering are the two processes occurred when electromagnetic wave reacts with the metallic sphere. For smaller size nanoparticles, absorption dominates and for larger size particles, scattering dominates.
- Smaller particle interacting with an electromagnetic waveforms dipole charge distribution, but for the case of large particle charge distribution is non-homogenous.
- Electronic transition due to the interaction with an electromagnetic wave is inter-band and intra-band. The energy required for the inter-band lies in the UV region whereas for the intra-band transition the energy required lies in the visible or NIR region. This intra-band transition leads to the formation of free electrons.

$$Q_{ext} = \frac{2}{x^2} \sum_{n=1}^{\infty} (2n + 1) \text{Re}[a_n + b_n] \quad (3)$$

$$Q_{sca} = \frac{2}{x^2} \sum_{n=1}^{\infty} (2n+1) [a^2 + b^2] \quad (4)$$

$$Q_{abs} = Q_{ext} - Q_{sca} \quad (5)$$

$$a_n = \frac{m\psi_n(mx)\psi'_n(x) - \psi_n(x)\psi'_n(mx)}{m\psi_n(mx)\xi'_n(x) - \psi_n(x)\xi'_n(mx)} \quad (6)$$

$$b_n = \frac{m\psi_n(mx)\psi'_n(x) - \psi_n(x)\psi'_n(mx)}{m\psi_n(mx)\xi'_n(x) - \psi_n(x)\xi'_n(mx)} \quad (7)$$

Where m = Ratio of refractive index of sphere n and to the surrounding medium n_m

x = size parameter $2\pi nR/\lambda$

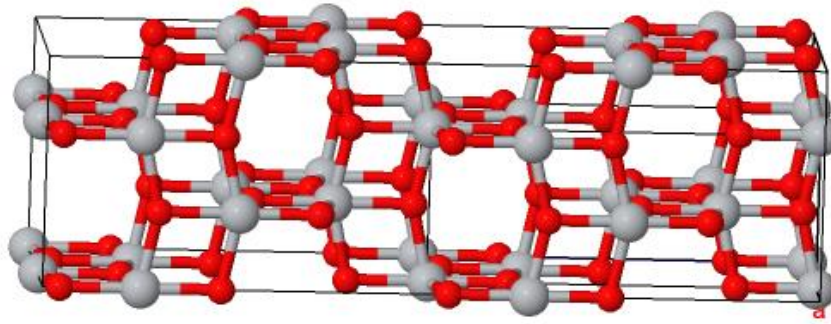
ψ_n, ξ_n = Riccati- Bessel function

1.3 Noble metal/ Metal oxide-based nanocomposite

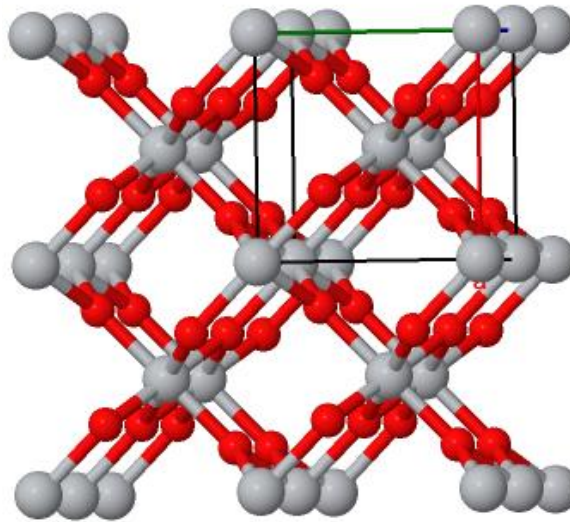
Nanocomposite based on Noble metal / Metal oxide have shown high potential during the last decades. The properties of the nanocomposite material depend on both filler and matrix. The less reactivity and optical properties of noble metal nanoparticles show a remarkable presence in the Plasmonic resonance field. Also, there is an advantage for choosing metal oxide as a matrix because they offer wide band gap, excellent chemical and mechanical stability in the environment and easy synthesizable.

1.3.1 Selection of host matrix

The host matrix should be chemically and mechanically stable, environmentally compatible and should be multifaceted in the application. Titanium dioxide (TiO_2) have all these properties⁴³⁻⁴⁸ and besides this, it shows improved properties such as chemical reactivity at nanoscale regions. From the past few decades, TiO_2 shows the potential application in various field such as solar cell⁴⁹⁻⁵¹, hydrogen generation from water^{52,53}, biomedical implant^{54,55}, catalysis^{56,57}, pigment⁵⁸, UV absorber, etc. TiO_2 shows remarkable presence in optical properties also. The physiochemical of TiO_2 depends on the crystal phase, defects and crystallinity etc. By tuning its morphology by synthesis process, one can easily control the properties of TiO_2 . These properties of TiO_2 can modify the optical properties like SPR and cause the shift in the absorption spectrum. Mainly there are two polymorphs of TiO_2 , the anatase and the rutile phase, which have a band gap of 3.2 eV and 3.0 eV⁵⁹ respectively. The anatase phase reported more active than rutile as it shows high reduction potential and low recombination rate of electron-



(a)



(b)

Fig 1.8 Structure of TiO_2 phases in a ball and stick model (a) Anatase (b) Rutile

Table 1. Structural characteristics of the TiO_2 crystalline phase

Phase	Rutile	Anatase
Crystal System	Tetragonal	Tetragonal
Space Group	P42/mnm	I41/amd
a (Å)	4.59	3.78
b (Å)	4.59	3.78
c (Å)	2.95	9.51
α (°)	90	90
β (°)	90	90
γ (°)	90	90
Density (g/cm^3)	4.24	3.89

hole pair^{59,60}. The benefits of wide band gap are that it absorbs UV radiation and allow visible radiation to pass. These properties made TiO₂ more functional with noble metal nanoparticles to function in the visible region. The decrement in electron-hole recombination rate has been observed, due to the interaction between noble metal nanoparticles and TiO₂.

1.3.2 Selection of filler

Noble metal nanoparticles show great potential in the application and attract the attention of their extraordinary properties. The optical properties of noble metal nanoparticles can be modified by altering their shape, size and surrounding environment^{61,62}. Silver nanomaterials are the most promising materials with TiO₂ for the nanocomposite synthesis due to its low cost and high intensity in LSPR, which is beneficial for visible region applications. Silver has been widely used with TiO₂ for photocatalysis^{63,64}, DSSC^{65,66}, Antibacterial^{67,68} and other applications. It also shows the capability for improving the charge separation as silver and gold show mostly similar properties, but silver nanoparticles show high efficiency for plasmonic excitation, which leads silver nanoparticles to increment in properties such as catalysis, magnetic, optical, electrical conductivity, antibacterial over gold nanoparticles. Among noble metal, Ag is the only one metal to cover the whole visible region for surface plasmon resonance and silver also has the absorption coefficient greater than its geometrical cross-section⁶⁹. This increases the effective absorption in the vast region of wavelength.

1.4 Modifications of properties of nanocomposite thin films

Further, the properties of metal/metal oxide nanocomposite can be improved by various techniques as Ion-irradiation, thermal treatment.

1.4.1 Swift heavy ion induced modifications

Energetic ion beam plays an important role in materials science for the modification and tuning of properties of materials⁷⁰. As the energetic ion passes through the materials, they losses their energy by the interaction between the energetic ion and the target material. This sharing of energy with the target material is the primary factor for the modification in properties of the material. This energy exchange depends on the

materials, ion energy, fluence and ion species⁷¹. The energetic ions can be classified into two categories based on energy (i) low energy and (ii) high energy. Low energy ions have energy up to few hundreds KeV energy which is used to implant ions in the target materials. High energy ions have energy greater than 1MeV/nucleon with velocity equivalent to Bohr velocity, called as swift heavy ions (SHI). The beauty of swift heavy ion beam is its localized high energy density which is confined in volume and this provides better results than thermal annealing. The tuning of optical, mechanical, structural, chemical, magnetic properties of target materials depends on the energy dissipated into the material by SHI ion. So one can achieve the desired modification by selecting the particular ion and its energy⁷¹.

The energy loss mechanism is classified by two main process

(i) Nuclear energy loss S_n

- Whole energy is transferred to the atom
- It dominates at low energy 10 keV/amu
- The order of S_n is few eV/nm to few keV/nm

(ii) Electronic energy loss (S_e).

- Ion causes the excitation and ionization of an atom
- Energy transferred by electron-phonon interaction
- Dominates at High energy 100 keV/amu
- The order of S_e is few eV/nm to tens of keV/nm

Both energy loss S_e and S_n depend on the mass and energy of ion and target materials. Different ions losses different energy in the materials. The energy loss ΔE in a given path Δx is given by $\Delta E/\Delta x$ ($\Delta x \rightarrow 0$), which is called stopping power S . The stopping power is equal to both sums of energy losses.

$$S = -\frac{1}{\rho} \frac{dE}{dx} = S_e + S_n \quad (8)$$

Where ρ = atomic density in the material

There are three regions in the curve given in figure 1.9. The first region is low energy region (~1 keV/amu), where S_n dominates over S_e . Within this range, the ions lose their energy by collision with the target atom. As a result, the atoms were displaced and ion trajectory changes with each collision. In the second region, electronic energy loss increases with increasing the energy and reaches the maximum and energy is proportional to \sqrt{E} . The velocity of ions having such a high energy is comparable to the

Bohr velocity of orbital electron and excitation and ionization of the target atom take place. In the third region, electronic energy loss decreases with the energy and it is inversely proportional to E .

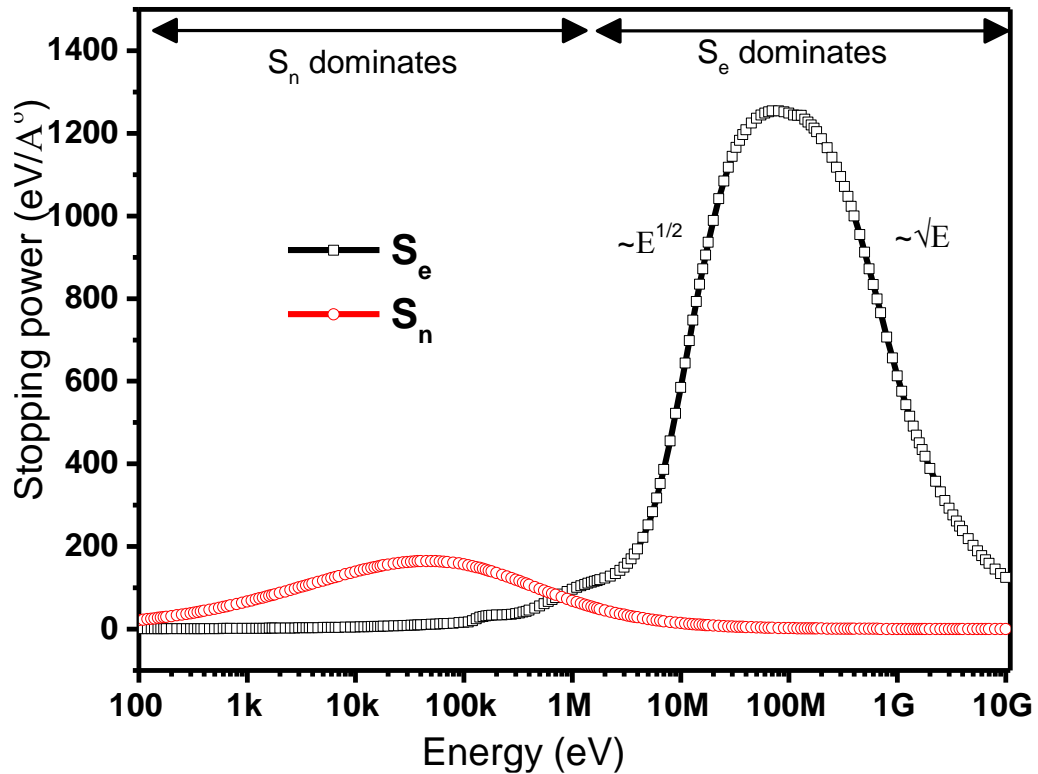


Fig 1.9 Stopping power in eV/A for Ni 90 MeV in TiO₂ by SRIM program.

The collisions and energy exchange between ions and target atoms are purely random, and the energy loss mechanism is statistical. All the ions have the different projectile range and overall it is distributed over a broad energy range. The distribution of ion along its path is called as longitudinal straggling. As the ion trajectory deviated while interacting with the target atom, straggling in a lateral direction occurs known as lateral straggling.

1.4.2 Thermal annealing

In the thermal annealing process, direct heat treatment is given to the target material in an ambient medium. This kind of heat treatment modifies the properties of the material. The main factors affecting the modifications are heating temperature, ramp rate, annealing environment, and heating time. In the case of nanocomposite thin film, thermal annealing also provide excellent control over optical and electrical properties. Thermal annealing process plays an important role in removing defects in ion-implanted materials. In this thesis, the nanocomposite thin films were thermally

annealed and also irradiated with SHI. Further, the modifications in the optical, structural and electrical properties of nanocomposite thin films occurred by both the treatments were compared.

Swift heavy ion irradiation has proved to produced modifications in TiO_2 by creating changes in stoichiometric and defects. This modification directly affects the optical properties of nanocomposite thin film and provide excellent control over properties. Whereas in the thermal annealing process, it provides excellent control over phase transformation. For the nanocomposite thin film, one can select the tool from SHI irradiation and thermal annealing to obtain the desired modifications.

Chapter Two

Literature Review

2.1 Introduction

The nanocomposite thin films have been attracted by their optical properties to be used as potential application. Both filler material and host matrix play an important role in its optical and structural properties. Here silver (Ag) is selected as filler material and Titanium Dioxide (TiO₂) as host matrix. Post-synthesis treatment by swift heavy ion beam irradiation and thermal annealing modifies the optical and structural properties. Brief literature on the selection of material, nanocomposite thin film synthesis and modification of structural and optical properties are presented here.

2.2 Literature

The Ag-TiO₂ and Au-TiO₂ nanocomposite thin film show attractive results for the photocatalytic and antibacterial properties. This photocatalysis process was governed by LSPR which shows more importance and application of nanocomposite thin film in the biomedical fields and dye degradation. Prakash *et al.*⁷² report the synthesis of Ag-TiO₂ nanocomposite for optical SERS and antibacterial properties. Uniform Ag nanoparticle distribution has been reported. They have reported the enhancement in LSPR due to the silver nanoparticle, which reduced the recombination rate of the electron-hole pair and shows a potential application for antibacterial and photocatalysis. The reduced recombination rate was supported by a decrement in PL intensity. Absorption band appears between 400 to 800 nm while increasing the concentration of silver; this confirms the presence of silver nanoparticle. The antibacterial property shown against the bacterium *Staphylococcus aureus* and further discussed the killing action of bacteria. The same photocatalysis properties for Au-TiO₂ was reported by Lin *et al.*⁷⁴ which show the LSPR role in Au/TiO₂ photocatalysis system for UV-visible light irradiation. They have been demonstrated the pros and cons of LSPR. The thin films were prepared by using doctor blade on ITO substrate. The results show that the gold is in metallic form and also an LSPR was observed at 536 nm. They also explained the charge transfer mechanism between nanoparticle and TiO₂ during LSPR. The gold nanoparticle has enough energy to transfer the electron to TiO₂

and Au/TiO₂ shows better photocatalytic performance in mixed (UV and green light) irradiation. Sangpour *et al.*⁸¹ studied the nanocomposite thin film containing Au, Ag Cu in TiO₂ matrix. They have investigated the effect of metal nanoparticles adding to the TiO₂ matrix in comparison with pure TiO₂. The thin films were prepared by reactive RF magnetron co-sputtering. 1 mm pieces of metal were stuck symmetrically to the surface of the target TiO₂. After the inclusion of different metal in TiO₂ the photocatalysis has significantly improved. These metal nanoparticles inhibit the recombination rate electron and hole. Thus this property plays an important role in photocatalytic enhancement. Copper nanoparticles and Au nanoparticles in shows markedly photocatalysis up to 96% of Methyl Blue. Ti³⁺ chemical state formed in Cu contained thin film which shows the phase of Ti₂O₃. They also reported that the average roughness of nanocomposite thin film was improved after photocatalysis.

For the photocatalytic application, Uddin *et al.*⁸² studied the coating of Au/TiO₂ thin films on cotton textile fibres. The pure cotton fibre of 10-15 μm coated with Au/TiO₂ by sol-gel method and chemical treatment. For photocatalysis, methyl blue has been used. They revealed that the cotton fibre coated with Au/TiO₂ shows more active for the degradation of methyl blue. They give two explanation for this more activeness of Au/TiO₂. One is light absorbed by gold nanoparticle form visible region transferred to the TiO₂ by excitation of the electron. The second one is the trapping of an electron by metal nanoparticles, which results in increasing the lifetime and stability of excited electron. Thus this results in reducing the recombination rate of electron and hole and enhancement in photocatalysis properties. They also show great stability towards washing cycles.

In the biomedical field, Ahmed *et al.*⁷⁶ studied the adsorption of β-amyloid on Ag-TiO₂ thin films. This β-amyloid involved in the Alzheimer disease. Changes in the structure of this compound were reported. The Ag-TiO₂ thin films were synthesized by unbalanced RF magnetron co-sputtering technique. They reported that the immobilized Ag nanoparticle was protected by Ag-TiO₂ nanocomposite thin film for a more extended time while in contact with the solution. Irradiated these thin film with the UV light to conformal changes in the β-amyloid which was suggested due to the photocatalytic mechanism. These changes were monitored by Raman spectra and XPS. Further, they reported that the potential dangerous β-amyloid contamination could be self-cleaned by the UV illumination of Ag-TiO₂ surface. Similar results were obtained

by Ahmed *et al.*⁷⁸ who again studied the photocatalytic degradation of human serum 'albumin' on TiO₂ and Ag-TiO₂. The TiO₂ and Ag (4.7 at. %)-TiO₂ thin films were prepared by the RF magnetron sputtering and photo-reduction of Ag into TiO₂ respectively. These thin films were annealed for 3 hr at 430°C which results to form an anatase phase only. The silver was in metallic form. The shifting of the amide III to higher wavelength was caused by increasing the atomic ratio of silver. They reported that photocatalytic activity confirmation through a reduction in α -helices mode in the amide I band. The photocatalysis improved by the inclusion of silver in TiO₂. Xu *et al.*⁸³ studied the Au(1-4 wt. %)-TiO₂ nanocomposite for photocatalytic activity on human colon carcinoma LoVo cells which was produced by cancerous cell. This study shows the degradation of those cells. The thin films were deposited by precipitation method. The inclusion of Au in TiO₂ affects the photocatalytic efficiency and Au 2 wt% was reported most active for photocatalysis. They have given the mechanism of photocatalytic activity, which was explained by the transfer of an electron from TiO₂ to Au nanoparticle. This reduced the recombination rate of electron-hole pair and enhancement in photocatalytic efficiency observed.

In the last decade's modification in the plasmonics properties were reported. The effect of matrix on shape, size and distribution was studied. The effect of filler material on matrix structure was also discussed. Among them Borges *et al.*⁷³ studied the gold nanoparticles in TiO₂ and Al₂O₃ matrix. They also studied the post-annealing heat treat affect the optical properties. The Au nanoparticles in Al₂O₃ shows LSPR at 530 nm. The transmittance remains the same for the annealing temperature between 400°C and 800°C. The agglomeration of particles is random. The LSPR for Au-TiO₂ shows redshift as the annealing temperature increases. That was explained by an increment in crystallinity of TiO₂. It becomes crystalline in anatase phase from amorphous but for Al₂O₃, its crystallinity not affected by much with the annealing. Improvement in crystallinity affects the refractive index of host matrix. They have revealed that there was an influence on the nanoparticle size, shape and distribution by dielectric environment, which directly affects its optical and mechanical properties. Gültekin⁷⁵ revealed the effects of inclusion of Au nanoparticle in TiO₂ on its optical and structural properties. The Au-TiO₂ nanocomposite thin film was prepared by the chemical process. The concentration of Au was (10 at.%, 20 at.%, 30 at.%, 40 at.%, 50 at.%). They have reported the increment in the band gap, on increasing the concentration of

Au. The band gap was increased from 3.74 eV to 3.89 eV. This increment is explained by Burstein-Moss (BM) effect; it shows occupation of the conduction band in lowest states and only the transition to above these level were allowed. The increment in average surface roughness and grain size was reported. Viana *et al.*⁷⁷ synthesized the amorphous and crystalline Ag-TiO₂ thin films by the sol-gel process (dip coating) followed by thermal annealing for 1hr at 100°C and 400°C. To obtain amorphous and crystalline phase rapid and slow cooling rate were used. They studied the effect of Ag concentration on the phase of the matrix TiO₂. They also reported the effect of Ag concentration on plasmonic properties. The Ag/Ti concentration was varied from 1:6 to 1:100. They discussed the growth and segregation of silver nanoparticles, which was affected by treatment temperature and cooling rate. Their results suggest the migration of silver nanoparticles to the surface without crystallization. Redshift has been reported by them with increasing the concentration of silver. The HR-TEM images show the interface region between Ag nanoparticle and TiO₂ matrix, which is essential to heighten the nanocomposite properties. Torrell *et al.*⁷⁹ studied that the tuning of the surface plasmon resonance in Au nanoparticle by altering the nanoparticle shape size and the refractive index of the host matrix. The thin film of Au (12 at.%) -TiO₂ was prepared by reactive magnetron sputtering at 150°C. The thin films were annealed up to 700°C and optical transmittance was measured to mark the surface plasmon resonance. From this, it can be seen that redshift has been observed which was due to the change in the phase composition of host matrix. They have shown the comparison between calculated and experimental spectra and finally concluded that surface plasmon resonance can be tuned by thermal annealing treatment. Affect of concentration was studied by Torrell *et al.*⁸⁰, who explore the effects of gold nanoparticle (10 at.%, 20 at.%, 30 at.%) doped in amorphous TiO₂. This nanocomposite the films were prepared by DC reactive magnetron sputtering. These were thermally annealed significant changes were observed. They report the Au (20 at.%) -TiO₂ for most promising changes. The change in colour was obtained while increasing in cluster size from 2 to 17 nm. Above this size, it showed a golden colour. Then Au (10 at.%) is upper limit to SPR behaviour. The growth of Au nanoparticles was observed by annealing treatment. Most significant changes observed for annealing temperature 500-600°C with grain size 10 nm. In plasmonics phenomenon of transfer of charge was very important this was revealed by Tian *et al.*⁸⁴ which explain the separation of charge at gold nanoparticle and TiO₂ interface. They reveal that charge separation took place by

electron transfer from gold nanoparticle to TiO₂. Gold nanoparticles absorbed the visible region light of a certain wavelength and the gold nanoparticle goes in an excited state. Then the excited electron from Au nanoparticle transferred or injected to TiO₂ bulk. The thin film of pure and Au-TiO₂ was prepared by sol-gel method. The gold was in metallic form. They also show that this Au-TiO₂ system can show the oxidation of ethanol and methanol at the expenses of O₂. This can be potentially used in the photovoltaic fuel cell; one can obtain photocurrents with alcohol and O₂.

In the above literature, Xu *et al.*⁸³ Tian *et al.*⁸⁴ Uddin *et al.*⁸² well discussed the charge transfer between the noble metal and matrix TiO₂. We have found the RF co-sputtering method as the best-reported method for the preparation of nanocomposite thin film. Also, Gültekin⁷⁵ studied the high concentration of Au in the matrix of TiO₂ which was (10 at.%, 20 at.%, 30 at.%, 40 at.%, 50 at.%) but for Ag, it has not been studied for its high concentration in TiO₂.

In the last few decades, many materials have been used for the synthesis of nanocomposite thin film. The filler material and host materials decide the optical, structural and morphological properties of thin film. In our literature survey, the most published article was based on the material Ag-TiO₂, Au-TiO₂. The optical properties of this material are interesting as these filler material are noble metal and show SPR in the visible region. The TiO₂ matrix is also interesting because of its band gap it allows passage of visible region light and blocks UV. Various concentration of noble metal Ag and Au were deposited in the TiO₂ matrix. The approx concentration is up to 25 at.% for Ag and 40 at.% for Au. High concentration of Ag above 40 at.% in TiO₂ is not studied. For Ag and Au in TiO₂ matrix enhancement in optical and structural properties were reported. High concentration of filler metal has the ability to show the enhanced absorption in the visible region, as the intensity of absorption by nanoparticle is also dependent on the concentration. More the concentration the absorption will be more.

For the synthesis of nanocomposite thin film ion implantation is another technique. Hou *et al.*⁸⁵, Xu *et al.*⁸⁶, Stepanov⁸⁷, Chang *et al.*⁸⁸. studied the implantation of Ag in TiO₂ matrix. Hou *et al.*⁸⁵ synthesized the Ag-TiO₂ nanocomposite thin film by ion implantation of Ag 40keV in TiO₂ at different dose. Further, they used these films to test their antibacterial ability for Escherichia coli and photocatalytic degradation for methyl orange. The activity of implanted nanocomposite thin film increased with the dose of Ag for a certain range. Through DFT DOS analysis they have shown that the

inclusion of Ag shows new electronic energy states, which was due to Ag 4d states. The impurity level increased the absorption. Thus the band gap decreased. The illumination gets the electron excited for valance band to impurity level and then the electron is transferred to the conduction band of TiO₂. The impurity level increased the electron-hole separation. Thus the enhancement in photocatalytic and antibacterial activity has been observed. Xu *et al.*⁸⁶ studied the synthesis of nanocomposite thin film by implantation Ag 30 keV in TiO₂ thin film, which was followed by thermal annealing. They have reported the formation of Ag₂O after Ag implantation. These thin films were used for photocatalysis using methyl blue, which show highest photocatalytic efficiency for the dose 3×10^{16} ions/cm², which is 1.4 times faster than pure TiO₂ thin film. The reason behind the improvement in catalytic activity is given that Ag₂O have a band gap of 1.2 eV and TiO₂ have 3.2 eV. So their composite show bandgap between the range 1.2 to 3.2 eV. The improvement was also explained by electronic structures of Ag⁺, its presence improve the efficiency in separating the electron-hole pair. This results in a reduction of recombination rate. At optimal Ag⁺ concentration the photocatalytic is maximum, but for more concentration, there is an increment in the defects which act as recombination centre of electron and hole. Stepanov⁸⁷ studied the modification in TiO₂ by ion implantation. In this, it has been shown that ion implantation is a successful technique for modification in various fields such as magnetic data storage, nano-catalyst and optics. TiO₂ implanted with noble metal enhance the plasmonic and optical properties. Chang *et al.*⁸⁸ studied the optical properties of Ag 40 KeV implantation in TiO₂ thin film. After implantation, no peaks of silver oxide or metallic silver were observed. This process includes the aggregation due to near-surface sintering and increasing in roughness. Strong photoluminescence and increased in absorption has been observed, which was beneficial for TiO₂ based applications. The intensity of PL and absorption were affected by Ag dose. This enhancement is due to the strong capability for formation of a compound of Ag implantation. The above Ag ion implanted thin film shows great potential for various application, but in all the cases a clear LSPR was not reported. That's why it promotes us to modify the plasmonics properties of nanocomposite thin film and to obtain the LSPR in visible region as the oxidation of Ag was reported in all cases.

Ion implantation was also a good technique to synthesize the nanocomposite thin film. But from the literature, the absorption of nanocomposite thin film does not

show any LSPR peak in the visible region. After implantation of Ag ion with an energy range between 20 keV to 60 keV in anatase and rutile phase thin film there is an increment of absorption in the whole visible region. The formation of Ag nanoparticle was shown in the TiO₂ matrix but there was no sign of LSPR. The region may be due to the heat required to agglomeration was not delivered to the atoms of Ag. So here we have chosen the slightly high energy of Ag (120 keV) for implantation. It was expected that at this energy the local aggregation of nanoparticle would be accelerated by the thermal energy provided by nuclear energy loss nearby surface.

Synthesis of nanocomposite thin film is quite easy but to get the desired results at high concentration is not easy. So the as-deposited nanocomposite thin films need modification to make use for an application. The modifications of nanocomposite thin film were done by both SHI irradiation and thermal annealing. Modification by SHI beam was reported by Verma *et al.*⁸⁹, Chakravadhanula *et al.*⁹⁰, Rath *et al.*⁹¹, Chakravadhanula *et al.*⁹², Mishra *et al.*⁹³. Verma *et al.*⁸⁹ studied the ion beam irradiation on Au/TiO₂ nanocomposite for photoelectrochemical splitting of water. Au/TiO₂ nanocomposites were irradiated by 500 KeV Ar²⁺ at fluences 1×10¹⁶, 3×10¹⁶, 1×10¹⁷ ions/cm². They reveal the study of nuclear energy deposition on optical and structural properties. Decrement in band gap was observed from 3.0 eV to 2.8 eV for 1×10¹⁶ ions/cm². Enhancement in photocurrent density was observed and it offers three times for nanocomposite. The increment in efficiency was explained by transferring of electron from TiO₂ to Au. The photoelectrochemical, optical and structural properties were affected by ion beam irradiation. They report the low fluence of Au/TiO₂ nanocomposite to achieve maximum efficiency. Chakravadhanula *et al.*⁹⁰ explore the study of modification of optical and structural properties by swift heavy ion irradiation (100 MeV Ag⁸⁺) in Au(7-50%)-TiO₂ and Ag(15-47%)-TiO₂ nanocomposite thin film. Au-TiO₂ and Ag-TiO₂ nanocomposite thin films were synthesized by co-sputtering technique. Growth in nanoparticle was observed for both Au and Ag while increasing their concentration. Au(15%)-TiO₂ and Ag(15%)-TiO₂ was irradiated and analyzed by its TEM images, in which growth in Au nanoparticle size reported from 2 nm to 14 nm. For Ag nanoparticle, the size was reported increased from 2 to 26 nm. This increment in particle size was explained by agglomeration of nearby particle and the transfer of thermal energy by electronic energy loss. A redshift of LSPR peak by 35 nm (7%), 60nm (15%) was observed for Au(7,15%)-TiO₂. For Ag(13,27%)-TiO₂ the redshift was observed by value 45 nm and 75 nm respectively. This shift confirmed the increment

in particle size. Formation of TiO in Ag-TiO₂ nanocomposite thin film was also reported. They also report the in-situ thermal annealing SAED pattern results, which report the growth of nanoparticles by Ostwald ripening. Crystallization of TiO₂ takes place after annealing. Rath *et al.*⁹¹ studied the thermal annealing (400 °C-1000 °C) and SHI irradiation (200 MeV Ag) effect on TiO₂ thin film synthesized by a sol-gel spin coating method. XRD reveals the phase transformation of anatase to rutile as the annealing temperature was increased. A complete transformation was reported at 1000 °C. These results were also supported by Raman spectra. The thin film annealed at 1000 °C was irradiated. The increment in rutile was reported which was strongly supported by Raman spectra. The growth mechanism of anatase and rutile phase during thermal annealing was also explained by grain boundaries. They reported that unlike thermal annealing, SHI irradiation was able to suppress the anatase phase at fluence 3×10^{12} ions/cm². They have used the thermal spike model to explain the complete transformation to rutile, which transfers the energy from inside of the grains of anatase phase rather than from grain boundaries. Chakravadhanula *et al.*⁹² present work based on modification by swift heavy ion irradiation. They reported that the irradiation of Ag-TiO₂ nanocomposite thin film (35 nm) with silver volume fraction (10-40%) by 100 MeV Ag⁸⁺ ion beam results in the formation of single crystalline TiO. They found this single crystalline conversion for the fluence 1×10^{13} ions/cm² for the sample with 13% MVF Ag. Mishra *et al.*⁹³ studied the modification by 90 MeV Ni ion beam irradiation of Au nanoparticles in a silica matrix. They have reported the growth of Au nanoparticle from 4 nm to 9 nm at fluence 1×10^{14} ions/cm². The SPR was obtained at 520 nm. The growth in nanoparticle was supported by an absorption graph, where they report the redshift of 22 nm by ion irradiation. This growth was further explained by the thermal spike model, which reports diffusion of Au atoms to form nanoparticle, which leads to the ripening of nanoparticle to form a bigger one. They showed ion irradiation as a useful tool for the modification of optical properties.

Thermal annealing was also provided better results for the modification of nanocomposite thin films. This was studied by Borges *et al.*⁹⁴, Kumar *et al.*⁹⁵, Laruinaz *et al.*⁹⁶, Adochite *et al.*⁹⁷, Torrell *et al.*⁹⁸, Torrell *et al.*⁹⁹. Borges *et al.*⁹⁴ explore the modification of structural properties of Au-TiO₂ nanocomposite thin films by the concentration of Ag and thermal annealing. They have deposited nanocomposite thin film co-sputtering with the variation of Au concentration from 2 at.% to 25 at.%. thin films were annealed in the range 200 °C to 800 °C. During annealing, the

microstructural properties of Au were affected and crystallization of TiO₂ was also reported. They have reported the clustering of Ag at high temperatures (> 500 °C) for Au 2 at.%, whereas for higher concentration (6,11,15,24 at.%) clustering was reported at 200 °C. The increment in cluster size was reported by 3 to 5 times for increasing the Au concentration value. Anatase phase of TiO₂ also appeared at low temperature, but at high temperature (700 °C, 800 °C) mixed phase of anatase and rutile was reported. This study revealed that the size and distribution of Au nanoparticle strongly depend on the concentration of Au and annealing temperature. As these feature affecting the morphology, so these are the key to tuning the LSPR properties. Kumar *et al.*⁹⁵ explore the plasmonic bleaching in Ag-TiO₂ nanocomposite thin film by thermal annealing at 450 °C. They also show the effect of thermal annealing on plasmonic properties. The composite thin film was synthesized by atom beam co-sputtering. The concentration of Ag was (1%,2%,5%). The average particle size was 7.4, 5.1 and 9 nm, which were uniformly dispersed in TiO₂. A redshift has been observed by value 21 nm from 453 nm to 474 nm which was justified by an increment in Ag concentration. They have reported the bleaching at 450 °C which was explained because of diffusing out of composite thin film or dissociation of Ag particle in atomic form. Laruinaz *et al.*⁹⁶ studied the Au(5 at.%) -TiO₂ nanocomposite thin films, which were deposited by magnetron co-sputtering. These were annealed in a vacuum furnace in the range 200 °C to 800 °C. Inhomogeneous distribution of nanoparticles was reported. Formation of gold nanoparticle was confirmed at 400 °C by low-frequency Raman scattering and TEM results. Further, they confirmed the crystallization of TiO₂ as anatase. The increment in the concentration of gold was observed at the surface and near the film substrate interface after annealing at 800 °C. The growth of nanoparticle was reported by Ostwald ripening which starts at a temperature 400 °C and size increases with increasing the annealing temperature. They show that the crystallization of matrix TiO₂ plays an important role in gold diffusion. Adochite *et al.*⁹⁷ explore the annealing treatment influence on Ag (at.8%) -TiO₂ nanocomposite thin film properties. These thin films were prepared by magnetron co-sputtering. Thin films were annealed in the temperature range of 200 °C to 600 °C. The amorphous structure of the matrix allows silver to agglomerate and form a bigger particle. The nanoparticle shape becomes irregular, which was due to the Ag aggregation by thermal annealing. At annealing temperature 500 °C, the Ag diffuse toward both surface and substrate-thin film interface. Progressive growth of Ag cluster with increasing the annealing temperature

was confirmed by diffraction peak. The matrix of TiO₂ partially crystallized in anatase phase at 400 °C annealing temperature. The silver atom diffused in the matrix provides an activation barrier for crystallization. The particle size of Ag nanoparticle was increased from 12.5 nm at 300 °C to 20 nm at 600 °C. They showed that after annealing the nanocomposite thin film, the hardness value increases 4.5 GPa to 7GPa. This was explained by an increment in crystallinity of matrix. Torrell *et al.*⁹⁸ studied the effect of thermal annealing on surface plasmon properties of Au-TiO₂ thin films. They have studied the size, shape and crystallization properties after annealing treatment. Thin film was synthesized by magnetron co-sputtering. The annealing temperature was in the range 200 °C to 800 °C. Initially, nanocomposite thin film does not possess any SPR as they are diffused in the matrix, but at the high annealing temperature, it promotes the formation of nanoparticles. The annealing treatment also affects both the filler and matrix crystallization properties. They have reported the change in SPR position in the range 610-710 nm and making these actively high usable in the decorative coating. Torrell *et al.*⁹⁹ studied the optical properties modification of Au-TiO₂ nanocomposite thin film by thermal annealing. Thin film was synthesized by dc magnetron sputtering. The annealing temperature was varied from 200 °C to 800 °C. Initially, the as-deposited film was amorphous, whose crystallinity improves and anatase phase appears at 500 °C, at high temperature 800 °C the TiO₂ phase completely converted to rutile. The crystallinity of Au increases with the annealing temperature. Also, LSPR intensity increment was also reported with increasing the annealing temperature. This was due to the aggregation of smaller Au nanoparticle and Au atom to form a bigger one. They analyzed the change in colour by studying CIELab colour analysis. The nanoindentation was also done to identify the hardness and elastic modulus values. These values increased with increasing the temperature. This was explained by the crystallinity of thin film. Good adhesion of the film was reported even at the high annealing temperature.

In our study, we have chosen Ag in TiO₂ to reveal the study of high concentration of Ag in TiO₂ for modification of optical and structural properties. These nanocomposite thin films synthesized by RF co-sputtering deposition method. Further, for the modifications in nanocomposite thin film, these were given the thermal annealing treatment and SHI irradiation. From the literature the results show that the pristine nanocomposite for high filler concentration does not show proper absorption, to make useful for an application their optical properties need to be modified. So here

we have selected annealing and SHI irradiation to study the effect on optical and structural properties. For thermal annealing treatment temperature 200, 400, 600 °C has been selected. For SHI irradiation 90 MeV Ni ion beam irradiation is calculated to be suitable for our experiment as it shows high electronic energy loss at this energy.

Synthesis of nanocomposite thin film

Sr. No.	Reference	Materials and synthesis methods	Key observation
1.	Prakash <i>et al.</i> ⁷²	Ag-TiO ₂ nanocomposite, Sol-gel synthesis	antibacterial activity against <i>S. aureus</i> and photocatalytic against methyl orange
2.	Borges <i>et al.</i> ⁷³	Au-TiO ₂ and Au-Al ₂ O ₃ , Reactive DC magnetron sputtering	Thermal annealing shows a change in mechanical and structural properties.
3.	Lin <i>et al.</i> ⁷⁴	Au-TiO ₂ Doctor blade	Photocatalytic of methyl blue, photoexcited charge transfer mechanism
4.	Gültekin ⁷⁵	Au-TiO ₂ Spin coating	Au-TiO ₂ structural, an optical and morphological study
5.	Ahmed <i>et al.</i> ⁷⁶	Ag-TiO ₂ RF magnetron sputtering	Photocatalytic of β -amyloid protein
6.	Viana <i>et al.</i> ⁷⁷	Ag-TiO ₂ Dip coating	Effect of concentration of Ag on plasmon resonance. electron beam exposure
7.	Ahmed <i>et al.</i> ⁷⁸	Ag-TiO ₂ RF magnetron sputtering	photocatalytic degradation of human serum albumin on
8.	Torrell <i>et al.</i> ⁷⁹	Au-TiO ₂ Reactive magnetron sputtering	Tuning of SPR
9.	Torrell <i>et al.</i> ⁸⁰	Au-TiO ₂ Reactive magnetron sputtering	Different Au concentration study
10.	Sangpour <i>et al.</i> ⁸¹	Au-TiO ₂ , Ag-TiO ₂ , Cu-TiO ₂ RF reactive magnetron sputtering	Photodegradation of methyl blue and optical properties study
11.	Uddin <i>et al.</i> ⁸²	Au-TiO ₂ Sol-gel	Photodegradation of methyl blue, self-cleaning
12.	Xu <i>et al.</i> ⁸³	Au-TiO ₂ Precipitation deposition	Photocatalysis of Human Colon Carcinoma LoVo Cells
13.	Tian <i>et al.</i> ⁸⁴	Au-TiO ₂ Sol gel	Photovoltaic fuel cell

Synthesis of nanocomposite thin film by ion implantation

14.	Hou <i>et al.</i> ⁸⁵	Ag-TiO ₂	antibacterial application and photocatalytic performance
-----	---------------------------------	---------------------	--

		40 keV Ag ion (sol-gel deposited TiO ₂)	
15.	Xu <i>et al.</i> ⁸⁶	Ag-TiO ₂ 30 keV Ag ion (DC reactive sputtering deposited TiO ₂)	Characterization with thermal annealing
16.	Stepanov ⁸⁷		A review article
17.	Chang <i>et al.</i> ⁸⁸	Ag-TiO ₂ 40 keV Ag ion	Study of optical properties

Ion irradiation of nanocomposite thin film

18.	Verma <i>et al.</i> ⁸⁹	Au-TiO ₂ 500 keV Ar ²⁺ ion	Photoelectrochemical properties
19.	Chakravadhanula <i>et al.</i> ⁹⁰	Ag-TiO ₂ , Au-TiO ₂ 100 MeV Ag ⁸⁺	Structural and plasmonic modification
20.	Rath <i>et al.</i> ⁹¹	TiO ₂ , 200 MeV Ag ion irradiation, thermal annealing 400-1000 °C	Structural modification and comparison between thermal annealing and irradiation results
21.	Chakravadhanula <i>et al.</i> ⁹²	Ag-TiO ₂	Formation of TiO single crystal
22.	Mishra <i>et al.</i> ⁹³	Au-SiO ₂ , 90 MeV Ni ion irradiation	Growth of Au nanoparticle

Thermal annealing of nanocomposite thin film

23.	Borges <i>et al.</i> ⁹⁴	Au-TiO ₂ , thermal annealing 200-800 °C	Effect of Au concentration and thermal induced modifications
24.	Kumar <i>et al.</i> ⁹⁵	Ag-TiO ₂ , 450 °C thermal annealing	Plasmonic bleaching at 450 °C
25.	Laruinaz <i>et al.</i> ⁹⁶	Au-TiO ₂ , 200-800 °C thermal annealing	Crystallization of TiO ₂ and complex nanoparticle distribution observed
26.	Adochite <i>et al.</i> ⁹⁷	Ag-TiO ₂ , 200-800 °C thermal annealing	Growth of Ag cluster, Ag effect on TiO ₂ crystallization
27.	Torrell <i>et al.</i> ⁹⁸	Au-TiO ₂ , 200-800 °C thermal annealing	SPR tuning
28.	Torrell <i>et al.</i> ⁹⁹	Au-TiO ₂ , 200-800 °C thermal annealing	Redshift, improved mechanical properties and adhesion

Chapter Three

Materials and Methods

3.1 Introduction

In this chapter, the experimental techniques used to synthesize and characterize the nanocomposite thin films are discussed. The performance and quantification of any device depend upon the synthesize and characterization techniques. Their choices are fundamental in experimental science. This chapter is classified into three sections. (i) synthesis techniques (ii) techniques used for treatment (iii) characterization techniques.

3.2 Synthesis of nanocomposite thin film

3.2.1 RF Magnetron sputtering

The nanocomposite thin film texture, quality, uniformity, adhesiveness and morphology directly affected by the deposition techniques. The deposition techniques have to affect uniformness and adhesiveness of the thin film. Borges *et al.*⁷³, Borges *et al.*⁹⁴, Kumar *et al.*⁹⁵, Laruinaz *et al.*⁹⁶, Chakravadhanula *et al.*⁹⁰, Xu *et al.*⁸⁶, Ahmed *et al.*⁷⁶, Adochite *et al.*⁹⁷, Torrell *et al.*⁹⁸, Ahmed *et al.*⁷⁸, Torrell *et al.*⁸⁰, Torrell *et al.*⁷⁹, Sangpour *et al.*⁸¹, Torrell *et al.*⁹⁹, Chakravadhanula *et al.*⁹², Mishra *et al.*⁹³ synthesize the thin film by co-sputtering deposition method. Here we have chosen the RF magnetron co-sputtering technique to deposit the nanocomposite thin film. The magnetron sputtering has more benefits over another deposition method. The magnetron sputtering has the advantages of (i) high deposition rates (ii) high-purity films (iii) ease of sputtering (metal, alloy or compound) (iv) extremely high adhesion and uniformity of films (v) excellent coverage of steps and small features (vi) ease of automation¹⁰⁰¹⁰¹.

In the magnetron sputtering process the inert gas ions (Ar^+) were bombarded on the target surface area. This forceful collision of the Ar^+ and target atom cause to the removal of target atoms, which is called as sputtering. That target atom condenses on a substrate to form a thin film. Here the deposition rate and ionization are low; this was improved by magnetron sputtering. In this system, a strong magnetic field is applied to the target, which increases the interaction time of the electron by making its path helical.

Which results in an increment in the kinetic energy of electron and travel for a longer path. This further help in improving the ionization of the inert gas atom and generate plasma. The figure shows the necessary components of sputtering and schematic of the sputtering process.

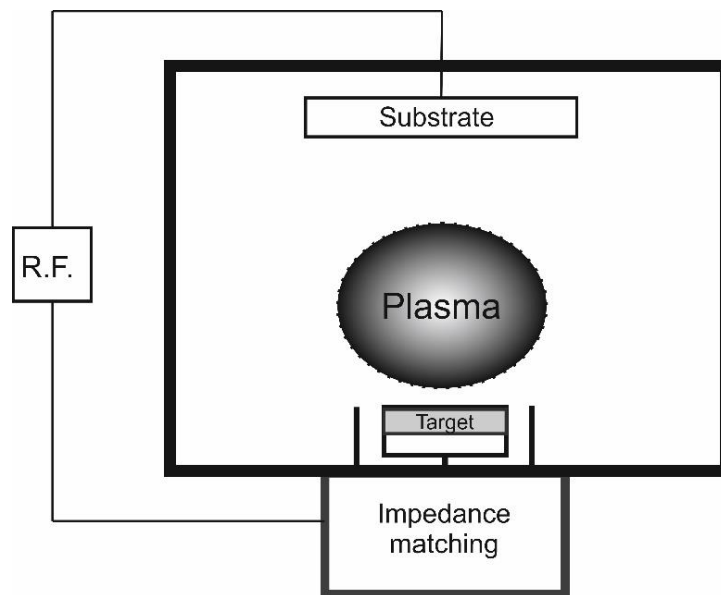


Fig 3.1 Illustration setup of RF sputtering machine

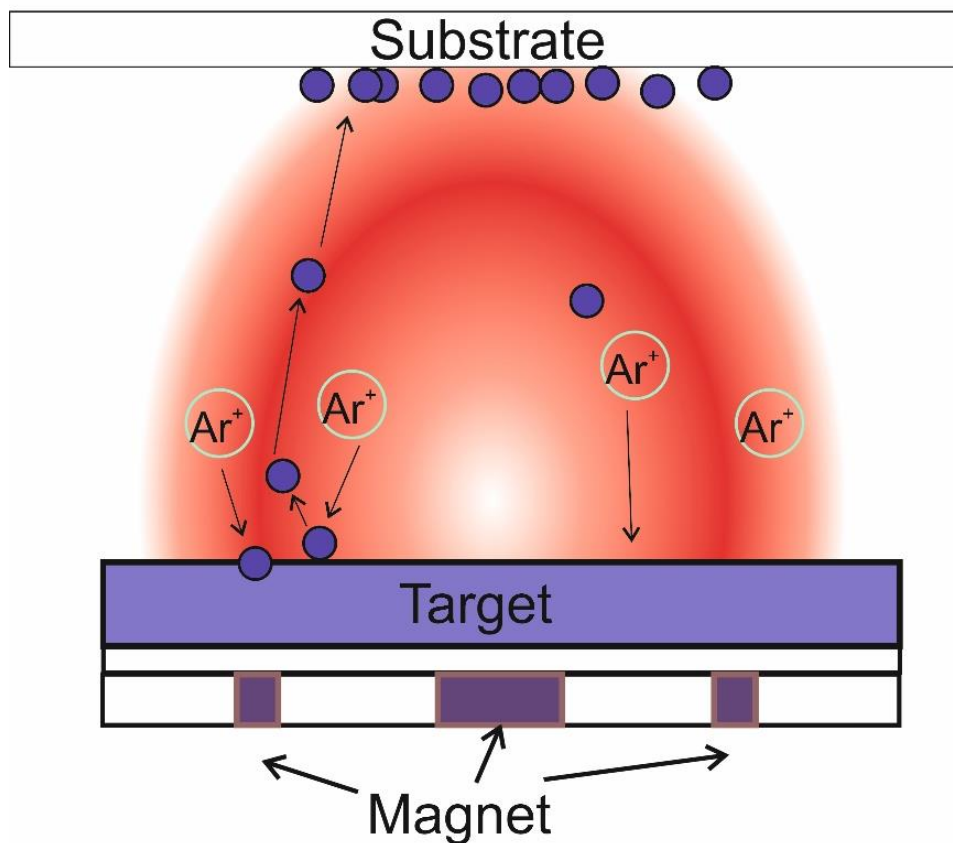


Fig 3.2 Schematic diagram for magnetron sputtering mechanism

3.2.2 Ion implantation

Ion implantation is a method to synthesize nanocomposite thin film with precise control over concentration of filler material and its implanted depth. Hou et al.⁸⁵, Xu et al.⁸⁶, and Chang et al.⁸⁸ synthesized the nanocomposite thin film by ion implantation technique and showed the enhancement in optical properties of nanocomposite thin film.

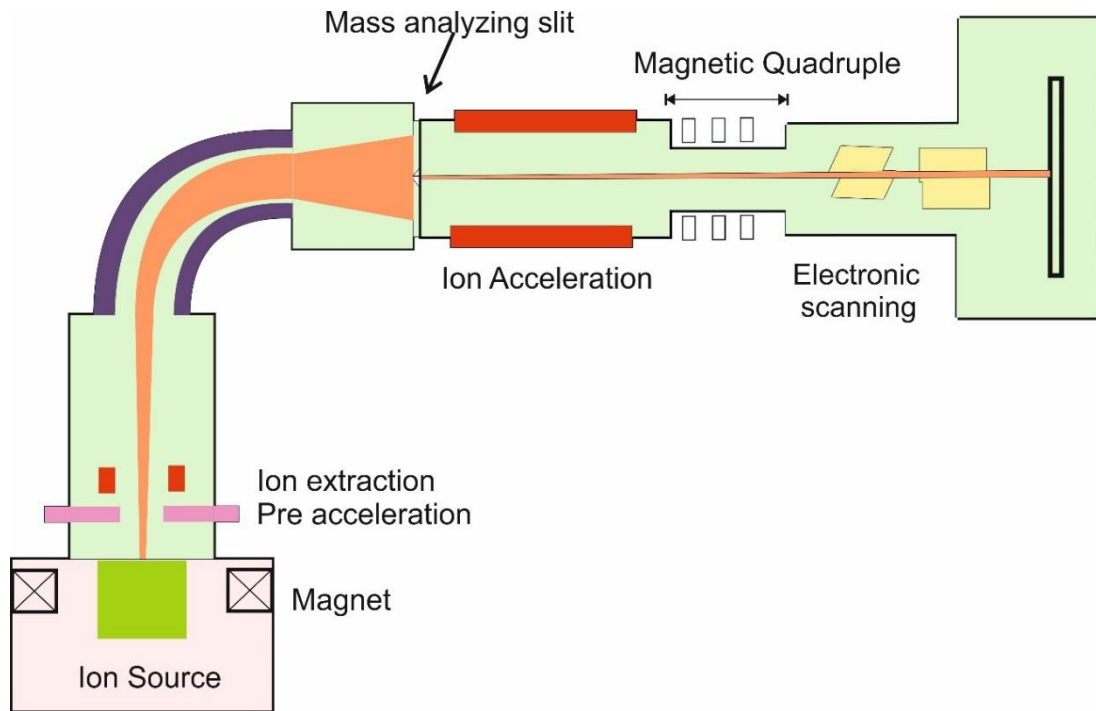


Fig 3.3 Schematic representation of Ion implantation technique.

In ion implantation, the element needs to be implanted was ionized in the ion source facility and further extracted from it through the ion extraction process. During this process, ion gets its pre acceleration due to Coulomb force. Further, it was moved from the magnet, which is used to separate the desired ion from the impurities. After that, the ion was accelerated up to the energy required for implantation and it was scanned through the surface of the target by electronic plates. This whole process occurs in the vacuum. The benefits of ion implantation over other synthesis technique is that it has precise control over dose and depth of implanted ion and complex profile can be achieved by implanting multiple energy ions. This technique is currently used in the fabrication of many semiconductors devices. The relation between implantation time and the dose is given below:

$$t = \frac{D \times e \times A}{I} \quad (9)$$

Where t = implantation time, D= dose of implanted ion, e = electronic charge, A= area of implanted region, I= current during implantation

3.3 Modifications techniques for nanocomposite thin film

3.3.1 Swift Heavy Ion Beam Irradiation

A 15 UD Pelletron accelerator (Electrostatic International Inc. USA) at IUAC New Delhi has been used for irradiation of nanocomposite thin film. It can deliver ion from proton to uranium with an energy range from few MeV to hundreds of MeV, which varies from ion to ion. It has the Tandem Van De Graff type accelerator. In this accelerator, the chain of pellets is used instead of the charge carrier belt. The whole machine is mounted vertically. The symbol 15 and UD stands for 15 MV terminal potential and Unit double respectively. Schematic diagram of the accelerator is shown in figure 3.4. This pelletron accelerator has a tank filled with SF₆ gas at 4 torr pressure. The role of SF₆ is to prevent the electrostatic discharging and sparking as the potential is too high. A high potential between the range 4 to 16 MV has used in the accelerate tube to accelerate the ions at high energy. A negative ion is generated by SNICS (Source of Negative Ion Cesium Sputtering) source, which was injected by injector magnet to potential gradient tube. A few electrons were stripped from the ion by ion stripper to make it from negative to positive ion and increase the charge on it. This ion got accelerated and moved towards the target by analyzer magnet. The energy gain (kinetic energy of ion) is given by the relation

$$E = E_o \text{ keV} + V_{\pi}(q + 1) \text{ MeV} \quad (10)$$

Where V_{π} is accelerating potential, q is charge states of ion.

The irradiation process was carried out at the material science beamline at IUAC New Delhi. The vacuum in beamline is maintained at Ultra High vacuum at pressure 10^{-9} torr and target was irradiated in the high vacuum target chamber. The vacuum in target chamber is maintained at 10^{-6} torr. The target was placed on the multi-target capacity ladder which was specially designed at IUAC for multi-target facility without breaking the vacuum. The irradiation was carried out at room temperature and keeping the current stable.

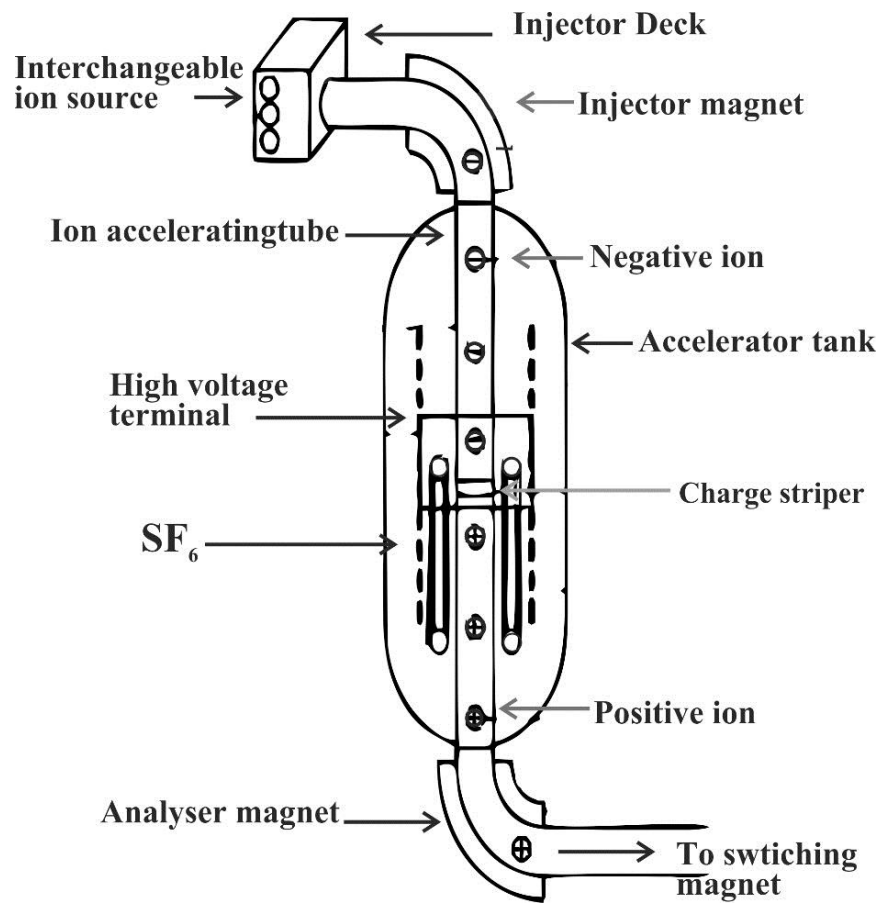


Fig 3.4 Schematic diagram of pelletron accelerator

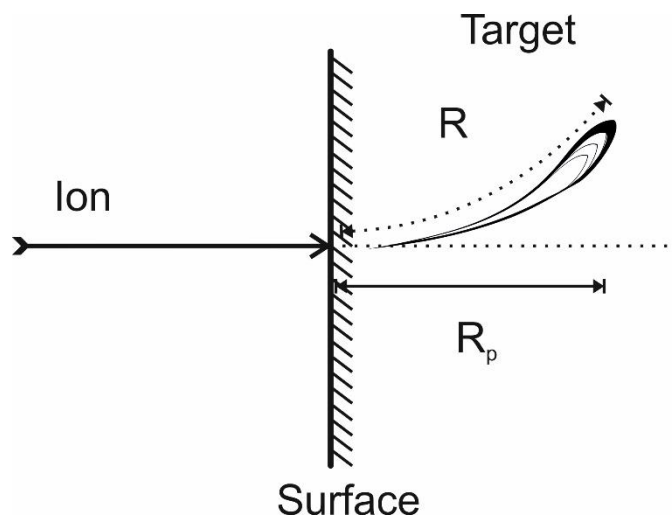


Fig 3.5 Total path length R and projected range R_p representation.

The ion beam energy loss mechanism, both nuclear and electronic energy loss was discussed in chapter 1. Figure 3.5 represents the range and path of ion in the matter. The integrated distance travelled by an ion is called as range R, whereas the net

penetration depth along the incident ion trajectory is called the projected range R_p . If ion incident perpendicularly on the target surface then the projected range vector is also perpendicular to the target surface area. In this ion matter interaction, the ion beam losses energy by rate dE/dx which is between few to 100 eV/nm. The range R is defined by the formula

$$R = \int_{E_0}^0 \frac{1}{dE/dx} dE \quad (11)$$

Where E_0 is the incident energy of ion beam and x is the depth from the surface in the target.

3.3.2 Thermal annealing

Thermal annealing is also another useful tool to modify the properties of nanocomposite thin film as discussed in chapter 1. A schematic diagram of thermal annealing is shown in figure 3.6. Ar gas was used as an ambient environment for annealing. The gas flow was controlled by the flow meter. Then the gas was inserted into the tube through

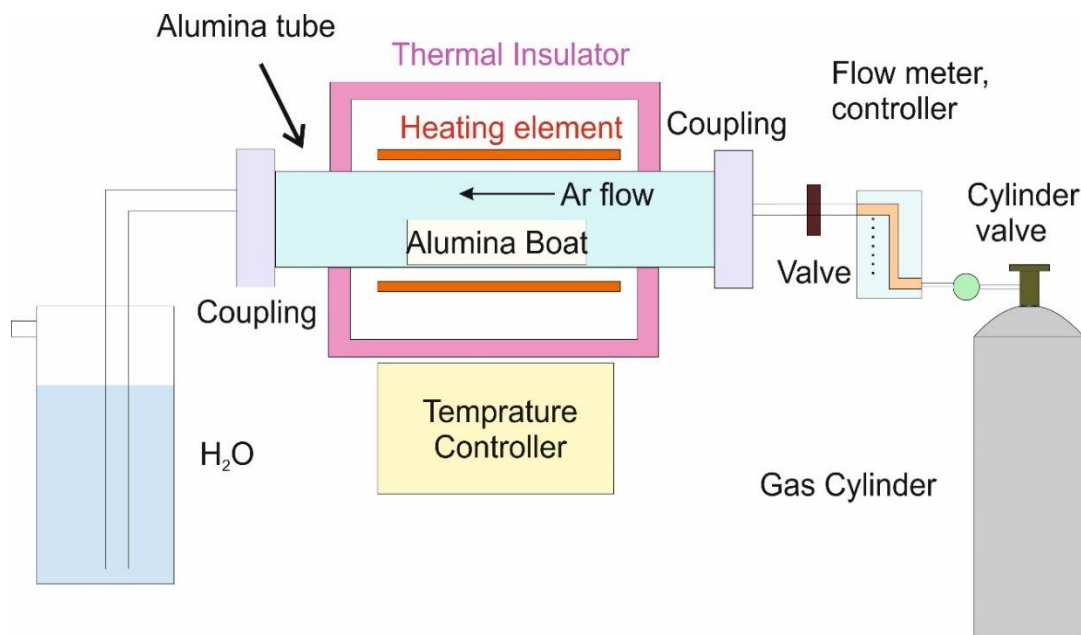


Fig 3.6 Schematic diagram for furnace setup used for annealing nanocomposite thin film

coupling attached at the end of the alumina tube. This alumina tube (dia 2 inches) was heated with silicon carbide heating element. The heating was controlled by the inbuilt controller. The flow of Argon gas remains continuous during the whole time. To place

the deposited thin film in the tube furnace alumina boats were used. This controller has the program to control heating the tube at a programmed ramp rate.

3.4 Characterization techniques

3.4.1 Rutherford Backscattering Spectroscopy

Rutherford backscattering spectroscopy (RBS) was used to measuring the thickness and composition of the thin film. Fig 3.7 represents the schematic of the experimental setup. There were three essential component in this setup (i) ion source (generally He^+) (ii) linear accelerator (to accelerate the ion in the range 1-3 MeV) (iii) detector (to measure the backscattered energies). RBS was based on the collision of atomic nuclei and it measures the number of the backscattered ion. This scattering depends upon the target nuclei and incident nuclei^{70,102}.

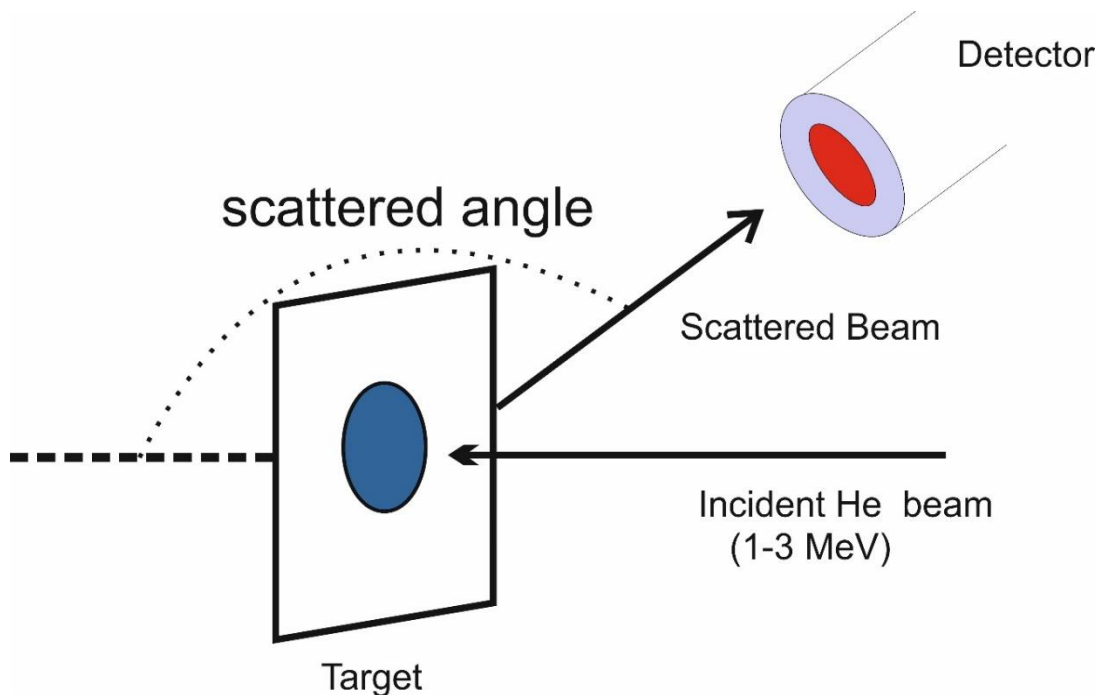


Fig 3.7 Schematic representation of experimental setup of RBS

The interaction between these nuclei was explained as elastic collision regarding scattering cross section. The scattered nuclei energy was linked by kinematic factor and depth of the target. This kinematic factor depends upon the scattering angle and mass of the incident and target nuclei atom. The kinematic factor was also stated as the ratio of scattered and incident nuclei energy.

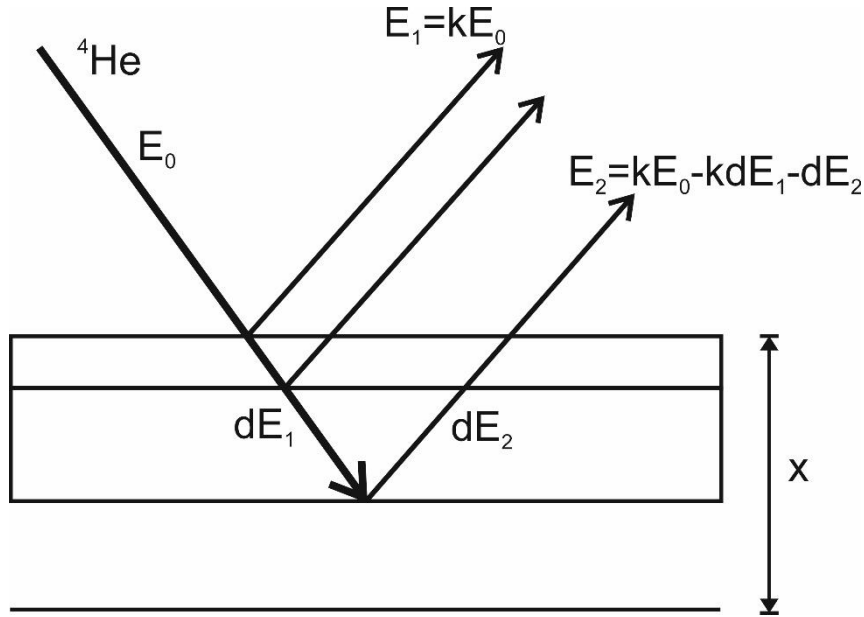


Fig 3.8 Schematic of scattered nuclei energy difference with thickness in RBS

The kinematic factor is given by the formula

$$K = \frac{E_{sca}}{E_{in}} = \left[\frac{\left(1 - \left(\frac{M_1 \sin \theta}{M_2}\right)^2\right)^{1/2} + \frac{M_1 \cos \theta}{M_2}}{1 + \frac{M_1}{M_2}} \right]^2 \quad (12)$$

Where M_1 , M_2 are the masses of the incident and target atom and θ is the scattering angle. The RBS has a good mass resolution for lighter elements. The scattered nuclei energy increases as the target atom mass increases. That is because of the decrement in the momentum transfer to the target nuclei. To differentiate the heavy target element, it is suggested to use the heavy incident nuclei. The schematic representation of energy difference during scattering is given in fig 3.8. The thickness (Δx) of the film is measured by the formula given below

$$\Delta x = \frac{\Delta E}{S_0} \quad (13)$$

Where,

$$S_0 = \left[k \left(\frac{dE}{dx} \right)_{E_0} + \frac{1}{\cos \theta} \left(\frac{dE}{dx} \right)_{kE_0} \right] \quad (14)$$

ΔE is the difference in energy of incident and scattered nuclei

Here $\frac{dE}{dx}$ is the function of nuclei energy. The energy at depth x is given by

$$E_x = E_0 - \int_0^x \frac{\Delta E}{\Delta x} dx \quad (15)$$

Application:-

- (i) Thickness and depth profile measurement

- (ii) Compositional analysis
- (iii) Channelling

3.4.2 X-ray diffraction spectroscopy

X-ray diffraction is a nondestructive technique for the identification of various crystalline structure. The x-ray diffraction also reveals the physical properties and chemical composition of the thin film. This diffraction is explained by Bragg's law¹⁰³

$$n \lambda = 2d \sin \theta \quad (16)$$

Where d = distance between atomic layers

λ = wavelength of X-ray

θ = diffraction angle

n = integer number

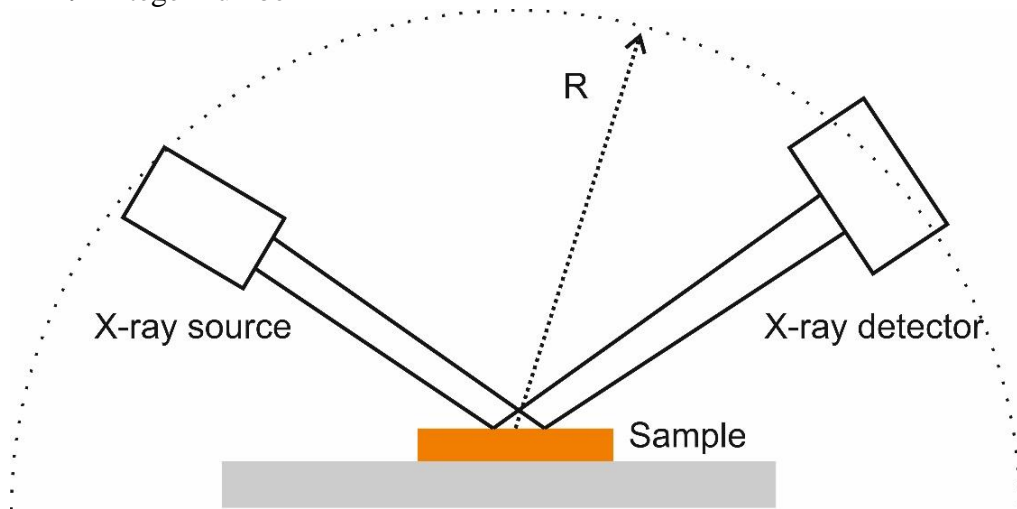


Fig 3.9 Schematic layout for X-ray diffraction instrument

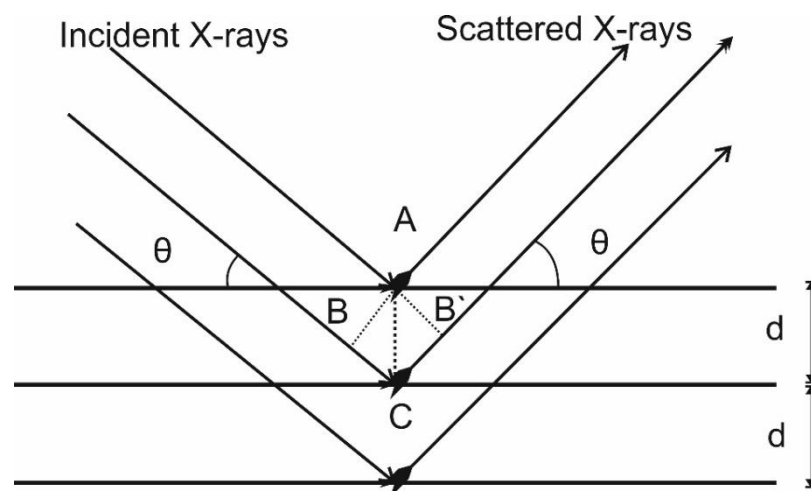


Fig 3.10 Schematic representation of X-ray diffraction from sample

The schematic diagram of instrument is given in fig 3.9. Fig 3.10 represents the diffraction of X rays by layers of the sample.

There are two common parts in the XRD instrument. (i) X-ray source (ii) X-ray detector. Here Cu K_α (1.54 Å) is used as an X-ray source. To analyze the data X'pert highscore¹⁰⁴ is used provided with the machine.

Application:-

- (i) Determination of atomic layer spacing
- (ii) Lattice constant
- (iii) Dislocation density
- (iv) Stress

3.4.3 UV-visible absorption spectroscopy

When light falls on the material, the light gets reflected, transmitted or absorbed. This phenomenon depends upon the material properties and incident light wavelength. This interaction of light with materials can provide information about the optical properties of materials. The absorbance is given by Beer Lambert's law⁴², according to that the absorbance is directly proportional to concentration *c* and the path length *l*.

$$A = -\log_{10} \frac{I}{I_0} = e \cdot l \cdot c \quad (17)$$

Where *e* is the proportionality constant, *l* is path length and *c* is concentration.

Here we have studied absorption of UV-visible light by nanocomposite thin film. The light gets absorbed by nanoparticle in the form of surface plasmon resonance, discussed in chapter 1.

Fig 3.11 shows the layout of dual beam Hitachi spectrophotometer used for the absorption measurements. The absorption in the visible region is the direct indication of SPR absorption. From this, it is possible to determine the band gap of nanocomposite thin film using the Tauc plot¹⁰⁵ method. Tauc equation is given by

$$(\alpha h\nu)^{1/n} = A(h\nu - E_g) \quad (18)$$

Where α = absorption coefficient

h = Plank's constant

ν = frequency of incident light

A = proportionality constant

E_g = Band gap

n = depends upon allowed or forbidden and direct or indirect transition.

1/2 for directly allowed transitions

3/2 for direct forbidden transitions

2 for indirect allowed transitions

3 for indirect forbidden transitions

The allowed transitions dominate the other values of n . So we took $n=1/2$ or 2 and compared the graph which provides the best fit for the band gap.

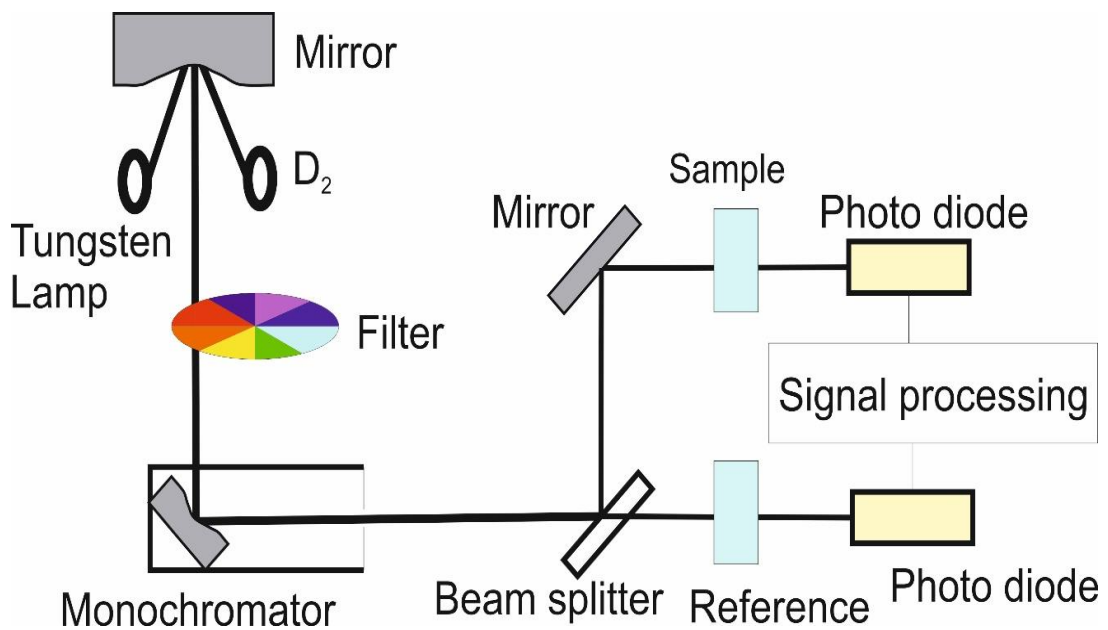


Fig 3.11 Layout of UV-visible absorption spectrometer.

Application:-

- (i) Surface plasmon resonance position can be identified
- (ii) The band gap of material can be calculated using Tauc Plot.
- (iii) Absorption and transmittance of material.

3.4.4 Fluorescence spectroscopy

It is the simple technique to determine the fluorescent properties and relative analysis of the sample. In fluorescence spectroscopy, a beam of wavelength, range between 180 nm to 800 nm is used to pass on the sample. In the sample the light got absorbed and further it emits the light which was detected by a detector which is at a different angle of incident light path. A setup diagram is shown in fig 3.12. In fluorescence

spectroscopy, both emission and excitation spectrum can be measured. In some cases due to the creation of defects, fluorescence properties are enhanced and new energy levels are created¹⁰⁶. In the case of nanocomposite thin film fluorescence is also affected by the interaction between filler and matrix.

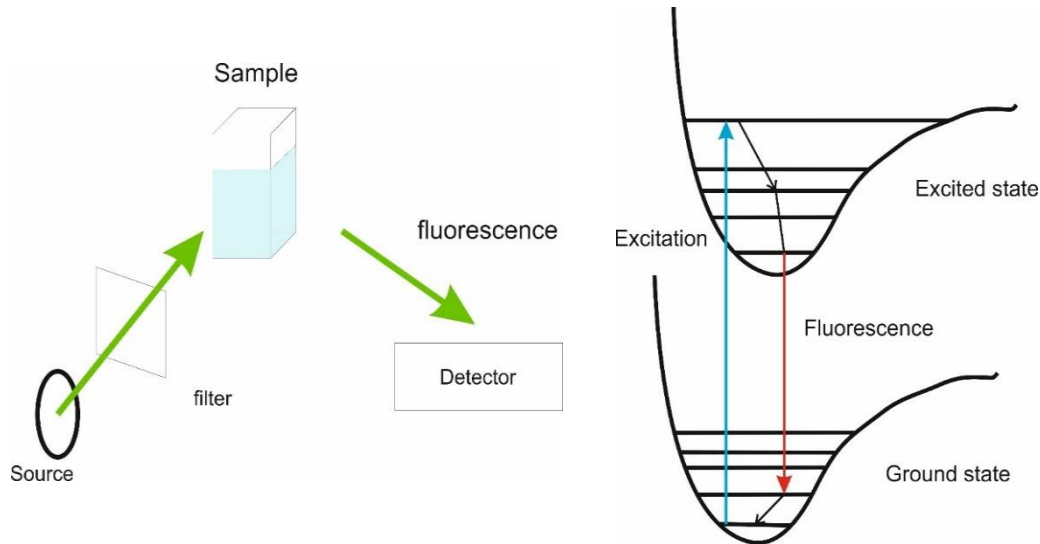


Fig 3.12 Schematic of fluorescence setup, excitation and fluorescence process diagram.

Application:-

- (i) Provides the information about the presence of creation of defects
- (ii) The interaction between the two material can be identified.

3.4.5 Transmission electron microscopy

In Transmission electron microscope (TEM) an energetic electron beam interacts with a very thin specimen. Due to the interaction, the electron beam got diffracted, passed through it and scattered. This transmitted electron beam can be identified using the imaging CCD sensor and a fluorescent screen. It is an outstanding tool for providing information about internal microstructure. This technique provides the high-resolution image of the order of few nm. The variation in the image intensity provides information about the defects, dislocation and specimen identification. TEM characterization is done using Tecnai G 2 20 (FEI) S-Twin kV. TEM analysis is done using digital micrograph software. The de Broglie wavelength of the electron beam at energy 200kV potential is given below^{107,108}.

$$\lambda = \frac{h}{\left[2m_0eV\left(1+\frac{eV}{2m_0c^2}\right)\right]^{1/2}} \quad (19)$$

At 200 kV $\lambda = 0.00273$ nm (for non relativistic case)

$\lambda = 0.00251$ nm (for relativistic case)

Due to this very low wavelength value TEM provide high-resolution images than a light microscope. TEM makes it useful in both biological and physical science. A typical TEM instrument is shown in fig 3.13. TEM work generally in two different modes (i) Image mode (ii) Diffraction mode.

(i) Image mode

(a) **Bright field Image mode:** In this mode, the incident electron beam passes through the specimen. With the help of aperture in the back focal plane (which block the diffracted electron beam) image can be obtained. This kind of image is called the bright field image and used to identify the microstructure of the specimen.

(b) **Dark field image mode:** for the crystalline sample the incident electron beam diffracted in a pattern from the various planes of specimen. Among this diffracted beam, one of the beams is allowed to pass using an aperture and images are obtained. This kind of image is called the dark field image and useful for the analysis of the single crystalline sample.

(ii) Diffraction mode

In diffraction mode, the diffracted beam is focused using the objective lens. In diffraction mode, various spot pattern is observed. If specimen is single crystalline these spots are in a regular pattern, for polycrystalline, circular rings are obtained whereas for the amorphous sample a broad ring is obtained. In this mode, the objective aperture is removed only intermediate aperture is used which allowed passing the diffracted beam. The more interplane distance D is given by

$$R D = L \lambda \quad (20)$$

Where R = distance of spot from the centre spot

L = camera length

λ = de Broglie wavelength of the electron beam

Application:-

- (i) Image morphology
- (ii) Electron diffraction pattern
- (iii) EELS spectroscopy
- (iv) Structure of material
- (v) Interplanar spacing

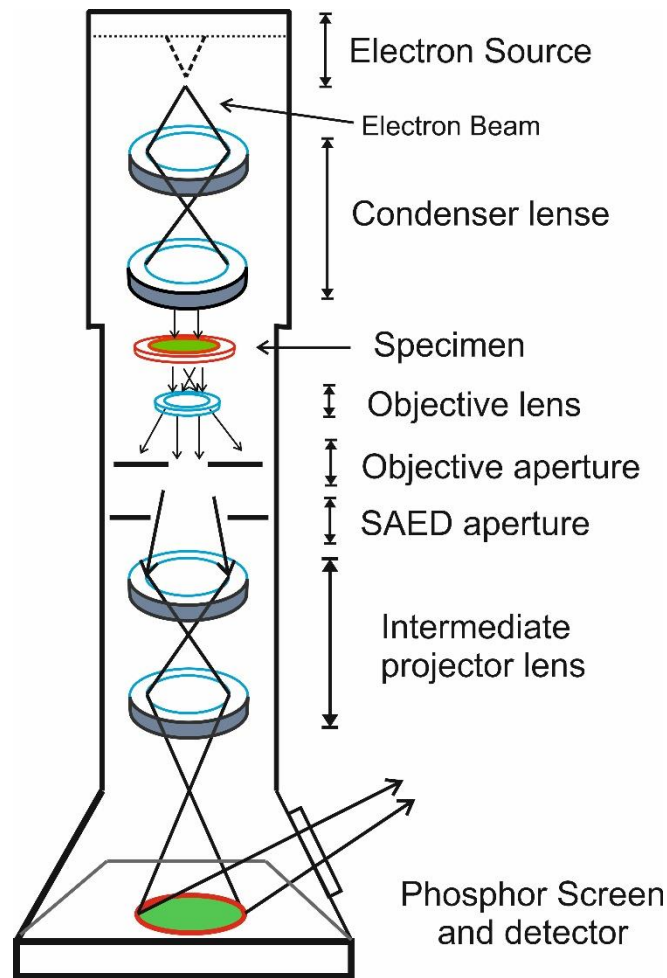


Fig 3.13 TEM instrument setup block diagram

3.4.6 X-ray Photoelectron spectroscopy

XPS is based on the kinetic energy of electron expelled from the sample irradiated by a monochromatic X-rays. Characteristic X-ray lines are used for the excitation of the electron. XPS is useful for the identification of electronic structure and binding energies. This binding energy allows the chemical state analysis. From this technique, elemental composition and empirical formula can also be identified. It is a very

sensitive technique, as the mean free path for photoelectron is 3 - 50 Å. Fig 3.14 shows the schematic representation of the XPS instrument. In this Mg or Al X-rays used as a source. The energy of Al K_{α} and Mg K_{α} is 1486.6 and 1253.6 eV respectively. The binding energy can be calculated by using the relation.

$$E_{binding} = E_{phototn} - E_{kinetic} - \varphi \quad (21)$$

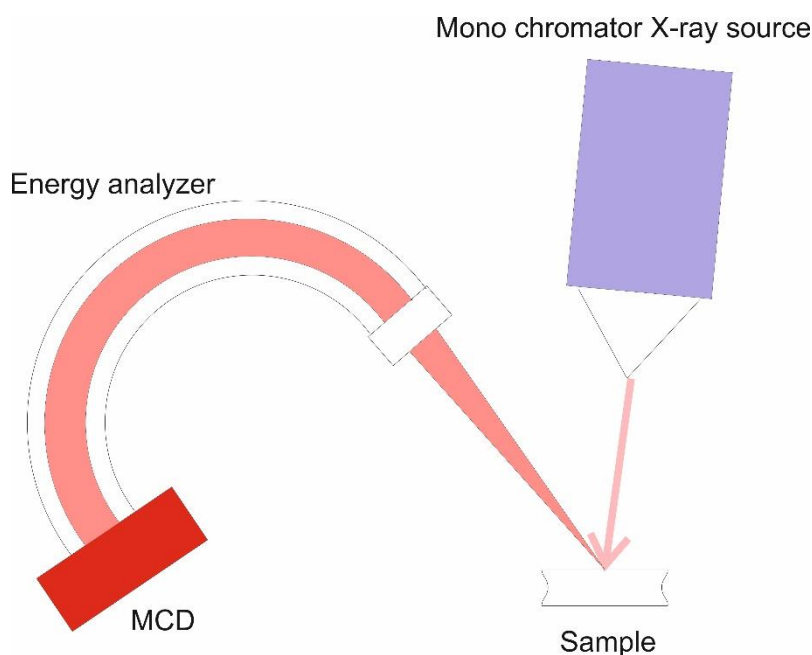


Fig 3.14 Schematic representation of XPS apparatus setup

Where $E_{binding}$ = energy of the electron emitted

$E_{phototn}$ = energy of the X-ray photon

$E_{kinetic}$ = kinetic energy of electron

φ = work function of the spectrometer

There is three basic component in this experimental setup (i) fixed energy X-ray source (ii) electron energy channel analyzer (concentric hemispherical analyzer) (iii) ultra-high vacuum. The basic behind XPS analysis is in the binding energy of the electron to the atom. Each element has a particular value of binding energy and it depends on the atomic number and quantum number.

Application:-

- (i) Chemical composition
- (ii) Surface analysis
- (iii) Electronic state

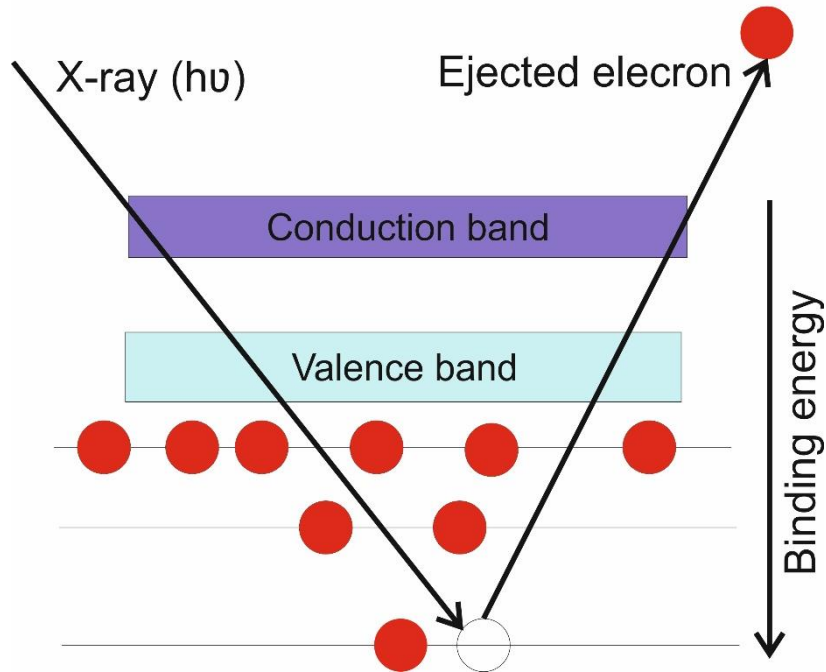


Fig 3.15 Ejection of core level electron from X-ray and dependencies on binding energy

3.4.7 Finite difference time domain simulation

FDTD is a numerical based analysis in which it uses Maxwell's equation to identify the variables within the time domain for the interaction of matter with the electromagnetic wave. The differential equation approximated in the finite difference is used to solve for small space grids. Leapfrog integration is used to calculate the electric vector first and then the magnetic vector component. This tool has attracted by its function of solving the complex problem and fast response for the use of interaction of electromagnetic wave with the matter.

Chapter Four

Synthesis of Ag-TiO₂ nanocomposite

4.1 Introduction

Synthesis of nanocomposite thin film with the variation of sizes and shapes of nanoparticles are of fundamental interests in physics. These kinds of nanocomposite thin film have potential applications in the various field. It is a challenge to synthesize the nanocomposite thin film which attains the potential to show diverse applications. This chapter briefs the results of Ag nanoparticle in the TiO₂ matrix. Based on the synthesis method, this chapter is divided into two section (i) Synthesis by RF sputtering (ii) Synthesis by Ion implantation.

4.2 Synthesis of nanocomposite thin film by RF sputtering

Several dielectric materials as ZnO¹⁰⁹, SiO₂¹¹⁰, ZrO₂¹¹⁰, Al₂O₃¹¹¹ fullerene¹¹¹ and polymer¹¹² are utilized in the fabrication of different multifunctional nanocomposites for various applications. In the present section, the TiO₂ matrix has been used for embedding Ag nanoparticles. TiO₂ is widely used in photocatalysis^{113,114}, micro-electric devices¹¹⁵, optical coating¹¹⁶, anti-reflector¹¹⁷, high dielectric constant, high refractive index, large band gap and relative non-toxicity. Due to the high band gap of TiO₂, it cannot function in the UV region. The loading of noble metal nanoparticles such as Ag, Au, Pt, etc., profoundly enhances the properties of TiO₂ to work in the visible region. Both the Ag and TiO₂ have some common properties and widely used. Nanoparticles of Ag show optical absorption due to SPR in the visible spectrum. So Ag-TiO₂ nanocomposite thin films have many applications in the photo-catalytic¹¹⁸ and plasmonic devices. The properties like size, shape and distribution of Ag nanoparticle affect the structural, optical, and electronic properties of Ag-TiO₂ nanocomposite materials¹¹⁹. These properties are also affected by the concentration of Ag and by depositing different concentration of metal in the TiO₂ matrix, these properties can be tuned easily. Different techniques have been used to synthesize the Ag-TiO₂ nanocomposite thin films such as ion implantation, magnetron sputtering (DC & RF), and chemical synthesis (sol-gel method).

In this section, various concentrations of Ag nanoparticles in TiO₂ have been synthesized and effect of Ag concentrations on the physical properties of nanocomposite thin film has been investigated by XPS, UV and TEM.

4.2.1 Experimental detail

Nanocomposites of Ag-TiO₂ and TiO₂ thin films have been deposited by RF sputtering using Ag foil pieces and solid TiO₂ target; this target has been prepared in the laboratory using TiO₂ powder of Alfa Aesar (99.9%). The substrates of Si, quartz and glass were ultrasonically cleaned in D.I. water and acetone. Then these were washed by TCE (Tri-Chloro Ethylene), methyl alcohol and acetone. In the RF sputtering chamber, the target to substrate distance was kept at 13 cm, and substrate holder rotates with the help of a DC motor to get uniform composition and thickness. The vacuum in the chamber before the deposition was 1.2×10^{-6} torr. The target was sputtered in Ar gas medium at pressure $\sim 8 \times 10^{-3}$ torr and the pure TiO₂ thin films were deposited for 30 minutes. For inclusion of the Ag, Ag pieces (surface area = 6 mm², thickness=0.5 mm each, purity 99.8%) were stuck to the target surface. To vary the concentration of Ag, we have varied the number of pieces attached to the target surface near the region where the plasma ring was obtained. Thin films of four different concentrations of Ag in the TiO₂ matrix were prepared. The deposition parameters were the same as in the case of pure TiO₂ thin film. These thin films were deposited at RF power of 75 W and Ar gas flow of 11 sccm. No heat treatment was given to the substrate during and after deposition. For TEM characterization, depositions were taken on a carbon coated copper grid for each concentration of Ag for 10 min and another parameter was kept the same. In this section, the RF magnetron sputtering technique has been used to deposit Ag-TiO₂ matrix due to the advantage of flexibility in this technique and also better adhesion of the film to the substrate. Deposition of nanocomposite films by sputtering also shows the controlled growth of the size, shape, distribution by changing the parameters like RF-power, pressure, substrate temperature and deposition time.

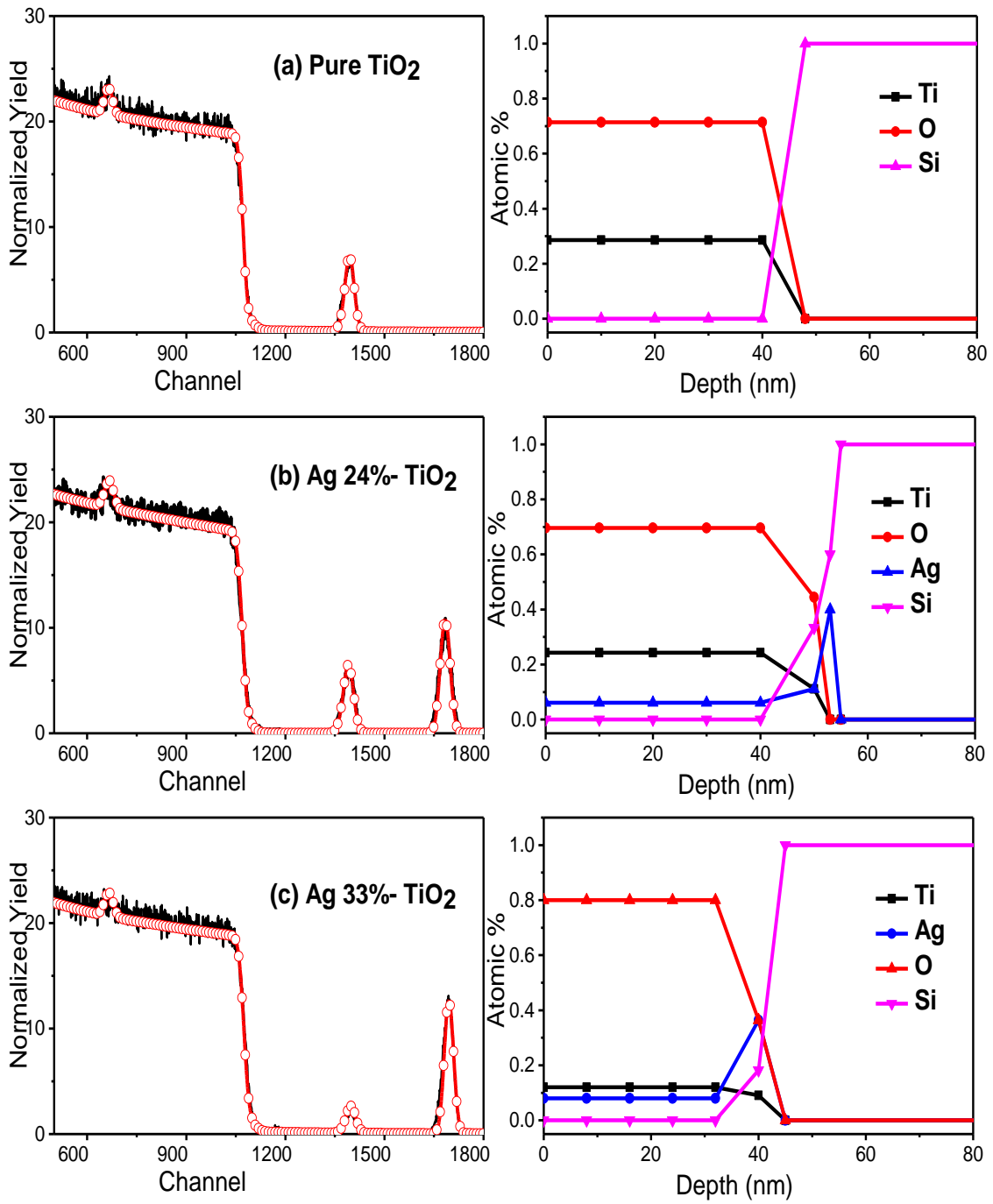
The concentration of Ag and thickness of nanocomposite thin films on Si substrate were characterized by Rutherford Backscattering (RBS) spectrometry. The detector was kept at an angle of 165° on incident beam 2 MeV He⁺ beam at IUAC, New Delhi, India. X-ray diffraction (XRD) measurements were carried out using Panalytical X-Pert Pro X-ray diffractometer to determine the crystallinity of thin films. To analyze the optical

properties nanocomposite thin films deposited on quartz substrates have been characterized by UV-visible absorption spectroscopy using a dual beam Hitachi photo spectrometer and Raman spectroscopy of nanocomposite thin film deposited on a silicon substrate using AIRIX STR 500 Raman microscope with laser excitation at 532 nm. These thin films were characterized by high-resolution Transmission Electron Microscope (HR-TEM) (Tecnai G2 20 (FEI) S-Twin 200 kV), to analyze the particle size, nanoparticle distribution and inter-planer spacing. X-Ray Photoelectron Spectroscopy (XPS) technique was used to determine the stoichiometry of the host matrix and to identify the interaction between the Ag nanoparticle and host matrix. Omicron ESCA instrument was used for this with a monochromatic source of Al anode and its energy was 1486.7 eV.

4.2.2 Composition and Structural Studies

Fig 4.1 shows the RBS spectra and the depth profiles of TiO₂ and Ag-TiO₂ nanocomposite thin films for various concentration of Ag on Si substrates. The thickness and the concentration of Ag metals were determined using the RUMP¹⁰² program and found to be ~45 nm and 24%, 33%, 45%, 56% respectively. Simulation from RUMP program confirmed that in case of TiO₂ thin films only two elements O and Ti are present, whereas in Ag-TiO₂ nanocomposite thin films Ag, Ti, O ions are present. While increasing the inclusion of Ag in the TiO₂ matrix, counts of Ag increases, this confirms the increase in the concentration of Ag. Due to the difference in the sputtering rate of Ag and TiO₂, Ag sputter at lower power value than TiO₂. That is why we have an increment in Ag weight at the interface between the Ag-TiO₂ thin film and the silicon substrate.

The XRD pattern of pure TiO₂ and TiO₂ with Ag at a concentration of 24%, 33%, 45% and 56% are shown in fig 4.2. In TiO₂ thin film, a highly intense peak of anatase phase at 25.9° and low intensity of anatase at 54.8° was observed. A shift in the peak of anatase at 25.9° by 0.4° to lower 'θ' value appears due to the inclusion of Ag ion in place of Ti ion. The ionic radius of Ag is greater than Ti ion which causes to increase in d-spacing value and reduction in diffraction angle. The Ag peak is observed at 38°, the intensity of this peak increases with Ag concentration. XRD pattern matches well with JCPDS card no. 89-4203 and 87-0719.



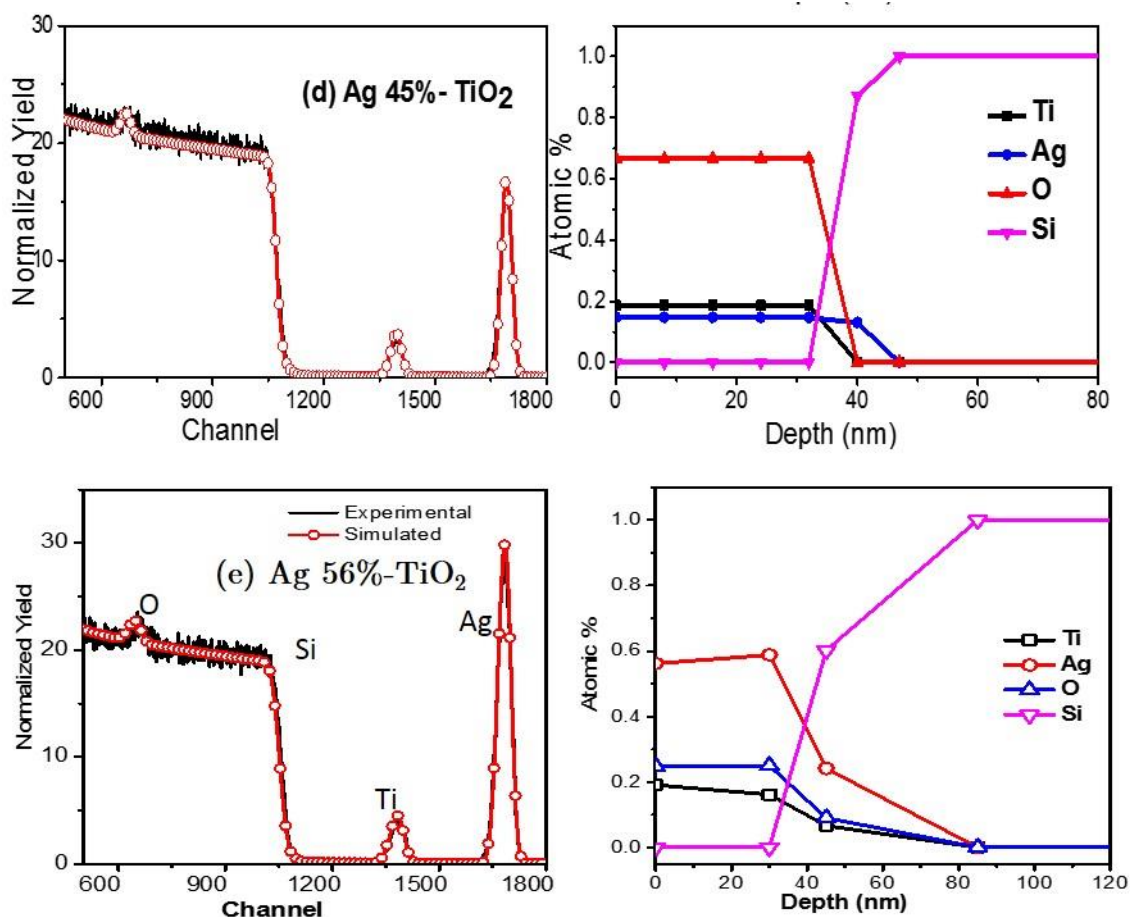


Fig 4.1 RBS simulation and depth profiles of TiO_2 and Ag-TiO_2 . The simulation showed with symbol and experimental data with the line. (i) TiO_2 , (ii) Ag-24\%-TiO_2 , (iii) Ag-33\%-TiO_2 and (iv) Ag-45\%-TiO_2 (d) Ag-45\%-TiO_2 and (e) Ag-56\%-TiO_2

The lattice constant of TiO_2 was calculated from Rietveld analysis using high score plus¹⁰⁴ shown in the Table-2. The lattice constant 'c' decrease by 0.5 \AA from 9.4 \AA (TiO_2) to 8.9 \AA (Ag 33\%). We have obtained the anatase phase because the deposition was carried out at room temperature and the anatase was more stable at a lower temperature than rutile phase because of its low surface energy¹²⁰. The inclusion of Ag nanoparticles in the TiO_2 matrix affects the phase of TiO_2 , and it is reflected in the XRD. The intensity of the anatase phase decreases with the concentration of Ag. At a concentration of 45%, 56% anatase phase completely vanishes and Ag (111) phase takes growth with an increase in Ag concentration. The anatase phase of the plane (105) disappears with the inclusion of Ag. The increase in crystallinity of Ag was supported

by SAED pattern, the intensity of the ring increases with Ag concentration and also very thick ring has been observed because of amorphous TiO₂, which was in agreement with XRD analysis.

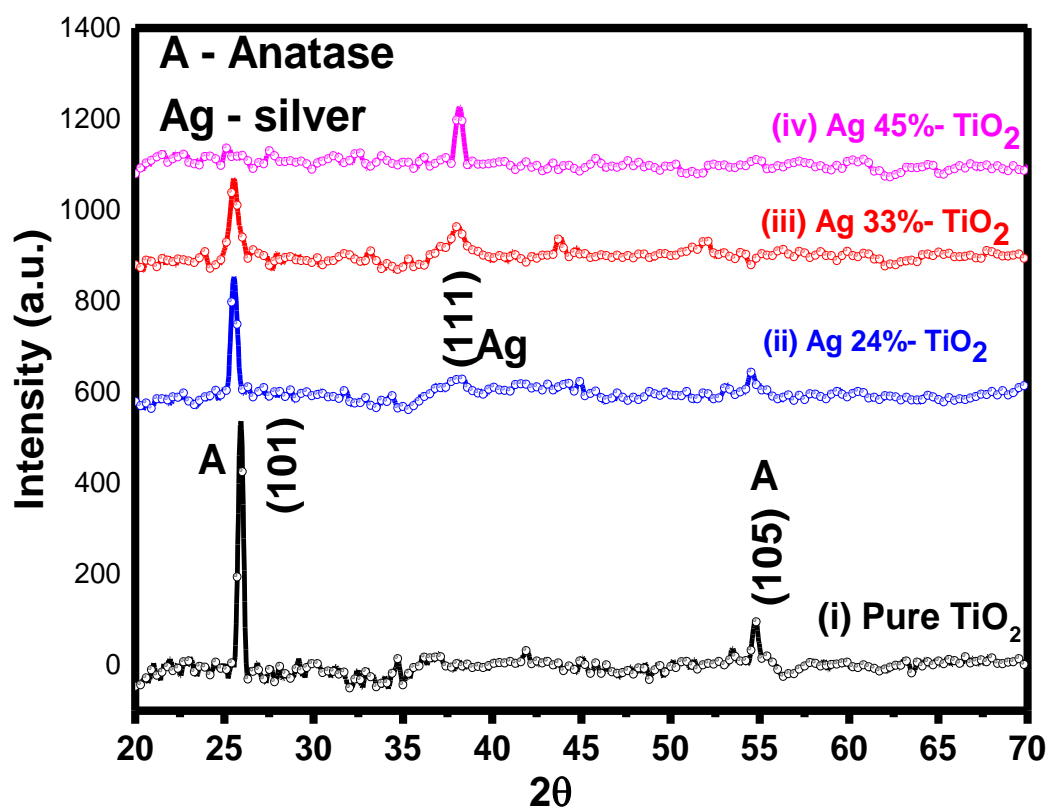


Fig 4.2 XRD pattern of TiO₂ and Ag-TiO₂, showing the anatase phase and affect of Ag concentrations on its phase (i) TiO₂, (ii) Ag-24%- TiO₂, (iii) Ag-33%- TiO₂ and (iv) Ag-45%- TiO₂ (v) Ag-56%- TiO₂

Table 2. Lattice constant calculated from XRD

	(a) Pure TiO ₂	(b) Ag 24%	(c) Ag 33%
a=b (Å)	3.77	3.72	3.58
c (Å)	9.44	9.36	8.92
Cell volume (Å ³)	134	129	114

4.2.3 Morphological Studies using HR-TEM

The images from HR-TEM of TiO₂ and Ag-TiO₂ are shown in fig 4.3. From the SAED pattern, the Ag nanoparticles are in crystalline and signature of Ag with phase (111) has been found for all concentrations. The anatase phase of TiO₂ has been observed for the

Ag concentration of 24%. From SAED pattern, a vast ring has been obtained which was due to the decrease in crystallinity or increments of the amorphous phase of anatase phase. The thickness of this thick ring increases with Ag concentrations. The average particle size has been analyzed by plotting histogram graphs, ~200 nanoparticles have

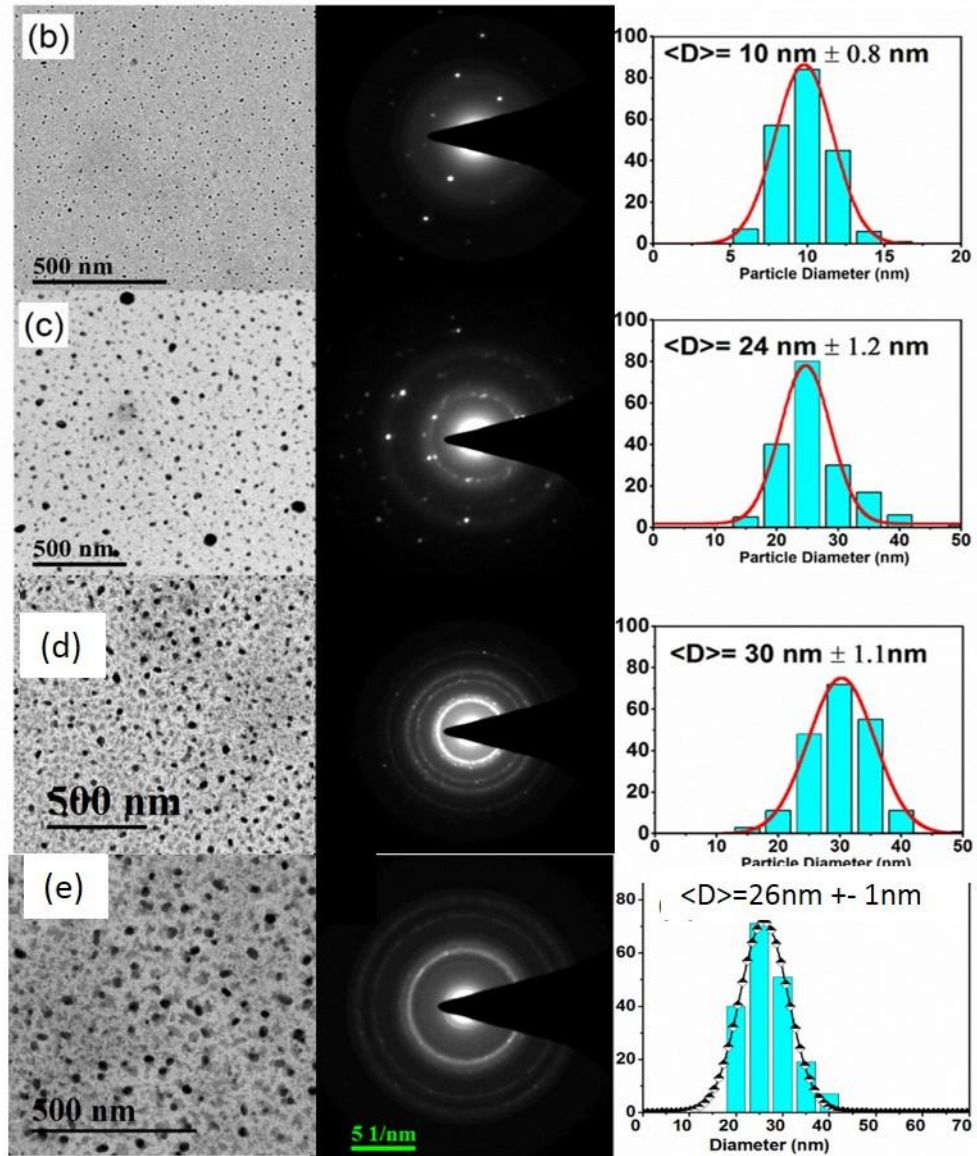


Fig 4.3 Plan view, bright field TEM images with SAED pattern and histogram of particle size distribution. (i) Ag-24%- TiO₂ (ii) Ag-33%- TiO₂ (iii) Ag-45%- TiO₂

been analyzed to draw histogram plotting in each figure, the particle size increases with Ag concentration due to the agglomeration of nearby nanoparticles and local heating effect created during the deposition by sputtering. In fig 4.3 (ii) some big Ag nanoparticles were observed compared to other images, this can be understood by

bimodal. In bimodal the particle on the surface of the thin film is bigger than the nanoparticles in the thin film. However, their number is very less. Bright field images of TEM verify the formation of Ag nanoparticles. From the histogram, the average radius of Ag nanoparticles for the concentration of Ag 24%, 33%, 45%, 56% was calculated to be 5 nm, 12 nm, 15 nm, 13 nm respectively. The average diameter of Ag nanoparticles was increased with the concentration of Ag, but the interparticle separation decreases as shown in fig 4.4.

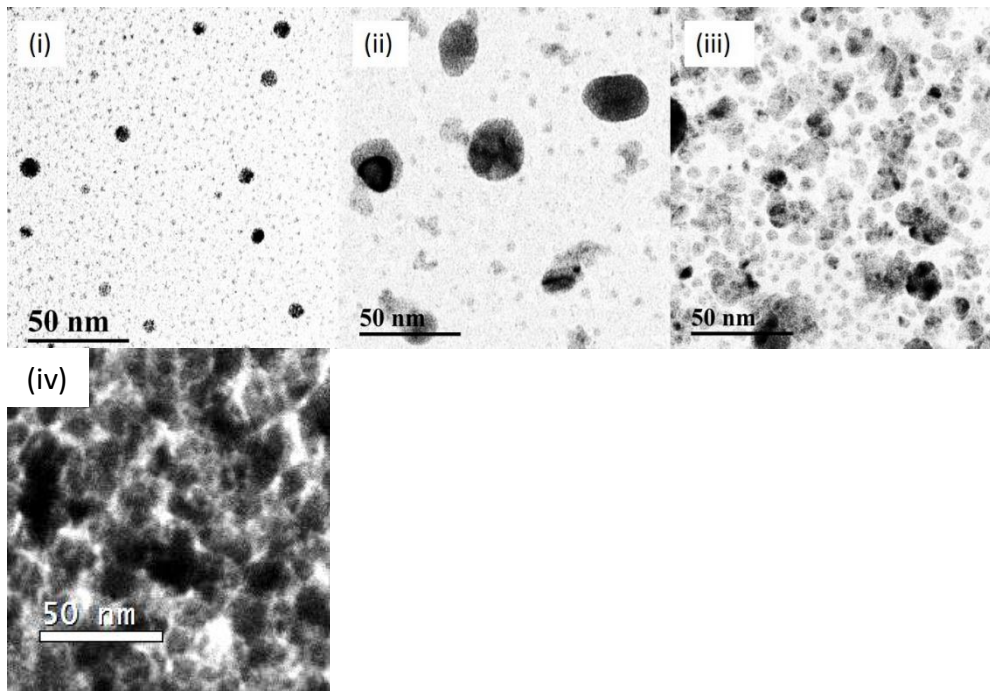


Fig 4.4 Bright field images showing the effect on inter-particle separation distance with concentration of Ag (i) Ag-24%- TiO₂ (ii) Ag-33%- TiO₂ (iii) Ag-45%- TiO₂ (iv) Ag-56%- TiO₂

4.2.4 Optical Properties

Nanocomposite thin films were deposited on quartz substrates to study the absorption spectroscopy. The absorption spectra of TiO₂ and Ag-TiO₂ nanocomposite thin films are shown in Figure 4.5 in the range of 300 nm to 800 nm. A broad SPR peak with low intensity is observed at ~500 nm for the thin film with 33 at.% Ag content. It was redshifted to ~ 525 nm with increasing its intensity for 45 at.% of Ag. This SPR exhibits due to the formation of Ag nanoparticles. The absorption increases with Ag content, and a shift towards higher wavelength value was obtained. Redshift has been observed

while increasing the concentration of Ag from 33% to 45%. From the concentration with Ag 56 at.% the SPR is not observed, but it shows broad absorption. The absorption for this thin film continuously increases with increasing the wavelength. Inset in fig 4.5 shows the graph after subtracting TiO₂ absorption in others. It reveals broad absorption due to Ag nanoparticle in the visible region.

According to Mie theory, the absorption bandwidth and peak position depend on the size of Ag nanoparticles. The diameter of these nanoparticles satisfies the condition ' $2R \ll \lambda$ ' (where R and λ were radius and wavelength, respectively). Under this condition, the electric field of incident light can be assumed to be constant, and the interaction between the nanoparticle and an electric field is governed by an electrostatic field. As the diameter of the particle increases, light loses its capacity to polarise the nanoparticles homogeneously. This inhomogeneous polarisation of nanoparticles causes massive shifts and broadening of SPR. The redshift of SPR for the heavy inclusion of Ag can also be explained by Maxwell-Garnett theory. According to this theory, interparticle interaction among various particles affects the position of SPR. When the condition $d \leq 5R$ is satisfied (where d is the inter-particle distance from the centre to the centre of nanoparticles, and R is the radius of particles), the inter-particle interaction becomes more active. Which leads to complicating extinction spectra which depend on the size and shape of forming an aggregate cluster¹²¹. For the condition $d \leq 5R$, the interparticle separation is much less, and it causes to form clusters of nanoparticles. In this cluster, the nanoparticles do not behave as a single particle; the absorption is governed by cluster not by the individual particle. From Maxwell Garnett theory the effective dielectric constant¹²² of the medium is given by the equation

$$\left(\frac{\varepsilon_{eff} - \varepsilon_m}{\varepsilon_{eff} + \varepsilon_m} \right) = f \left(\frac{\varepsilon_i - \varepsilon_m}{\varepsilon_i + \varepsilon_m} \right) \quad (22)$$

Where ε_{eff} is the effective dielectric constant, ε_i and ε_m is for inclusion metal and matrix dielectric constant, 'f' is the volume fraction of inclusion. From the Drude model, the dependence of local SPR wavelength depends on the dielectric constant of host matrix¹²³ by the following equation

$$\lambda_{sp} = \lambda_p \sqrt{2\varepsilon_m + 1} \quad (23)$$

Where λ_{sp} is LSP resonance wavelength, λ_p is the plasmon wavelength for bulk metal.

Table 3. Bandgap value with a variation of Ag content

Sample Name	Ag Conc. at. %	Band Gap (eV)
a	0	3.05
b	21.4	2.5
c	32.5	2.4
d	44.7	2.25

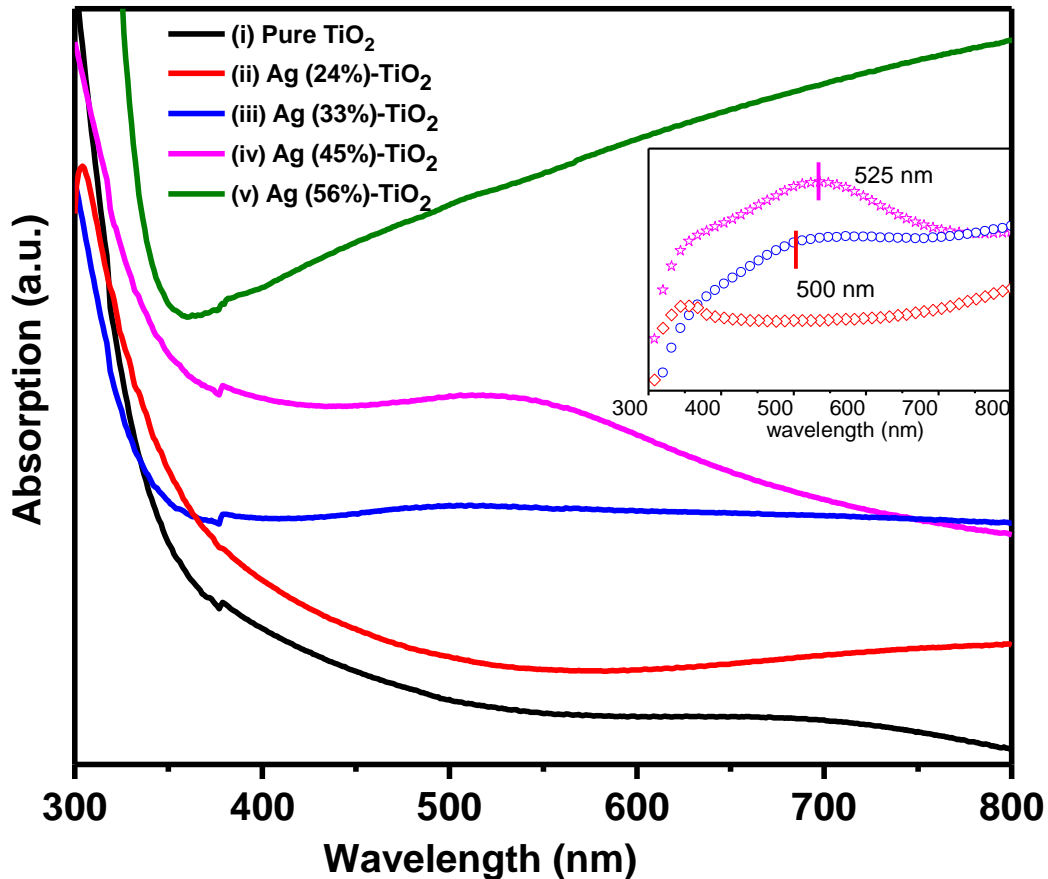


Fig 4.5 Optical absorption spectra of TiO_2 and TiO_2 with varying Ag concentration. (i) pure TiO_2 (ii) Ag-24%- TiO_2 (iii) Ag-33%- TiO_2 (iv) Ag-45%- TiO_2 (v) Ag-56%- TiO_2 . In the inset is TiO_2 absorption subtracted in others.

λ_{spr} strongly depends on the dielectric constant of the host matrix. As the dielectric constant decreases, the local surface plasmon wavelength decreases. As for the amorphous TiO_2 thin film, its dielectric constant is less than the dielectric constant for anatase phase of TiO_2 , when anatase transforms to amorphous form, its dielectric constant value decreases¹²³. The LSPR wavelength of Ag nanoparticles in anatase host

matrix retains on the lower wavelength side rather than in the amorphous host matrix. As in the case of sample (b), the SPR is not observed, it may be because of the effect of the high dielectric constant of host matrix which dominates the position of SPR of Ag nanoparticles to appear in the visible region. For the sample (c) and (d), LSPR is observed at 500 nm and 525 nm as shown in fig 4.5. It was evident from XRD (fig 4.2) that the crystallinity of host matrix decreases and become amorphous for maximum concentrations of Ag. From TEM planar view histogram (fig 4.3), the average nanoparticle size increases from 24 nm to 30 nm for the sample (c) and (d). After increasing the Ag concentrations, the inter-particle separation decreases, which is visible from (fig 4.4), this change in a physical parameter of nanoparticle led to a dominant change in properties due to the dielectric constant of host matrix and observed a redshift of 25 nm with increasing nanoparticle size. The average particle size for Ag 56 at.% decreased by 3 nm compared to Ag 45 at.%. This change is not large enough, but it may be due to the development of irregular shape of Ag nanoparticle for such high Ag content.

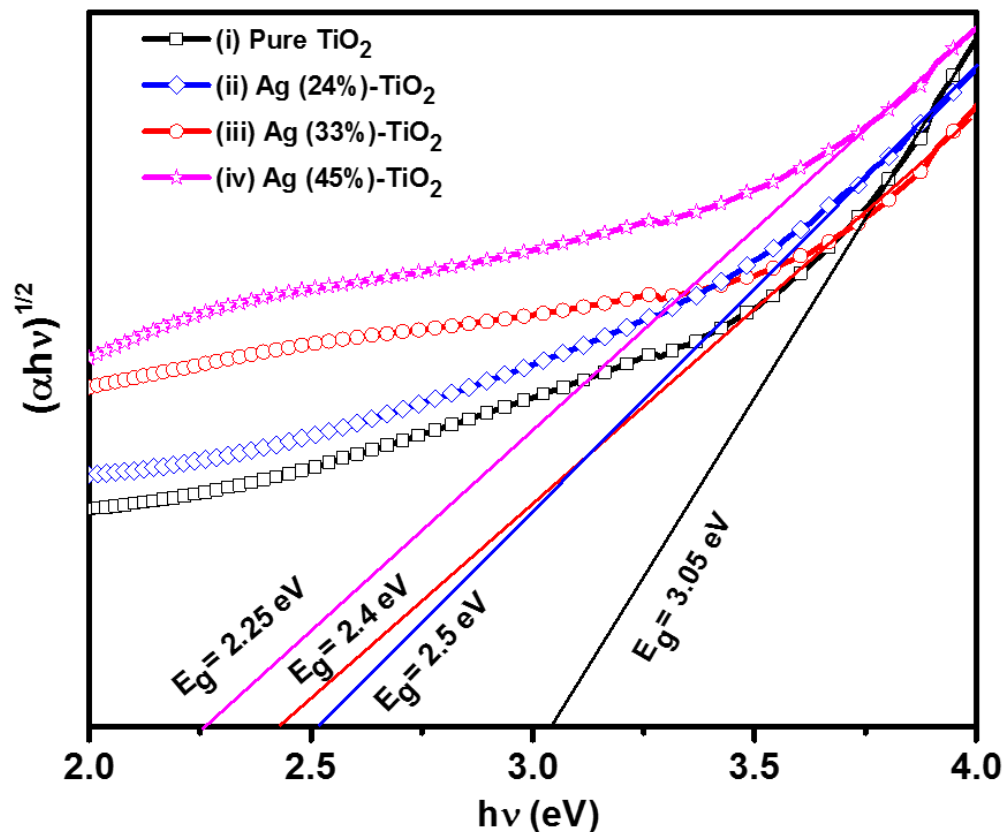


Fig 4.6 Tauc plot using the Tauc relation of obtained optical absorption spectra.

(i) TiO_2 (ii) Ag-24%- TiO_2 , (iii) Ag-33%- TiO_2 , and (iv) Ag-45%- TiO_2

Tauc relation^{105,124} has been used to calculate the band gap. Tauc plot was shown in figure 4.6. We have used this equation for an indirect band gap

$$(\alpha hv)^{1/n} = A(hv - E_g) \quad (24)$$

The band gap of pure TiO₂ has been found to be 3.05 eV which decreases while increasing the content of Ag up to 2.25 eV. The band Eg has been determined as 3.05 eV, 2.5 eV, 2.4 eV, 2.25 eV. As from table 2, the band gap decreases with increasing the concentration of Ag. The redshift of UV-visible absorption spectra shows a reduction in the band gap, which allows the delay in the rate of recombination¹²⁵. The modification in the band gap is due to the interaction between the Ag nanoparticles and TiO₂.

4.2.5 X-Ray Photoelectron Spectroscopy

The elemental and chemical states of the nanocomposites thin films were analyzed by XPS. The spectra of TiO₂ and Ag (45%)-TiO₂ thin films are shown in fig 4.7(a). The stoichiometry of the host matrix was TiO₂. The XPS spectra of Ti (2p), O (1s) and Ag (3d) shown in fig 4.7(b-c). The Ti 2p spectrum of TiO₂ in fig 4.5(b) shows the peaks at 458.75 for 2p_{3/2} and 464.5 eV for 2p_{1/2}. The length between Ti 2p_{3/2} and Ti 2p_{1/2} lines is 5.7 eV, which indicates the existence of Ti⁴⁺ oxidation state¹²⁶. The inset view in fig 4.7(b) shows that the peak position of Ti 2p for Ag-TiO₂ thin films shifted to higher binding energy, on Ti 2p in TiO₂. The shifting of Ti 2p peak to higher binding energy confirms that there is a strong interaction between Ag nanoparticle and TiO₂. Here for the nanocomposite Ag 56 at.-%-TiO₂, Ag content is high, XPS rarely identify the Ti element. So it is hard to find the matrix properties from XPS for this thin film.

Table 4. Ti 2p XPS fitting parameters

Sample	O/Ti	Ti 2p _{3/2}					
		Ti ³⁺			Ti ⁴⁺		
		B.E. (eV)	FWHM (eV)	Area (%)	B.E. (eV)	FWHM (eV)	Area (%)
Pure TiO ₂	1.95	457.76	1.3	2.2	458.8	1.2	97.8
Ag (45%) - TiO ₂	1.89	458.3	1.3	72.4	458.73	1.2	27.6

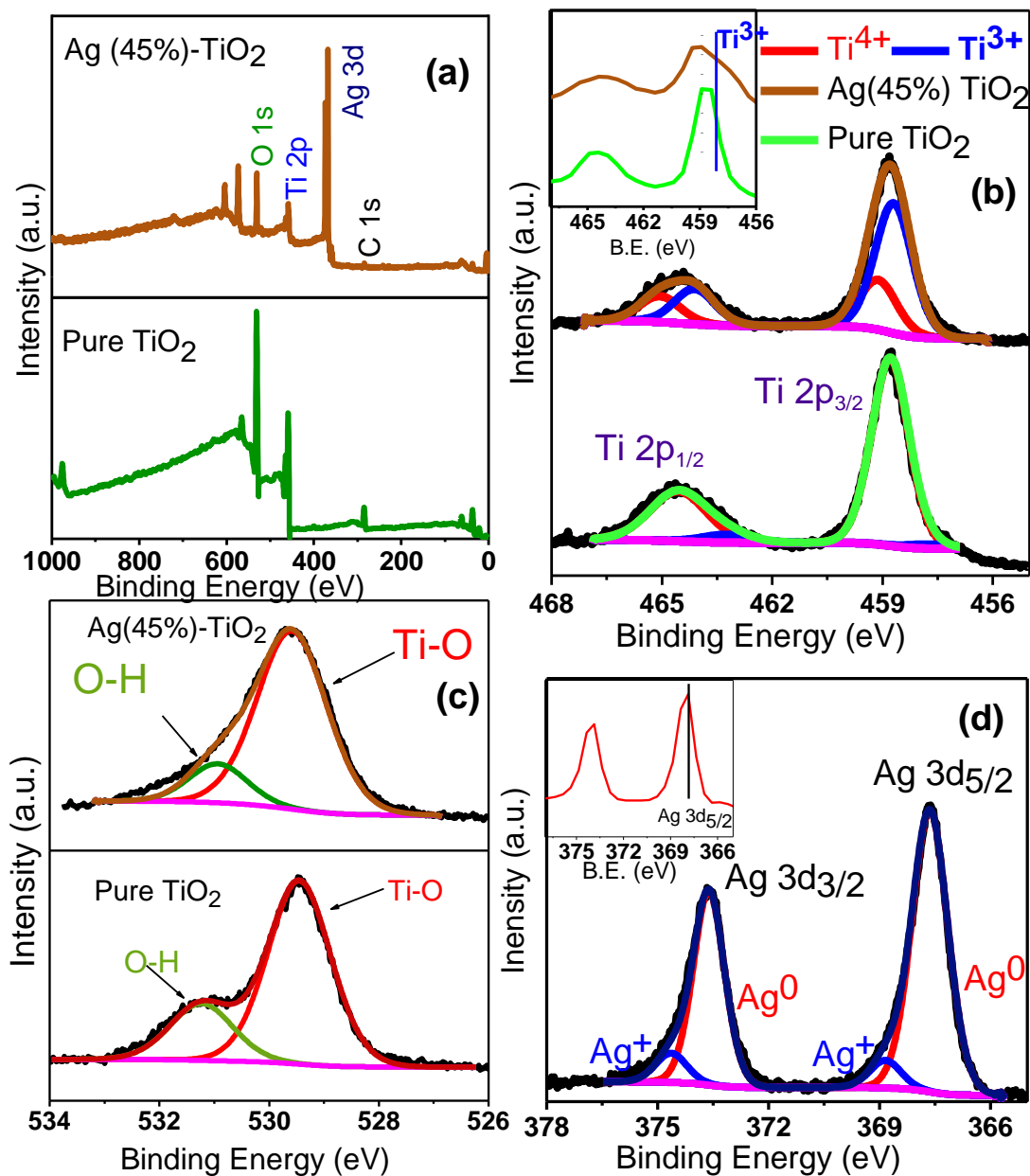


Fig 4.7 XPS (a) Full scan (b) Peak fitting of Ti 2p XPS of pure TiO₂ and Ag (45%)-TiO₂ thin films with inset of Ti 2p from full scan (c) O 1s XPS spectra and (d) Ag 3d spectra Ag (45%)-TiO₂ thin films with inset of Ag 3d from full scan.

The software Casa XPS has been used to fit and deconvolution of different peaks. The peak position, FWHM and concentration of Ti³⁺ and Ti⁴⁺ species were listed in Table 4. The presence of Ti³⁺ increases with Ag content and due to their interaction results in the narrowing the band gap which may be advantageous to heighten the photocatalytic

activity¹²⁶. The existence of Ti^{3+} ascribes to defects energy levels. These defects energy levels improve the photocatalytic activity¹²⁶.

From fig 4.7(c), it is clear that the asymmetric and broad spectra of O 1s indicate more than one component, which was fitted by Casa XPS and Ti-O position is 529.47. The other peak is of hydroxyl groups. Fig 4.7(d) shows two peaks at in Ag 3d spectrum, which is at 367.8 eV, 373.7 eV and represents Ag 3d_{5/2} and Ag 3d_{3/2}. The position of these peaks is lower than their bulk value, which is probably due to the migration of electrons from TiO₂ to Ag nanoparticles. A shift to lower binding energy reveals a strong interaction between Ag nanoparticles and TiO₂ thin film. From the fig 4.7(a)-(d) it can be determined that at this high concentration only 6% of Ag got oxidized, and 94% of Ag is in free of any chemical bonding and forms nanoparticles.

High doping of Ag content in TiO₂ affects its crystallinity, from XRD it is clear that the crystallinity decreases with Ag content. The SPR position and intensity was affected by nanoparticle size, distribution, inter-particle separation and crystallinity of host matrix. As seen from TEM images in fig 4.3, Ag nanoparticles indicate nonuniformity in size and irregular in shape which may be the reason for broad absorption, because the natural resonance frequency was different for nanoparticle which differs in shape and size. The redshift was observed due to increment in particle size of the nanoparticle. There was the interaction of Ag nanoparticle with TiO₂ which was confirmed by XPS, Ti^{3+} charge state arises. This interaction affects the band gap of nanocomposite thin film and band gap value decreased from 3.05 eV to 2.25 eV which was clear from band edge absorption in fig 4.5; the edge shifted to a higher wavelength. This band gap lies in the visible region and shows good absorption in the visible region. Ag nanoparticles trap electron from TiO₂ and act as an electron acceptor and reduce the recombination rate of an electron with a hole. The increment in the Ti^{3+} charge states, good absorption in the visible region and lowering the recombination rate of an electron with a hole, made these properties to use for photocatalytic active material. There is an important role of Ti^{3+} defect sites and hence the LSPR for photocatalytic activity. In our case, the Ti^{3+} sites increased up to 72.4% by heavy doping and have broad SPR at 525 nm with band gap 2.25 eV. These values are important because these affect the nanocomposite thin film to be more active in the visible region for the photocatalytic process.

4.3 Synthesis of nanocomposite thin film by Ion implantation

Ion implantation technique was used for a long time to modify many properties^{127–129}. Optical properties are one of them. Ion implantation can also be used to tune the SPR (Surface Plasmon Resonance) properties of nanoparticles by selecting the fluence, energy, and ion^{127,130}. By implantation technique, nanoparticle's can be synthesized easily inside the implant layer with desired depth. As the ion is injected with energy into the target, it creates structural changes in the target material. Defects were induced by implantation; sometimes these defects have shown potential application along with nanoparticle properties in various fields. In this process for the formation of nanocomposite thin film metal ion of specified energy was implanted into the target material. The combination of metal and target material modifies the optical properties of nanocomposite thin film. If the dose of implanted metal was increased and if it is above its dissolve value into the target, then metal atom agglomerate and combine to form a nanoparticle. The size, shape, distribution and surrounding environment of these nanoparticle, effects the LSPR properties of nanocomposite thin film^{121,131,132}. If implanted metal is among noble metals and the target material is metal oxide, then the nanocomposite thin film shows a great enhancement in properties, like optical sensing, photo-catalysis^{87,121}, antibacterial activity^{121,133}, SERS (surface-enhanced Raman scattering)^{100,134}. Ag nanoparticle shows notably strong LSPR in the visible region, which enhances its uses in electronic and cosmetic industries. For the target material, we choose TiO₂ matrix. By selecting the above both metal and metal oxide, shows bi-functionality properties.

In this section, Ag⁻ ions were implanted in the matrix of TiO₂ at different fluences and further these films were characterized by UV-visible spectroscopy, XPS (X-ray photoelectron spectroscopy), fluorescence spectroscopy. Some of the implantation experiments have shown that after implantation silver got oxidized completely^{135–137} but here we have successfully synthesized nanoparticles of Ag in TiO₂ matrix without using any heat treatment to the thin film.

4.3.1 Experimental detail

Thin films of TiO₂ have been deposited at power 75W by RF sputtering method. The target of TiO₂ has been used, which was prepared using TiO₂ powder of Alfa Aesar

(99.9%). The substrates were cleaned ultrasonically in D.I. water and acetone. Further, these were washed in TCE (trichloroethylene), methyl alcohol and acetone. The target to the substrate to target distance was 13 cm, and the vacuum is 1.2×10^{-6} torr. Argon gas has been used and the vacuum during deposition is 7×10^{-3} torr. The thin film was deposited for 45 min, and the substrate holder was rotated for uniform deposition with the help of DC motor. For the inclusion of silver metal in TiO_2 matrix silver negative ion was implanted at energy 120 keV and fluence 3×10^{14} , 1×10^{15} , 3×10^{15} , 1×10^{16} , 3×10^{16} ions/cm². No thermal treatment was given to the substrate during and after deposition and after implantation.

To measure the thickness of the thin film on a quartz substrate, Rutherford backscattering (RBS) has been done at IUAC New Delhi. The detector angle was 165° with beam 1.8 MeV He^+ . XRD measurement has been done by Panalytical X-pert Pro X-ray diffractometer to identify structural properties. To determine optical properties, we have the implanted, and pristine thin films were characterized by Perkin Elmer UV-visible spectroscopy and fluorescence spectroscopy. X-ray photoelectron spectroscopy (XPS) (Omicron ESCA) was used to quantify the stoichiometry and interaction of silver nanoparticle with TiO_2 . The monochromatic source of Al anode with energy 1486.7 eV has been used.

4.3.2 Composition and Structural Studies

For implant depth profile of 120 keV Ag⁻ ion in TiO_2 matrix, we have used a tridyn¹³⁸ simulation software. The concentration of Ag was given relative to with respect to the Ti. Fig 4.8 shows the ion distribution relative to depth for the thin film implanted with dose 1×10^{16} ions/cm² and 3×10^{16} ions/cm². The maximum concentration for dose 1×10^{16} ions/cm² and 3×10^{16} ions/cm² of Ag⁻ ion is 10% and 25% respectively.

RUMP program has been used to determine the thickness of the target thin film of TiO_2 . The thickness of the thin film is 62 nm. The simulated RBS spectrum is shown in fig 4.9. XRD spectroscopy of pristine and implanted thin film is shown in fig 4.10. The as-deposited thin film is amorphous as there was no diffraction peak observed. No diffraction peak was obtained after implantation.

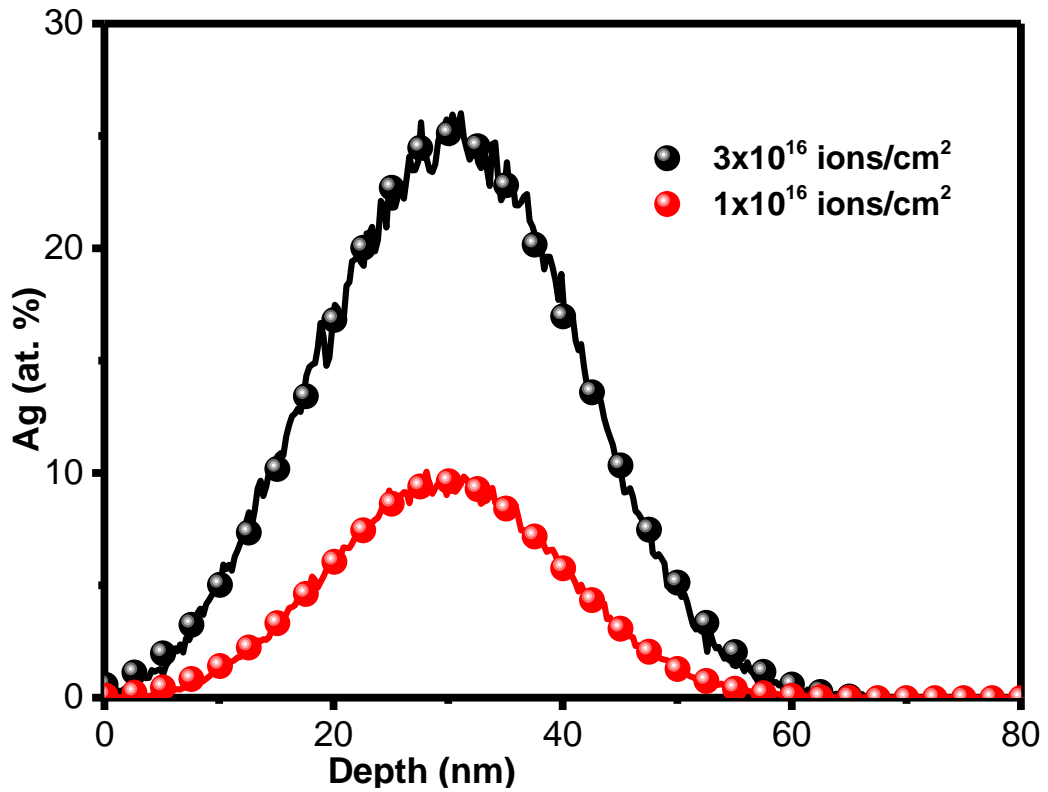


Fig 4.8 Evaluated depth profiles of distribution of Ag⁻ ions implantation in TiO₂ relative to depth.

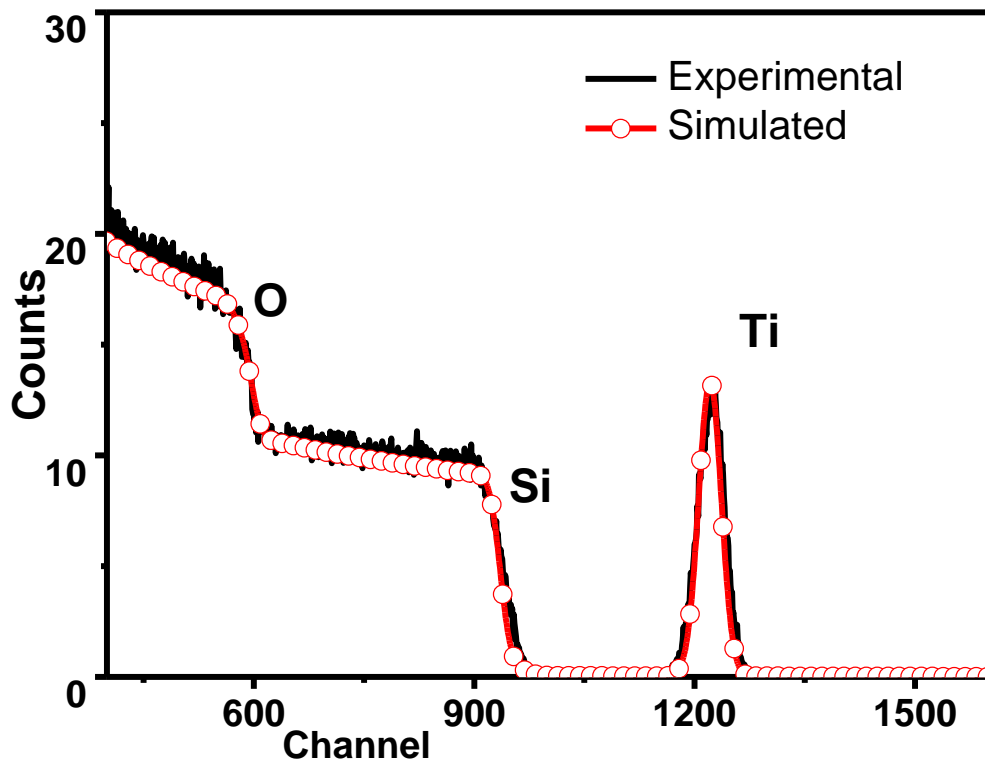


Fig 4.9 RBS simulation of pure TiO₂ thin film deposited on quartz substrate

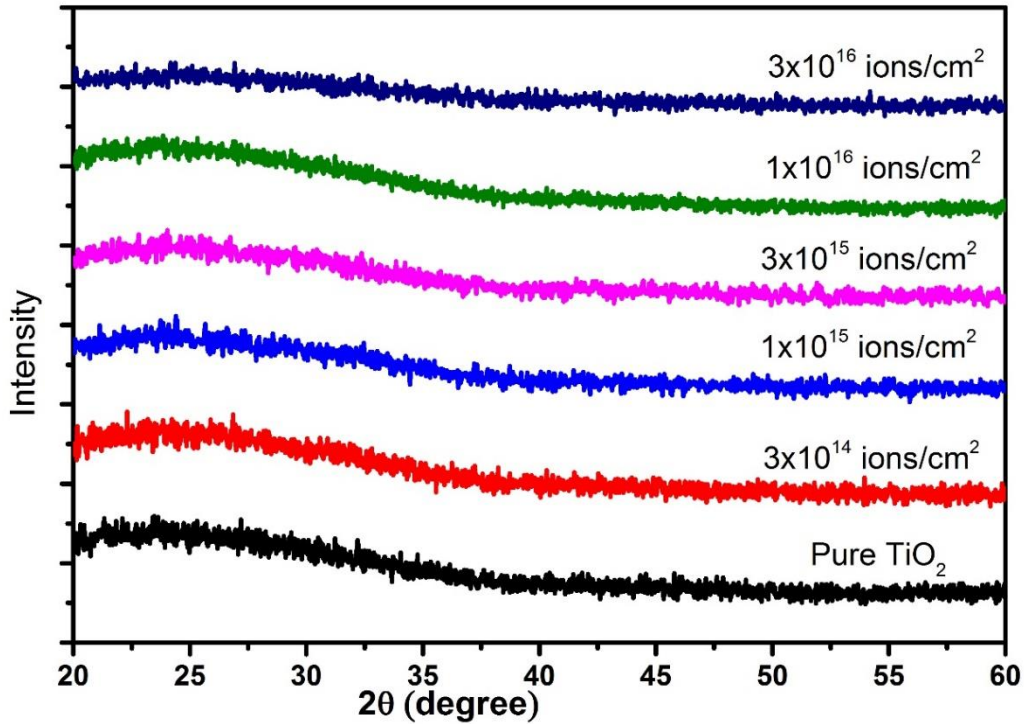


Fig 4.10 XRD pattern of pristine and implanted TiO_2 at different fluences

4.3.3 Absorption and fluorescence spectroscopy

The pristine and implanted thin films were studied by UV-visible absorption and fluorescence spectroscopy to determine the modifications of its optical properties. The

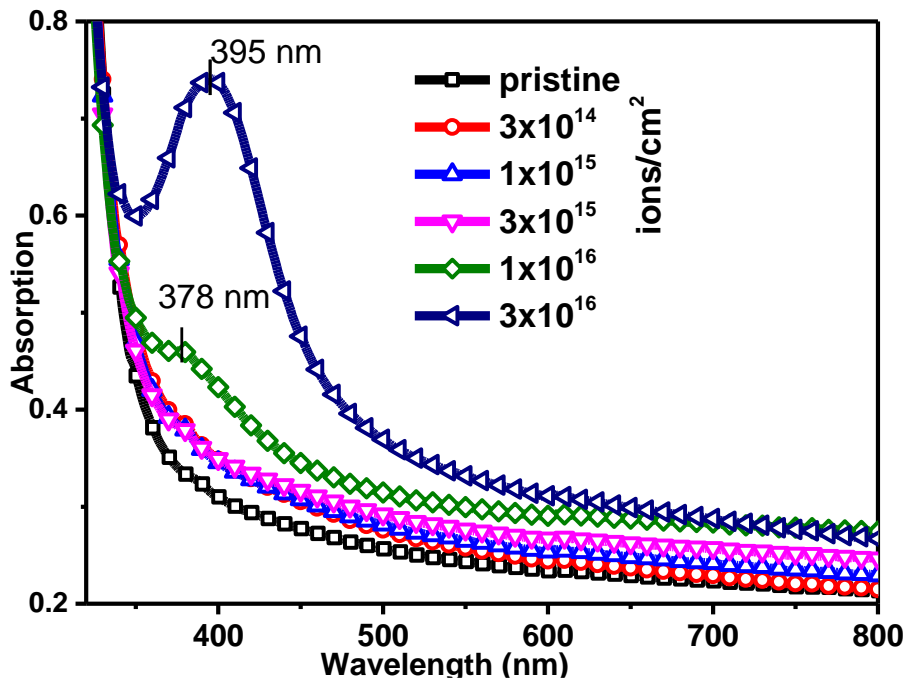


Fig 4.11 UV-visible absorption spectroscopy of TiO_2 and implanted composite thin film

UV-visible absorption in the range 300-800 nm is shown in fig 4.11. It can be seen that initially no SPR has been observed for the implanted thin film up to the fluence 3×10^{15} ions/cm². However, for the fluence at 1×10^{16} ions/cm², we have observed a low-intensity SPR at 380 nm. At fluence 3×10^{16} ions/cm², a strong LSPR has been observed which was shifted to 395 nm with noticeable intensity. No changes in the absorption edge of TiO₂ was observed. Also, there was an increment in absorption after 450 nm.

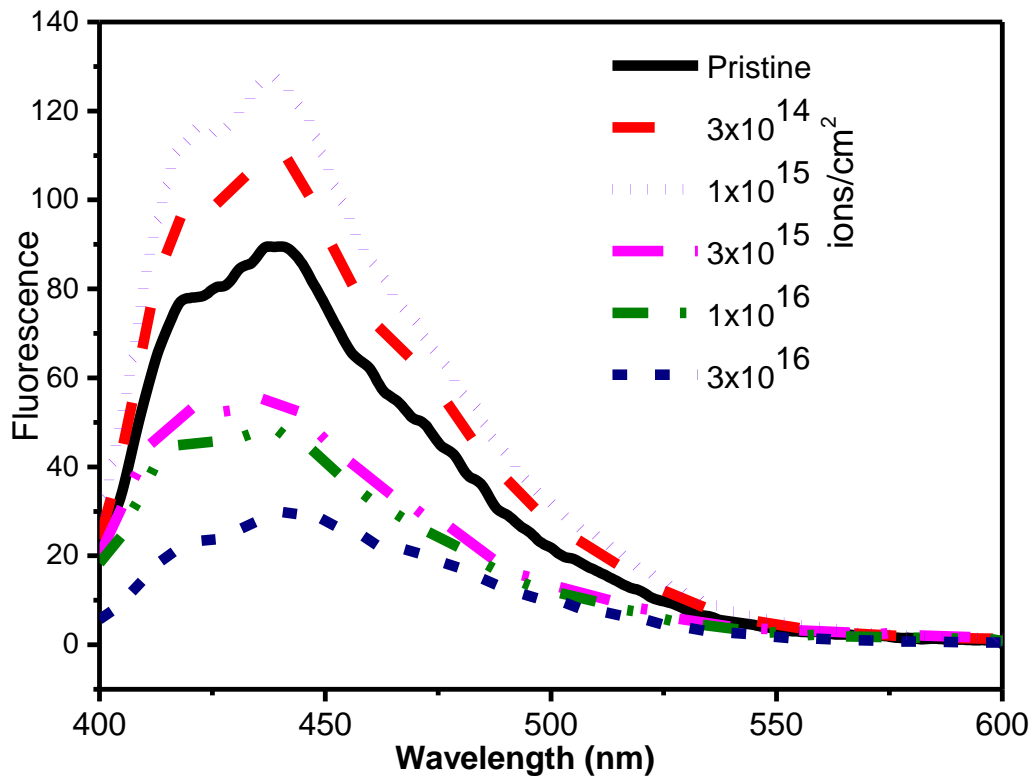


Fig 4.12 Fluorescence spectroscopy of pristine and implanted thin film fluence 3×10^{14} , 1×10^{15} , 3×10^{15} , 1×10^{16} , 3×10^{16} ions/cm²

Fluorescence spectra are shown in fig 4.12. As the excitation beam wavelength was 365 nm initially when the implantation dose is increased from 3×10^{14} ions/cm² to 1×10^{15} ions/cm² the fluorescence properties of the composite thin film also increased but for dose greater than 1×10^{15} ions/cm² the fluorescence intensity decreases with increasing the implantation dose.

4.3.4 X-Ray Photo-electron Spectroscopy

The chemical states of elements Ti, O and Ag were analyzed by XPS. High-resolution spectra of Ti, O and Ag were analyzed for the pristine and implanted thin film at fluence 3×10^{16} ions/cm². These results were given in fig 4.13 and calculated binding energies

were given in table 4 for pristine thin film the Ti 2p_{3/2} and Ti 2p_{1/2} located at 458.8 eV and 464.4 eV respectively. Highest fluence implanted thin film have Ti 2p_{3/2} and Ti 2p_{1/2} located at 458.35 eV and 464.2 eV respectively. After the implantation, the peak separation between 2p_{1/2} and 2p_{3/2} was increased by value 0.25 eV and shifting of the peak to lower binding energy of Ti was observed by 0.45 eV value. After the ion implantation, the increment in intensity observed for Ti³⁺ charge state.

The O1s peak is located at 529.3 eV, peak at 531.4 eV shows the hydroxyl group oxygen at the surface of thin film. For the fluence there is a peak of O 1s is obtained due to the defects created by ion implantation in TiO₂.

From fig 4.8 depth profile of Ag implanted in TiO₂, it has been observed that for both fluence 1×10¹⁶ and 3×10¹⁶ ions/cm² the highest concentration of Ag is 10 % and 25 % respectively. For such high concentration, the Ag is above its solubility limit and Ag agglomerates to form nanoparticles. While increasing the implantation dose the size of the nanoparticle increases but there is a structural modification in the matrix of TiO₂, due to the combining effect of these results redshift and increment in the intensity of LSPR. The size and concentration of Ag nanoparticles depend on the implanted dose, so for the dose ≥ 1×10¹⁶ ions/cm², the size and concentration will be less than these values has for high dose.

As it is clear from absorption graph in fig 4.11, by increasing the implantation dose, increment in absorption observed but up to the fluence 3×10¹⁵ ions/cm², no LSPR has been observed that may be due to the low concentration of silver or agglomeration of silver is very low and they form very small nanoparticles. For the dose 1×10¹⁶ and 3×10¹⁶ ions/cm², the concentration of silver was increased to 10% and 25% respectively at depth 30 nm, which is more than sufficient to form silver nanoparticles and results in show good intensity of LSPR. The redshift in LSPR has been observed by the value 17 nm, which is due to increment in the size of the nanoparticles. The size of the nanoparticles and dielectric constant of matrix decides the shifting in LSPR. Increasing the nanoparticle size, LSPR shifts to the higher wavelength.

From the fluorescence spectroscopy, the pure TiO₂ thin film and implanted thin film shows the origin of fluorescence spectroscopy. The occurrence of fluorescence properties is due to the presence of defects in the thin film. Due to defects of oxygen vacancies deep donor level creates and deep acceptor level creates due to the hydroxyl group present on the surface of the thin film¹⁰⁶ due to these oxygen defects lower charge

states of Ti^{3+} and Ti^{2+} creates¹³⁹. These donor level, acceptor level and lower charge states of Ti play a part in the fluorescence properties. There is a clear indication of interaction between Ag nanoparticles and TiO_2 matrices. When increasing the dose, the fluorescence intensity of composite thin film increases. It is because by implanting Ag

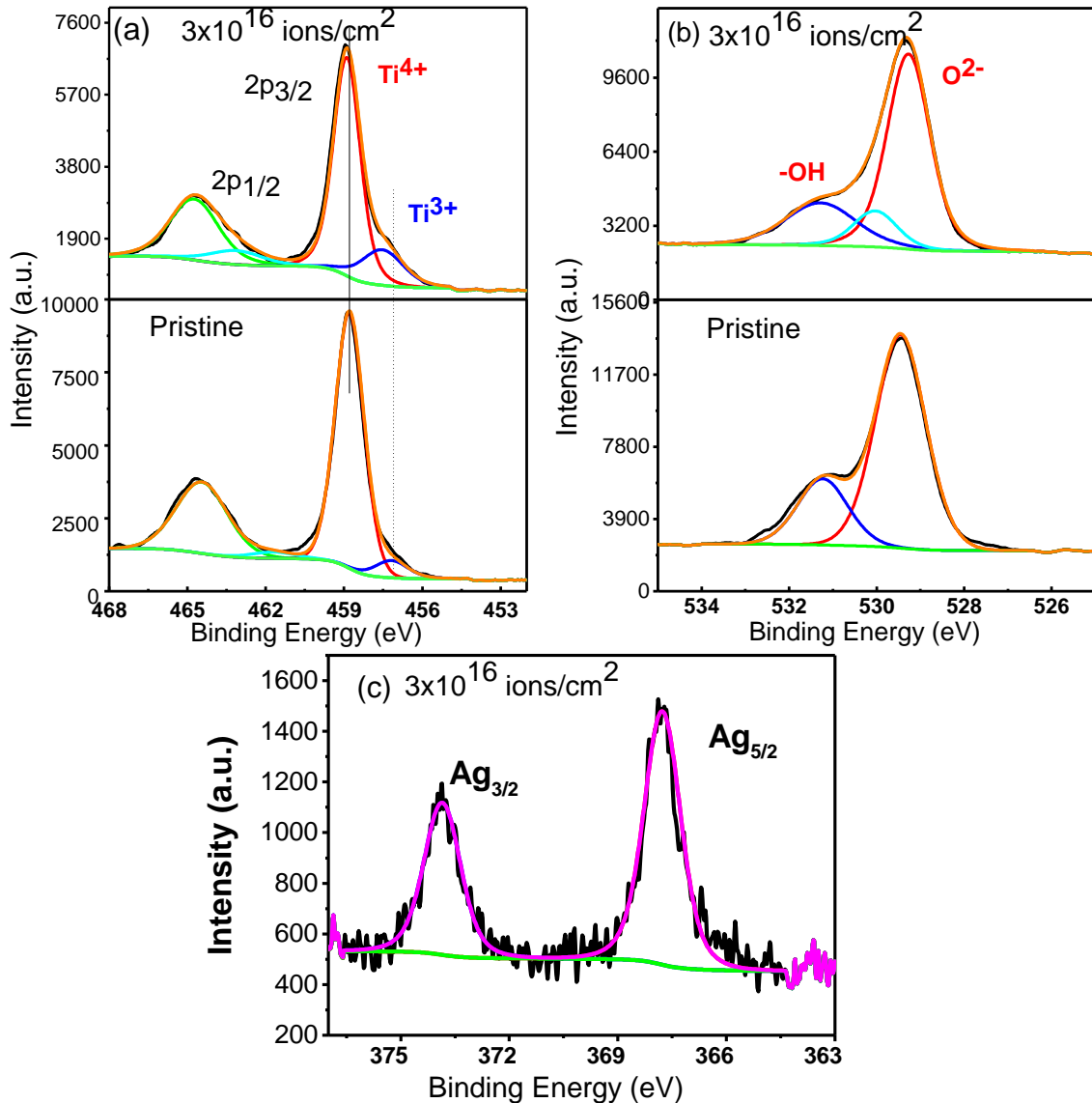


Fig.4.13 XPS of pristine thin film and implanted thin film for the fluence 3×10^{16} ions/cm². (a) Ti 2p core spectra, (b) O 1s core spectra (c) Ag 3d spectra for fluence 3×10^{16} ions/cm²

in the TiO_2 thin film the defects were created and those defects result in an enhancement in fluorescence properties. However, this was observed only up to the fluence 3×10^{15} ions/cm², for the dose greater than this, defects were also increased, but there is one more process occurs which results in decreasing the fluorescence intensity. That is

because of increasing the implantation dose the Ag starts agglomeration and forms silver nanoparticles surrounded by TiO₂ matrix. There is an interaction between these two in which TiO₂ transfer its electronic charge to the silver, which results in reduced intensity. The intensity decreased continuously up to the highest dose 3×10¹⁶ ions/cm². This interaction between Ag and TiO₂ was also supported by XPS analysis. From XPS implanting at dose 3×10¹⁶ ions/cm², the increment in Ti³⁺ states has been observed which can be explained by an increment in defects and also increment in the interaction of Ag with TiO₂. The increment in the interaction of Ag is also focused here because we have obtained Ag 3d_{5/2} peak position at 367.7 eV, which is lower than its bulk value. Also, the Ti⁴⁺ charge state is shifted to higher binding energy which is also evidence for strong interaction. This strong interaction between nano-particles and TiO₂ the recombination rate of electron and hole was reduced.

Table 5. XPS analysis for core spectra of Ti and O.

Sample	Ti 2p, eV		Ti 2p Peak separation, eV	O 1s, eV	
	2p _{3/2}	2p _{1/2}		O ²⁻	-OH
Pure TiO ₂	458.8	464.4	5.6	529.3	531.4
3×10 ¹⁶ ions/cm ²	458.9	464.74	5.85	529.3	531.4

4.4 Conclusion

The structural, morphological, optical absorption and electronic structures of Ag nanoparticles in TiO₂ matrices with a variation of Ag concentration have been investigated. A broad SPR at 525 nm was observed for 45% Ag concentration without any additional treatments during deposition and post-deposition. The HR-TEM images show a nearly uniform distribution of the Ag nanoparticles in the TiO₂ matrix. There is a combination effect of crystallinity of TiO₂, distribution of nanoparticles and interparticle separation on SPR. The band gap can be tuned between 3.05 eV to 2.25 eV with a variation of Ag concentration. This lowering in band gap value was explained by XPS, which was due to the strong interaction of Ag nanoparticle with TiO₂. With the interaction of Ag nanoparticle, some lower energy levels produced in TiO₂ band gap such as Ti³⁺, the energy levels of Ti³⁺ is near to valence band than Ti⁴⁺. The Ti³⁺ concentration was increased up to 72.4% for Ag (45 at. %). By ion implantation

technique the Ag nanoparticles in the matrix of TiO₂ was synthesized. Also, we report here that Ag is in a metallic form which shows strong LSPR due to Ag nanoparticles in the visible region. As other reported silver oxide by ion implantation. After implantation, the interaction between nanoparticle of Ag and matrix TiO₂ has been observed. This result show decrement in recombination rate of electron and hole pair. This reduction in recombination rate helps to improve properties like photocatalysis and antibacterial activities. Both deposition technique (RF sputtering and Ion implantation) used to modify the properties of nanocomposite thin film with the variation of silver concentration. In both cases, it has been identified that due to the interaction of silver nanoparticle with TiO₂ matrix helps in lowering the recombination rate of electron and hole pair. The band gap improvement was observed only in RF sputtering deposited thin films whereas a well defined LSPR was observed for the ion implantation thin film.

Chapter Five

Modifications in Ag-TiO₂ thin film by ion irradiation

5.1 Introduction

The modifications of optical and structural properties of nanocomposite thin film by altering the shape and size of the nanoparticle are necessary. This requirement helps to achieve the desired properties to use nanocomposite thin film as a potential application. Regarding this modification swift heavy ion irradiation proved itself a unique tool to control the engineering of nanoparticles. This chapter is based on the modification of nanocomposite thin film by SHI irradiation. This chapter is divided into two parts in which different concentration of Ag in TiO₂ matrix has been used for ion irradiation. In this chapter, the aim is to study the SHI irradiation of Ag metal nanoparticles (high filling fraction) embedded in a TiO₂ matrix. The high filling fraction of metal nanoparticles in TiO₂ matrix is interesting because, at higher concentration, structural properties of the matrix remain unaffected on ion-irradiation. Due to SHI irradiation, the temperature rises in nanocomposite thin film not enough to modify matrix properties (as the filler concentration is high). However it is sufficient to induce the modification of the properties of metal nanoparticles, this ascribed to the lower thermal conductivity of metal nanoparticles than that of matrix^{140,141}. The experimental results were compared with simulated results and explained the position and existence of LSPR.

5.2 SHI irradiation of Ag (45 at.%) -TiO₂ nanocomposite thin film

5.2.1 Experimental detail

Ag-TiO₂ nanocomposite thin films have been deposited on quartz, silicon and glass substrate with Ag content 45 at.%. The substrates were sequentially cleaned with acetone, methanol and Tri-Chloro Ethylene (T.C.E.). A lab-made TiO₂ target (Alfa Aesar ~ 99.9%) has been used. The size of the target holder and substrate holder was 2 and 5 inches respectively. Before deposition, the vacuum was 1.3×10^{-6} torr. For

sputtering, argon gas medium has been used at pressure $\sim 8 \times 10^{-3}$ torr and flow of Ar to the sputtering chamber was 11 sccm. The thin films were deposited at power ~ 75 watts and room temperature. The substrate holder was rotated with the help of a DC motor. Ag-TiO₂ thin films were irradiated by 90 MeV Ni ion at different fluences 1×10^{12} , 3×10^{12} , 6×10^{12} , 1×10^{13} , 3×10^{13} ions/cm² by Pelletron 15 UD accelerator at IUAC New Delhi. The thickness of thin film and concentration of Ag were calculated by Rutherford Backscattering spectrometry (RBS). The angle between the detector and 2 MeV He⁺ incident beam was 165°, this facility was used at IUAC, New Delhi. X-ray diffraction (XRD) measurements were carried out using Panalytical X-Pert Pro X-ray diffractometer to determine the crystallinity of thin films. For optical properties measurement, irradiated nanocomposite thin films have been characterized by UV-visible absorption spectroscopy using a dual beam Hitachi photo spectrometer and a fluorescence spectrometer. Morphological studies of pristine and irradiated thin films have been done using HR-TEM (Tecnai G2 20 FEI S-Twin 200kV). To simulate the absorption and electric field intensity, we have used Lumerical FDTD software¹⁴².

5.2.2 Compositional, structural and morphological studies

RBS spectrometry was done for the Ag-TiO₂ thin films deposited on silicon. The thickness, concentration and depth profile were determined by RUMP¹⁰² program. It was found to be thickness ~ 45 nm and concentration 45 at.%. The simulated RBS is shown in fig 5.1(a) and depth profile in fig 5.1(b), which confirmed that in nanocomposite thin film only Ti, Ag and O were present. From depth profile Ag is assumed to be distributed evenly through the depth of the thin film.

XRD pattern of pristine and SHI-irradiated Ag-TiO₂ nanocomposite thin films is shown in fig 5.2. The peak position of silver was observed at 38.1° and 44.3° which was identified by matching with JCPDS ref no. 87-0720. Initially for the fluence 1×10^{12} ions/cm² silver got amorphized and with increasing the fluence from 3×10^{12} to 1×10^{13} ions/cm², the silver nanoparticles show recrystallization.

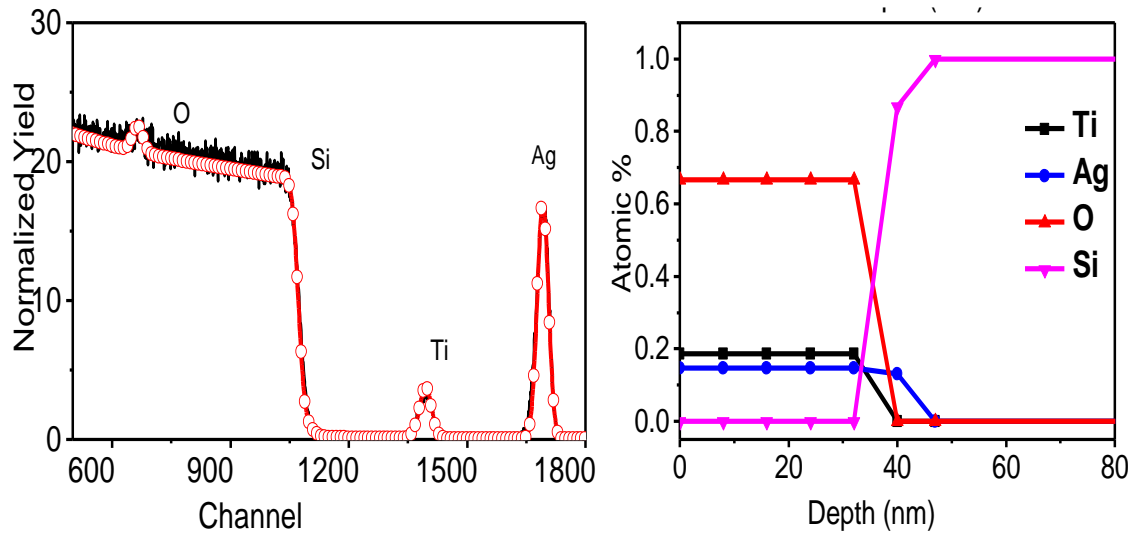


Fig 5.1 (a) RBS of Ag (45 at.%) -TiO₂, simulation shown with line and experimental data with the symbol. (b) Depth profile of nanocomposite thin film.

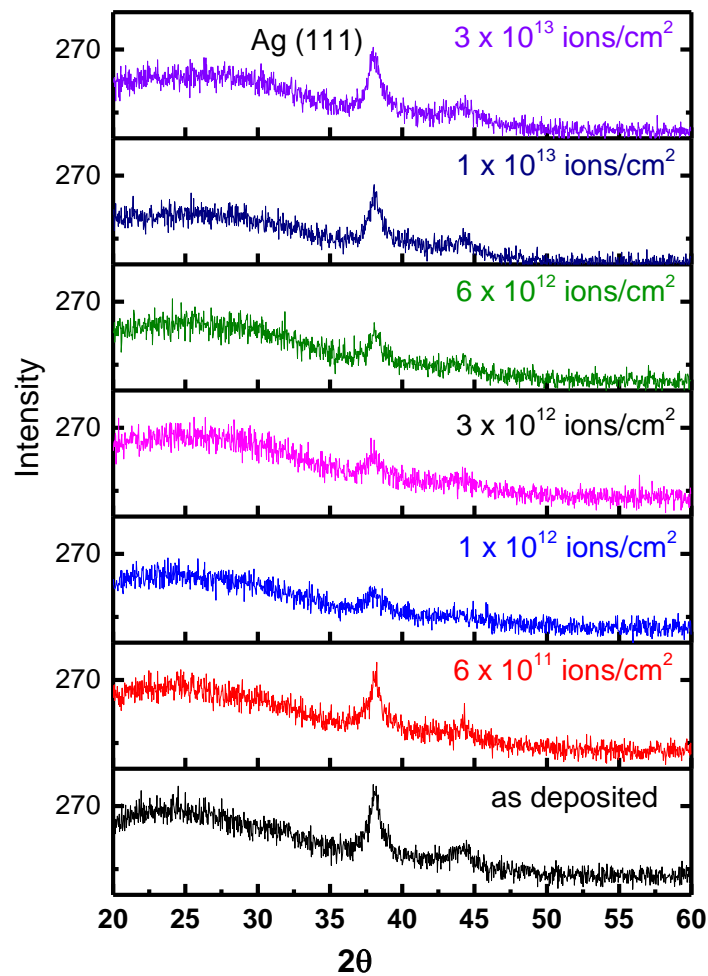


Fig 5.2 XRD of as-deposited and 90 MeV Ni ion irradiated thin film at different fluences

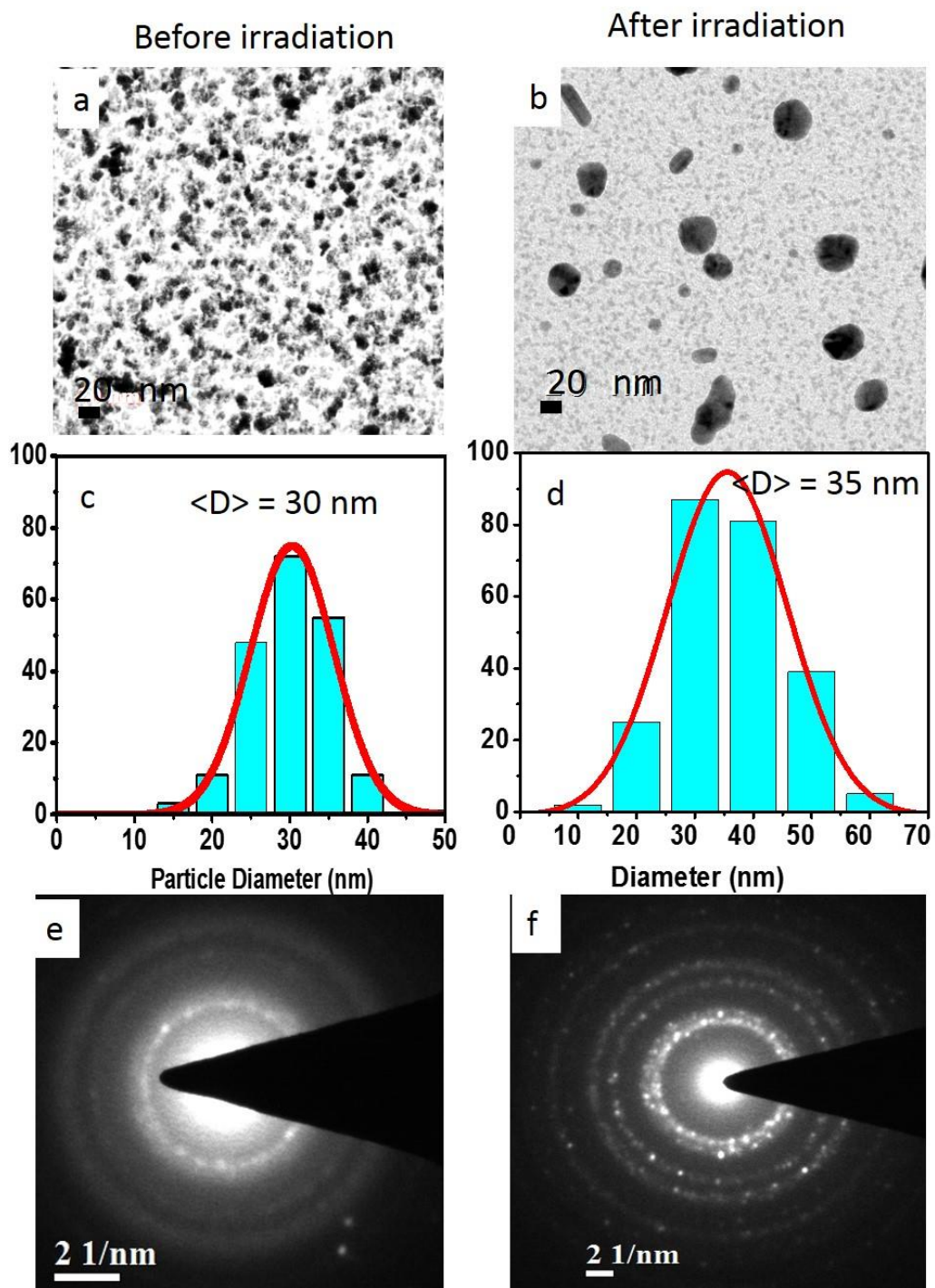


Fig 5.3 Planer view, bright field TEM images are shown in (a),(b) with SAED pattern in (e),(f) and (c),(d) show a histogram of particle size distribution

Morphological studies were done by TEM analysis; analysis is shown in fig 5.3. The topographical view for as-deposited and ion irradiated thin film on TEM grid is shown

in Fig 5.3(a),(b). Fig 5.3(c),(d) shows the particle size distribution. The average particle size was calculated considering the ~ 200 nanoparticles. The average nanoparticle size fitted with Gaussian distribution function is 30 nm for pristine thin film and 35 nm for irradiation thin film at fluence 3×10^{16} ions/cm². After irradiation, the average particle size increased by 5 nm. It is seen in fig 5.3(a),(b) that the interparticle separation is drastically affected by the ion irradiation, which directly affects the optical properties of the thin film.

As the deposited thin film shows no diffraction peak corresponding to TiO₂, this amorphous nature of TiO₂ in XRD is supported by SAED pattern where broad ring pattern was observed in fig 5.3(e). After irradiation at different fluence, no crystallization observed in TiO₂. However, the crystallinity of silver was affected by ion irradiation as seen in fig 5.10, the diffraction peak intensity varies with the fluence. After ion irradiation crystallinity of silver was increased which is seen in the SAED pattern Fig. 5.3(f).

5.2.3 Absorption spectroscopy and FDTD simulation

Nanocomposite thin films deposited on glass were used to study the optical properties. Fig 5.4 shows the UV-visible absorption graph. Initially, a very broad SPR was observed in region 350 nm to 550 nm. However, it shows no peak as it is a continuous absorption. As the irradiation fluence is increased, absorption in the region 400 nm to 650 nm increases, which were assumed to be due to SPR. For the highest fluence 3×10^{16} ions/cm², a broad SPR peak was observed at 530 nm. A dip in the absorption between region 350 nm to 400 nm was observed which is further explained with the TEM results. Fluorescence study has been done for the pristine and irradiated thin film shown in fig 5.5. Initially, the intensity increases with the irradiation fluence, but after the fluence 6×10^{11} ions/cm² the fluorescence intensity decreases continuously with increasing the fluence.

In the present case, the filler material is silver, and the dielectric matrix is TiO₂. Here for Ag-TiO₂ (Ag at. 45%) as-deposited thin film (pristine film), the interparticle separation is minuscule compared to the nanoparticle size, as clearly seen in Fig 5.3(a). This minuscule inter-particle separation results in lying the SPR in the infrared region and broadening of SPR¹²¹. After the irradiation at 90 MeV Ni ion, the absorption

increases in the visible region. For the fluence 1×10^{12} to 3×10^{16} ions/cm², an increment in absorbance in the region 400 – 650 nm observed.

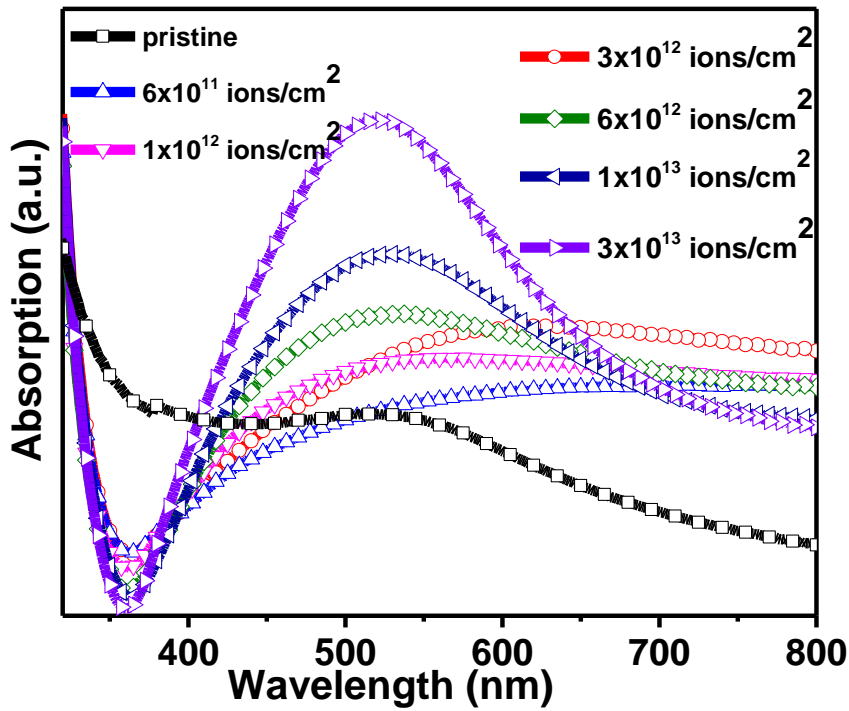


Fig 5.4 Optical absorption spectra of 90 MeV Ni ion irradiation of nanocomposite thin film

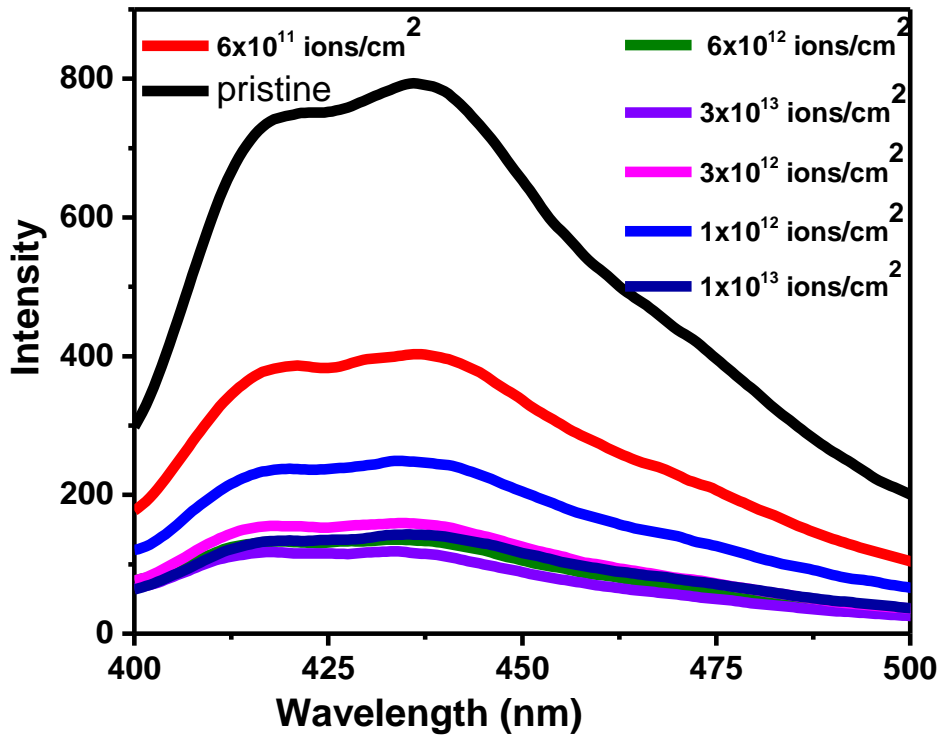


Fig 5.5 fluorescence spectroscopy of pristine and irradiated thin films at different fluences

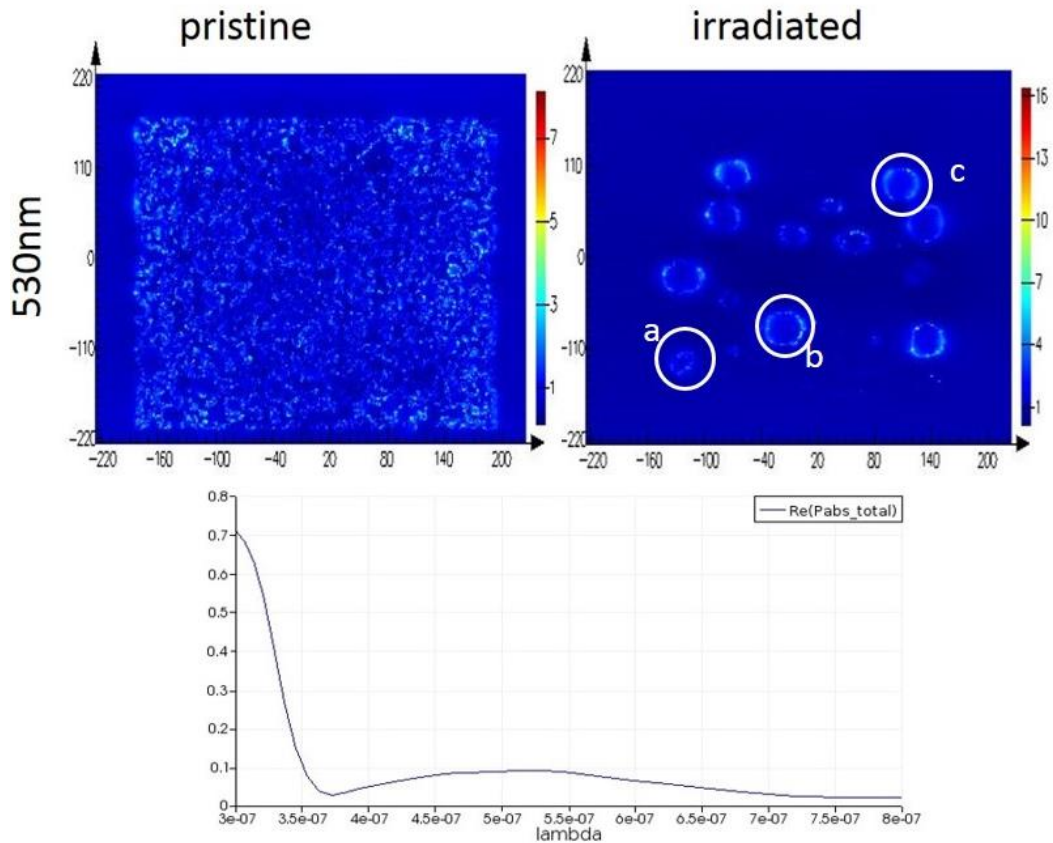


Fig 5.6 FDTD simulation of pristine and 3×10^{13} ions/cm² irradiated thin film at 530 nm and absorption graph of 3×10^{13} ions/cm² irradiated thin film

FDTD simulation was used to calculate the absorption in nanocomposite thin film for pristine and 3×10^{16} ions/cm² irradiated thin film. HR-TEM images were used for the simulation of absorption and electric field intensity distribution. Fig 5.6 unveil the electric field distribution at wavelength 530 nm and Fig 5.7 shows absorption obtained by FDTD simulation at 350 nm and 750 nm wavelengths. In the simulation, we have used refractive index and extinction coefficient for TiO₂ from reference¹⁴³ and Ag (CRC) from FDTD software¹⁴². The monitor was placed at a distance of 10 nm from the top surface of the thin film. The vertical colour bar represents the electric field intensity recorded in the monitor. The variation from the experimental results is observed that is because a small area of the film was used for simulation. Before irradiation, the interparticle separation is very less which, plays an essential role in inter plasmonic coupling effect¹⁴⁴. When plasmonic coupling becomes more effective, it affects the LSPR of nearby nanoparticles, which results in increased absorption for higher wavelength. This increment in absorption can be understood by using MAG (Maxwell-Garnet Theory) and Mie theory¹⁴⁵. This theory explains the plasmon

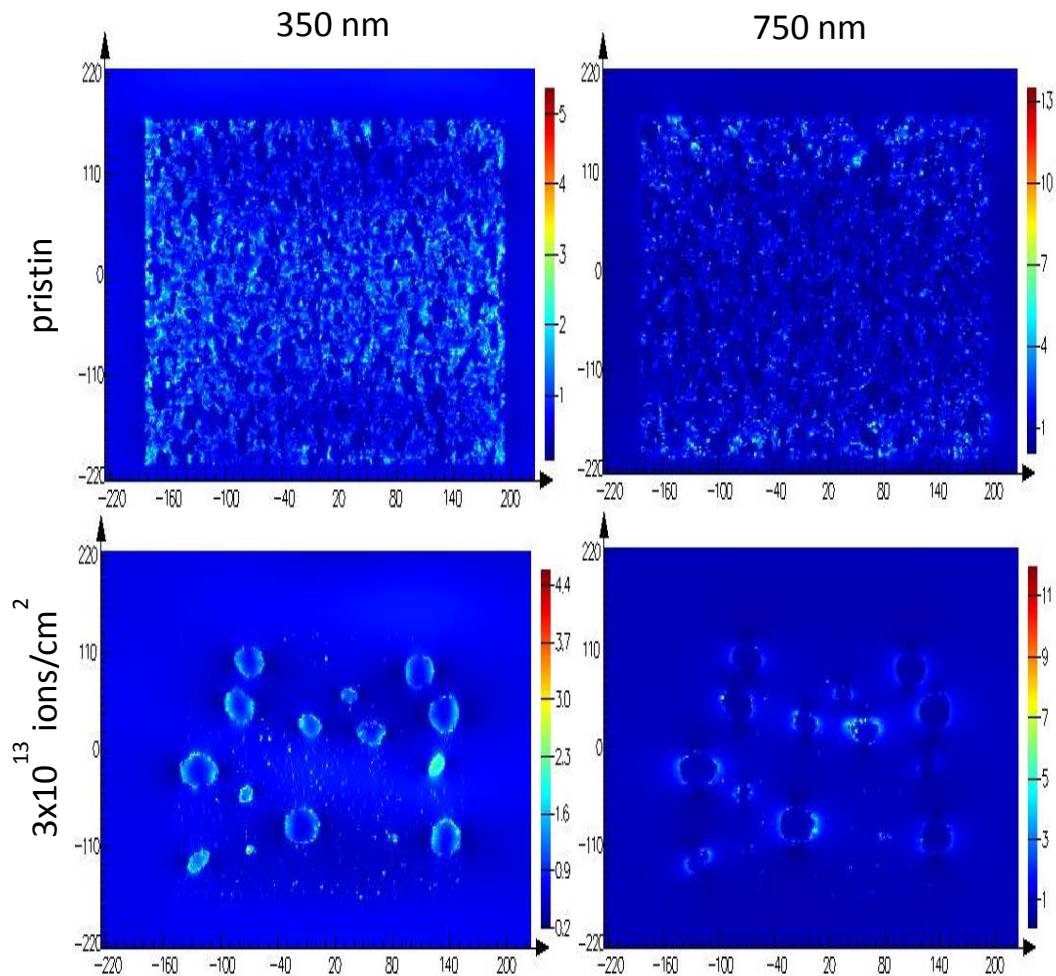


Fig 5.7 FDTD simulation of pristine and 3×10^{13} ions/cm² irradiated thin film at 350 nm and 750 nm

resonance in nanoparticles having less inter-particle separation. It considers the inter-particle plasmonic effect on other nanoparticles and explains surface plasmon for a densely packed nanoparticle. According to these theories when nanoparticle size is increased, it is resonant wavelength increases^{62,132}. The effects of interparticle plasmonic coupling also observed in the FDTD simulation, in fig 5.7 the absorbed power is low at 350 nm and 750 nm compared to power absorbed at 550 nm. Absorption at 350 nm includes the LSPR due to small nanoparticles, which are seen in fig 5.7 when the wavelength is increased the large particles effectively plays an important role in SPR absorption. It can be seen in fig 5.6 the electric field intensity increases after irradiation and shows less inter-particle plasmonic coupling effect compared to pristine thin film. The black circle shown in the figure are of size (a) 20 nm (b) 40 nm and (c) 35 nm. As we can see clearly at 530 nm, (c) shows good absorption whereas the particle

(a) and (b) contribute to absorption for lower and higher wavelength respectively. From fig 5.7 the difference in power was observed for 350 nm and 750 nm, but from fig 5.6 the absorption is almost same for both the wavelengths. The difference was due to the contribution of large particles in scattering. At higher wavelengths scattering dominates the absorption. This scattering is also beneficial for application of nanocomposite thin film as it hindered the transmittance of light.

SHI irradiation modifies the nanoparticle size and distribution and interparticle separation. After ion irradiation, growth in nanoparticles has been observed which is evident by TEM and UV-visible absorption results. The average particle size for the irradiated thin film with the highest fluence was calculated to be ~ 35 nm. For pristine thin film absorption increases at a higher wavelength. The increment in the SPR intensity was observed continuously with the fluence in the region 400 nm to 500 nm. A most intense peak of SPR has been observed after irradiation at fluence 3×10^{13} ions/cm² at 530 nm and its area was maximum compared to another irradiated thin film. That confirms an increment in particle size and number of particles. This result is in good agreement with the TEM results. As many clusters, atoms, and tiny nanoparticles combined to form new nanoparticles in the nanocomposite thin film, this leads to enhancement in the SPR absorption peak. The absorption in the region 350 nm to 400 nm is due to the smaller nanoparticles, which decreases while increasing the ion fluences. This decrement was also in support of the agglomeration of the smaller nanoparticles to form a bigger one due to the thermal energy deposited by SHI ions. Simultaneously the inter-particle separation has been increased by ion irradiation, which results in lowering the inter-particle coupling effect and broadening of SPR decreased. As there is the availability of small nanoparticles and clusters, the counts of absorption in the region 350 nm to 400 nm are due to the smaller nanoparticles which decreases while increasing the ion fluences. The absorption peak remains broad because of the formation of the irregular shape of Ag nanoparticles, which leads to non-homogenous polarization.

5.3 SHI irradiation of Ag (56 at.%) -TiO₂ nanocomposite thin film

5.3.1 Experimental detail

Ag-TiO₂ nanocomposite thin films have been deposited on quartz, silicon and glass substrates by RF co-sputtering. Before deposition, the substrates were sequentially cleaned with acetone, methanol and Tri-Chloro Ethylene (T.C.E.). TiO₂ powder of Alfa Aesar (~99.9%) has been used to prepare the target. The size of the target holder and the substrate holder was 2 and 5 inches respectively. This substrate holder rotates to get uniform composition and thickness all over the substrates. Before deposition, the vacuum was 1.2×10^{-6} torr. For sputtering, argon gas medium has been used at pressure 8×10^{-3} torr and flow of 11 sccm. The thin films were deposited at power 75 watts and room temperature. Ag-TiO₂ thin films were irradiated with 90 MeV Ni ion with fluences 1×10^{12} , 3×10^{12} , 6×10^{12} , 1×10^{13} ions/cm² at IUAC New Delhi. In the case of 90 MeV Ni ions, the electronic Se and nuclear energy Sn losses in the Ag-TiO₂ thin film is ~15.9 KeV/nm and ~0.104 KeV/nm respectively and the range of the Ni ion is 10.3 μ m which was calculated from SRIM 2008 program. The thickness of thin film and concentration of Ag were calculated by Rutherford Backscattering (RBS) spectrometry. The angle between the detector and 2 MeV He⁺ incident beam was 165°, this facility was used at IUAC, New Delhi, India. X-ray diffraction (XRD) measurements were carried out using Panalytical X-Pert Pro X-ray diffractometer to determine the crystallinity of thin films. For optical properties measurement, irradiated nanocomposite thin films have been characterized by UV-visible absorption spectroscopy using a dual beam Hitachi photo spectrometer. Morphological studies of pristine and irradiated thin films have been done using HR-TEM (Tecnai G2 20 FEI S-Twin 200kV). To simulate the absorption and electric field intensity, we have used Lumerical FDTD software (Lumerical).

5.3.2 Compositional, structural and morphological studies

For RBS analysis, Ag-TiO₂ thin films deposited on silicon have been used. The thickness and concentration of Ag metal were determined by RUMP¹⁰² program and found to be ~ 50 nm and 56 at.%. Simulation from RUMP program with depth profile is shown in Fig 5.8, which confirmed that in nanocomposite thin film only Ti, Ag and

O were present. From the fitting view and depth profile, it is clear that Ag is distributed evenly through/along the depth of the thin film.

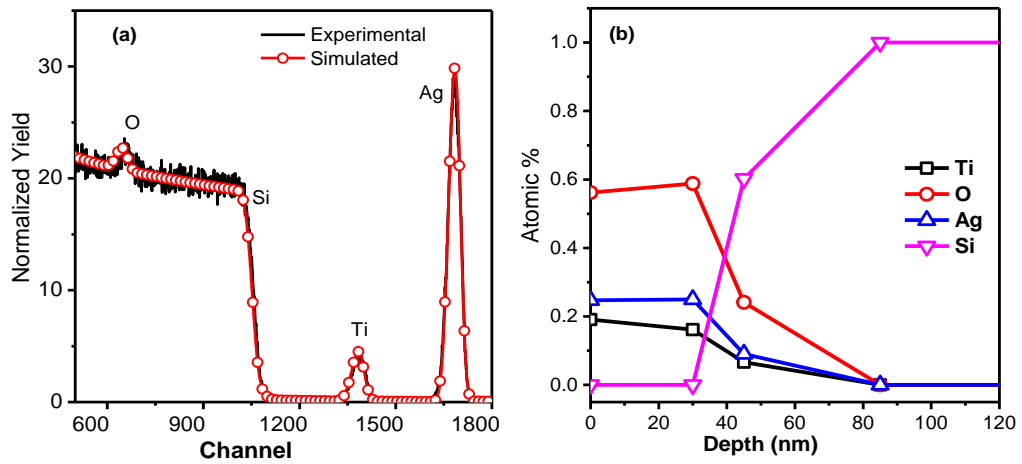


Fig 5.8 (a) RBS of Ag(56%)-TiO₂, simulation shown with line and experimental data with symbol. (b) Depth profile of Ag(56%)-TiO₂ nanocomposite thin film.

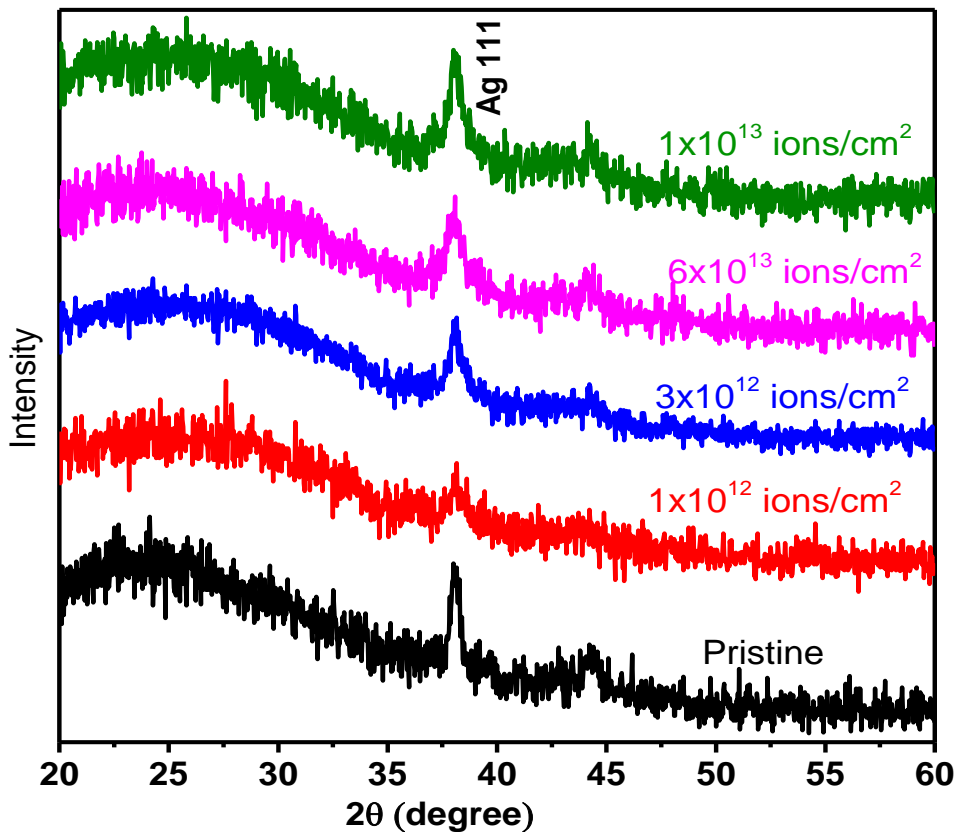


Fig 5.9 XRD of 90 MeV Ni ion irradiated thin film at different fluences

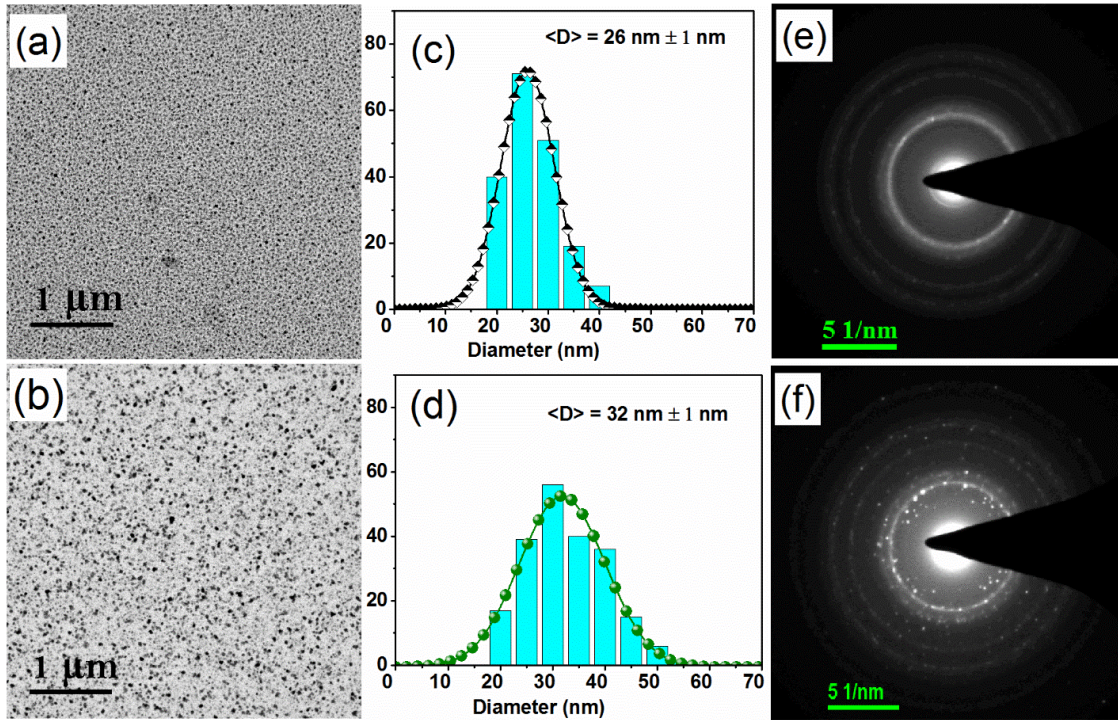


Fig 5.10 (a,b) Plan view, bright field TEM images with (e,f) SAED pattern and (c,d) histogram of particle size distribution

TEM images of pristine and SHI-irradiated Ag-TiO₂ nanocomposite thin films are shown in Fig 5.10. In the as-deposited thin film, no diffraction peak corresponds to TiO₂ was found which indicates amorphous nature of TiO₂. Which is also evident from SAED pattern in Fig 5.10(e). When these thin films were irradiated by 90 MeV Ni ion with fluences of 1×10^{12} , 3×10^{12} , 6×10^{12} , 1×10^{13} ions/cm², no change was observed in the phase of TiO₂; it remains in amorphous form. However, the crystallinity of silver was affected by ion irradiation. After ion irradiation, the crystallinity of silver was increased which is seen in the SAED pattern Fig. 5.10(f). The XRD pattern of pristine and SHI-irradiated Ag-TiO₂ nanocomposite thin films is represented in fig 5.10(a). The peak position of silver was observed at 38.1° and 44.3° which is in agreement with JCPDS ref no. 87-0720. For the fluence 1×10^{12} ions/cm², silver got amorphized and with increasing fluence from 3×10^{12} to 1×10^{13} ions/cm², the crystallinity of silver increases.

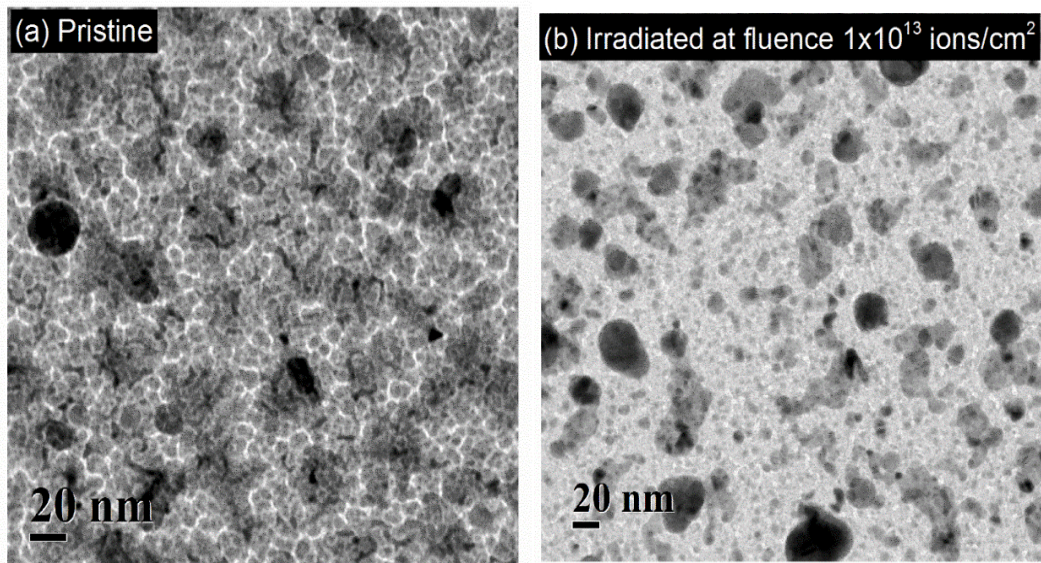


Fig 5.11 Bright field images showing the effect of ion irradiation on inter-particle separation

The topographical view of both as-deposited and ion irradiated samples is shown in Fig 5.10(a),(b). Fig 5.10(c),(d) shows the particle size distribution. The average silver nanoparticles size for as-deposited and ion irradiated was calculated ~ 26 nm and ~ 32 nm respectively. To plot a histogram of particle size, approx. 200 nanoparticles were considered. It is evident from particle size distribution that after ion irradiation, the average particle size was increased by ~ 6 nm. From Fig 5.11 it has been analyzed that the inter-particle separation between nanoparticles for the as-deposited sample is very less than their average particle size.

5.3.3 Absorption spectroscopy and FDTD simulation

Nanocomposite thin films deposited on glass were used to observe the effect on optical properties and their UV-visible absorption spectra are given in Fig 4.12. From Fig 4.12, it is clear that no SPR has been observed in the visible range for the as-deposited thin film. The optical plasmonic behaviour of metal nanoparticles embedded in a matrix depends on the morphology, inter-particle separation, nanoparticles size distribution and dielectric constant of the matrix.

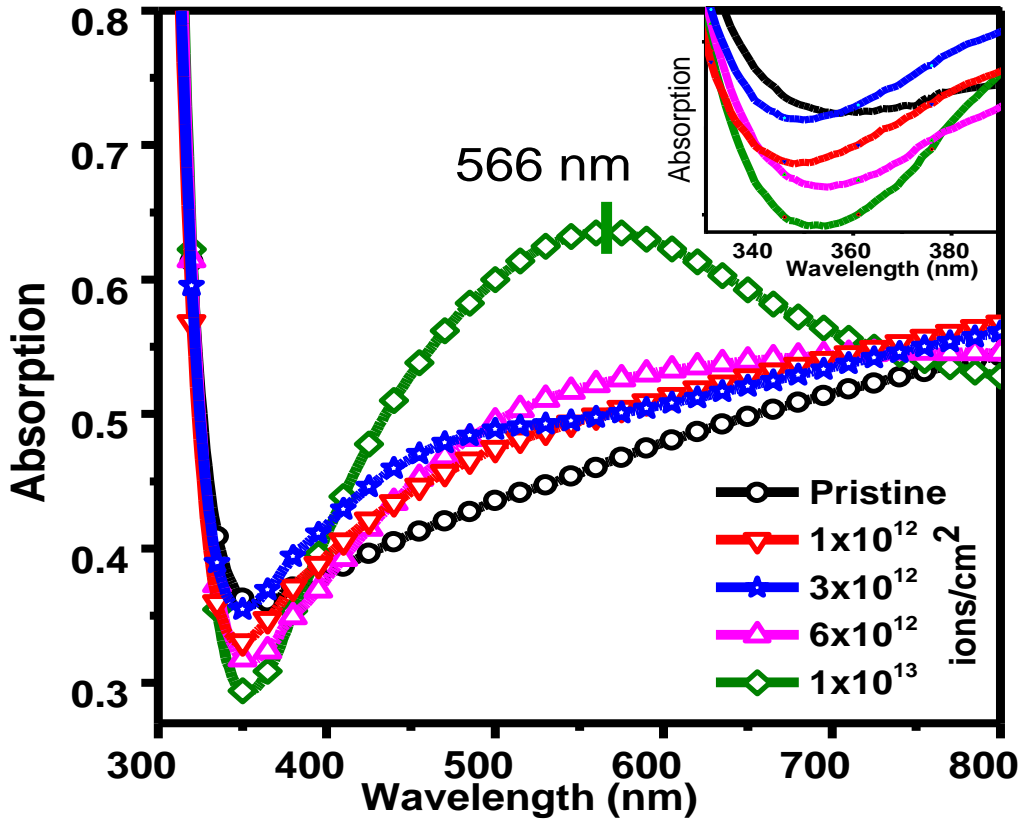


Fig 5.12 Optical absorption spectra of 90 MeV Ni ion irradiation of nanocomposite thin film

In the present case, the metal nanoparticles are of silver, and the dielectric matrix is TiO₂. Here for Ag-TiO₂ (Ag at. 56%) as-deposited thin film (pristine film), the interparticle separation was minuscule compared to the nanoparticle size, which is seen in Fig 5.11(a). The average nanoparticle size was calculated to be ~ 26 nm. This minuscule inter-particle separation results in lying the SPR in the infrared region and broadening of SPR. When these thin films were irradiated by 90 MeV Ni ion, the absorption increases in the visible region. For the fluence 1×10^{12} and 3×10^{12} ions/cm², there is an increment in absorbance in the region 400 – 600 nm. At fluence 6×10^{12} ions/cm², the absorbance shifted towards the higher wavelength. However, at the fluence 1×10^{13} ions/cm², broad SPR is observed at position 566 nm.

To study the plasmonic modification in Ag-TiO₂ nanocomposite thin films (the pristine and 1×10^{13} ions/cm² irradiated thin film) HR-TEM images (Fig 5.11) were used for the simulation of absorption and electric field intensity distribution by FDTD method. Fig 5.13(a) and (b) unveil the electric field distribution at wavelength 550 nm and Fig 5.13(c) shows absorption obtained by FDTD simulation. In the simulation, we have

used refractive index and extinction coefficient for TiO₂ from reference¹⁴³ and Ag (CRC) from FDTD software¹⁴². The monitor was placed at a distance of 10 nm from the top surface of the thin film. The vertical colour bar represents the electric field intensity recorded in the monitor. The variation from the experimental results is because a small area of the film was used for simulation. Before irradiation the interparticle separation is very low, so, the plasmonic coupling becomes more active and it affects the LSPR of nearby nanoparticles, which results in increased absorption at a higher wavelength. This can be understood by using MAG (Maxwell-Garnet Theory) and Mie theory¹⁴⁵.

According to these theories, when nanoparticle size is increased, the higher order modes become more important and the nanoparticle polarizes non-homogeneously. Therefore, due to these higher modes, there is shifting in plasmon position with increment in particle size and the plasmon bandwidth¹⁴⁶. Though, Mie theory is valid only for low concentration of nanoparticles in the solid matrix. In Mie theory, each nanoparticle is assumed to be separated by enough distance, and no SPR effect on other nanoparticles is considered. In the case of pristine thin film, Mie theory cannot be applied as only a minuscule separation exists between nanoparticles. This problem can be solved by MAG theory. This theory explains the plasmon resonance in nanoparticles having less inter-particle separation. It considers the inter-particle plasmonic effect on other nanoparticles and explains surface plasmon for densely packed nanoparticles in a host matrix. A combined model of this theory is given graphically in Fig 5.15. According to these theories when nanoparticle size is increased, its SPR wavelength increases. If we consider two nanoparticles at low separation as given in Fig 5.15, then as the separation decreases the interparticle plasmonic coupling becomes more effective and its SPR wavelength increases. Those two particles play a role in SPR and show complex absorption. These effects also observed in the FDTD simulation, in fig 5.14(a) the absorbed power is low at 350 nm and 750 nm compared to power absorbed at 550 nm. Absorption at 350 nm includes the LSPR due to small nanoparticles, which are seen in fig 5.15 when the wavelength is increased the large particles effectively shows absorption by LSPR. From fig 5.14 the difference in power was observed for 350 nm and 750 nm, but from fig 5.13 the absorption is almost same for both the wavelengths. The difference was due to the contribution of large particles in scattering. At higher wavelengths scattering dominates the absorption.

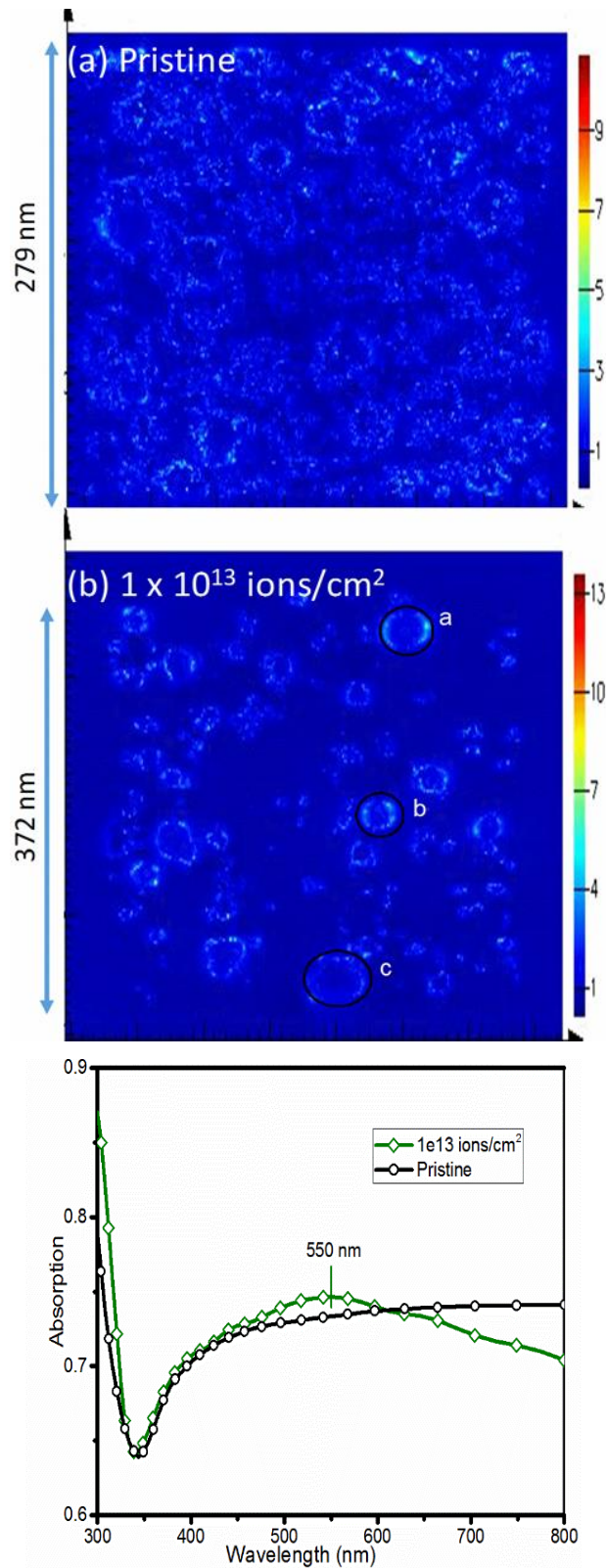


Fig 5.13 Distribution of electric field intensity around silver nanoparticles (a) simulation for pristine thin film (b) simulation of irradiated thin film at fluence 1×10^{13} ions/cm² at 550 nm (c) absorption spectra from the simulation.

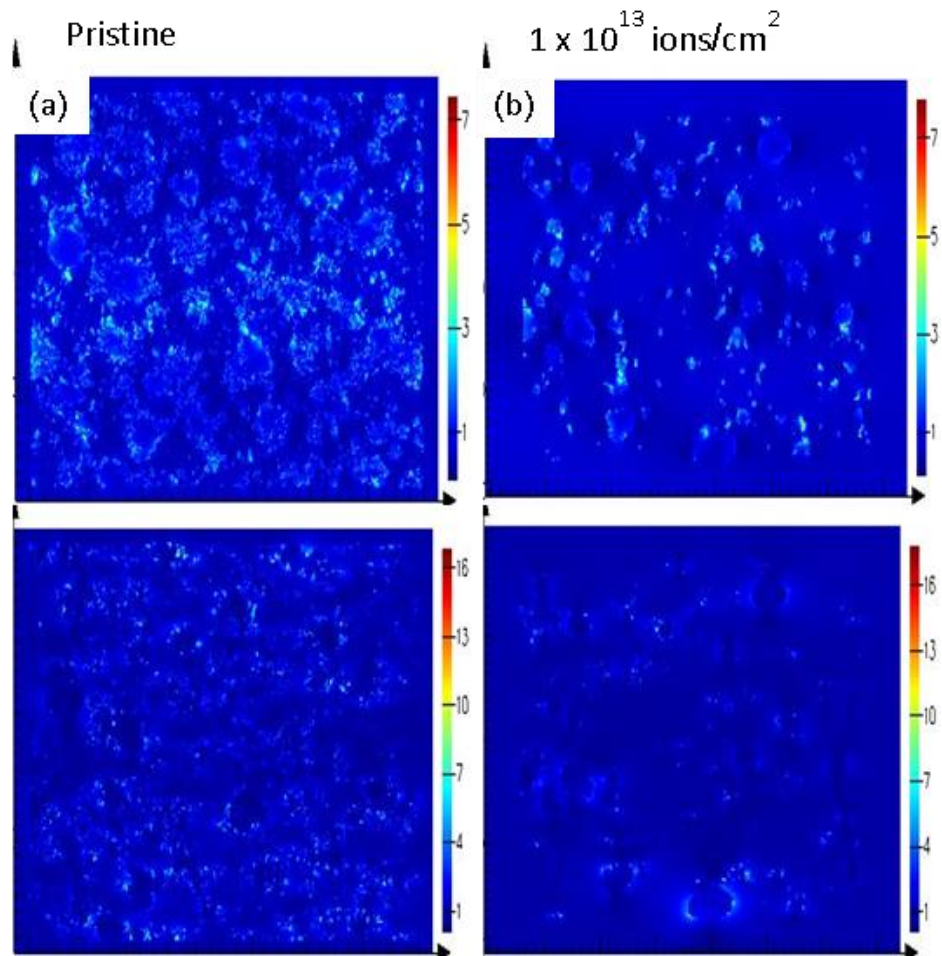


Fig 5.14 Distribution of electric field intensity (a) simulation for the pristine thin film at 350 nm and 750 nm (b) simulation for the irradiated thin film at fluence 1×10^{13} ions/cm² at 350 nm and 750 nm

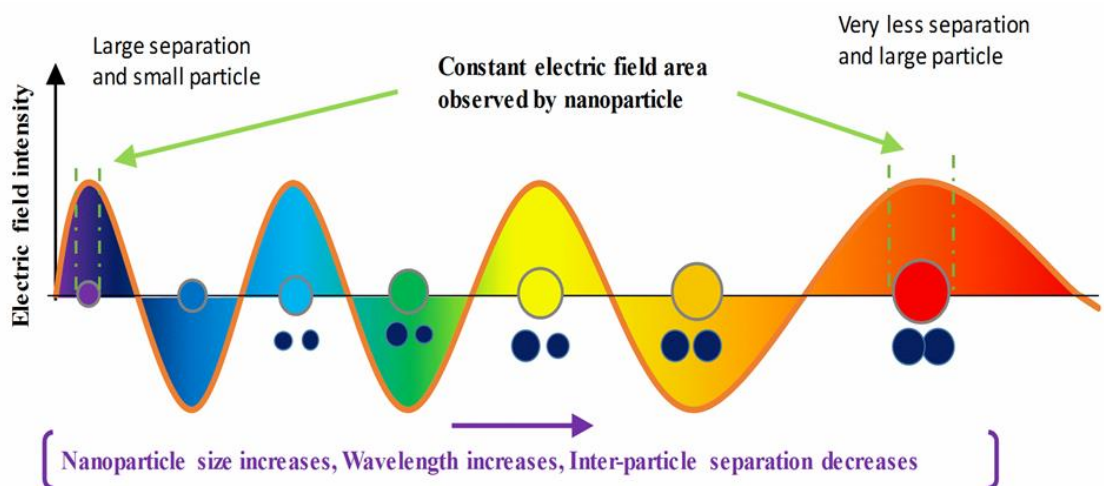


Fig 5.15 The schematic diagram shows colour/absorption depending on nanoparticle size and inter-particle separation

It can be seen in fig 5.13(a),(b) that the electric field intensity increases after irradiation and shows less inter-particle plasmonic coupling effect compared to pristine thin film. The black circle shown in the figure are of size (a) 35 nm (b) 26 nm and (c) 50 nm. As we can see clearly at 550 nm, (a) and (b) shows good absorption whereas the particle (c) which is larger than (a) and (b) partially absorbed power at 550 nm.

After SHI irradiation the properties and distribution of nanoparticles are modified. Earlier studies revealed in the reduction or growth of metal nanoparticles and variation in their inter-particle separation in nanocomposite thin film⁹³. After ion irradiation, growth in nanoparticles has been observed which is evident by TEM and UV-visible absorption results. The average particle size for the irradiated thin film with the highest fluence was calculated to be ~ 32 nm shown in fig 5.10(d). From UV-visible absorption graph fig 5.12(a), for pristine thin film absorption increases for higher wavelength. At low fluence irradiation 1×10^{12} and 3×10^{12} ions/cm², there is an increment in the SPR intensity in the region 400 nm to 500 nm. At fluence 6×10^{12} ions/cm² the absorption in region 400-500 nm shifted towards higher wavelength (500 nm – 600 nm) region. A most intense peak of SPR has been observed after irradiation at fluence 1×10^{13} ions/cm² at 566 nm and its area was increased compared to other irradiated thin film, which reveals an increase in particle size and a number of particles. This result is in good agreement with the TEM results. As many clusters, atoms, and very small nanoparticles combined to form new nanoparticles in the nanocomposite thin film, this leads to enhancement in the SPR absorption peak. The absorption in the region 320 nm to 400 nm is due to the smaller nanoparticles, which decreases while increasing the ion fluences. This decrement was also in support of the agglomeration of the smaller nanoparticles³⁹ to form a bigger one due to the thermal energy deposited by SHI ions. Simultaneously the inter-particle separation has been increased by ion irradiation, which results in lowering the inter-particle coupling effect and broadening of SPR decreased. As there is the availability of small nanoparticles and clusters, the counts of absorption in the region 320 nm to 400 nm are due to the smaller nanoparticles which decreases while increasing the ion fluences. The absorption peak remains broad because of the formation of the irregular shape of Ag nanoparticles, which leads to non-homogenous polarization.

5.4 Conclusions

Ion irradiation of heavily included silver in TiO₂ matrix shows significant changes in the morphological and plasmonic properties of nanocomposite thin film. The average size of nanoparticles was increased in both cases from 30 nm to 35 nm for Ag(45%)-TiO₂ and 26 nm to 32 nm for Ag(56%)-TiO₂. A minor red shift was observed for Ag(56%)-TiO₂ with increasing the fluence. FDTD simulation has been done for both pristine and irradiated thin film, which explains and support the experimental. The growth of Ag nanoparticles and occurrence of redshift is discussed in detail and attributed to agglomeration due to massive electronic energy transferred by swift heavy ion irradiation. This modification by SHI irradiation by enhancing the SPR in the visible region for both the thin films will be advantageous for photocatalytic activities and biomaterials.

Chapter Six

Modification in Ag-TiO₂ thin film by thermal annealing

6.1 Introduction

The optical properties of nanocomposite thin film show dependency on the nanoparticles shape, size, distribution and host matrix dielectric properties. By altering this parameter, one can achieve desired properties from nanocomposite thin film. The alteration of these properties can be done by varying the parameter during deposition and providing any treatment to nanocomposite thin film. Thermal annealing treatment is one of them. In this chapter modification of optical properties by thermal annealing is discussed.

6.2 Thermal annealing of nanocomposite thin film

6.2.1 Experimental detail

The nanocomposite thin film of Ag-TiO₂ with silver concentration (24%, 33%, 45%, 56%) was annealed using the Lenton tube furnace. The nanocomposite thin film was sequentially annealed at 200 °C, 400 °C, 600 °C for one hr in the ambient environment of Ar gas. The setup diagram is shown in fig 3.6. After annealing, the thin films were naturally cooled, the argon gas flows continuously till the sample archive room temperature. Alumina boat is used to keep the samples in a tube furnace. These samples were characterized by UV-visible absorption spectroscopy, XRD and XPS for each annealing temperature.

6.2.2 Thermal annealing of Ag(24%)-TiO₂ thin film

Fig 6.1 shows the XRD for Ag(24%)-TiO₂ annealed at 200 °C, 400 °C, 600 °C. The XRD was taken at a glancing angle 1.5°. In the as-deposited sample, a matrix of TiO₂ was in the phase Anatase (101). When this was annealed at 200 °C, anatase phase diminishes and a small peak of rutile (101) emerges. Annealing at 400 °C increases the crystallinity matrix in rutile (101) phase. Which continue its growth for the sample

annealed at 600 °C. While increasing the rutile and anatase phase intensity redevelop crystallinity. At 600 °C, a mixed phase of TiO₂ was obtained. A slightly increment in the intensity of Ag(111) was observed, but after annealing at 600 °C, the silver phase vanishes completely. Mixed-phase phase occurrence can be explained on the stability of TiO₂ phase with temperature. Anatase phase was stable at low temperature whereas rutile was stable at high temperature. For the mid-temperature range, we will have mixed phase and anatase phase transforms entirely to rutile at high temperature (above 700 °C). UV visible absorption spectroscopy is shown in fig 6.2. In this as-deposited thin film shows broad absorption for complete visible spectrum but no SPR was observed. Annealing the thin film at 200 and 400 °C, increases the absorption in the visible region. Low intensity and broad LSPR was observed at 650 nm.

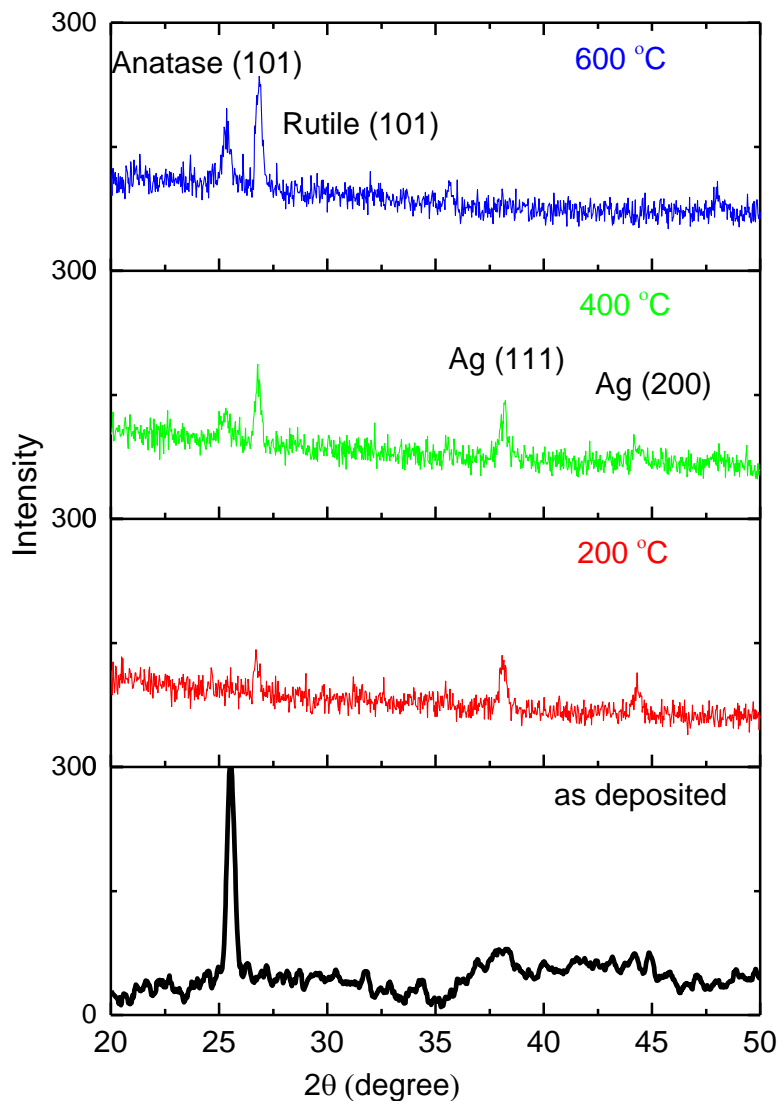


Fig 6.1 XRD of Ag(24%)-TiO₂ nanocomposite thin film as-deposited and annealed at 200 °C, 400 °C, 600 °C.

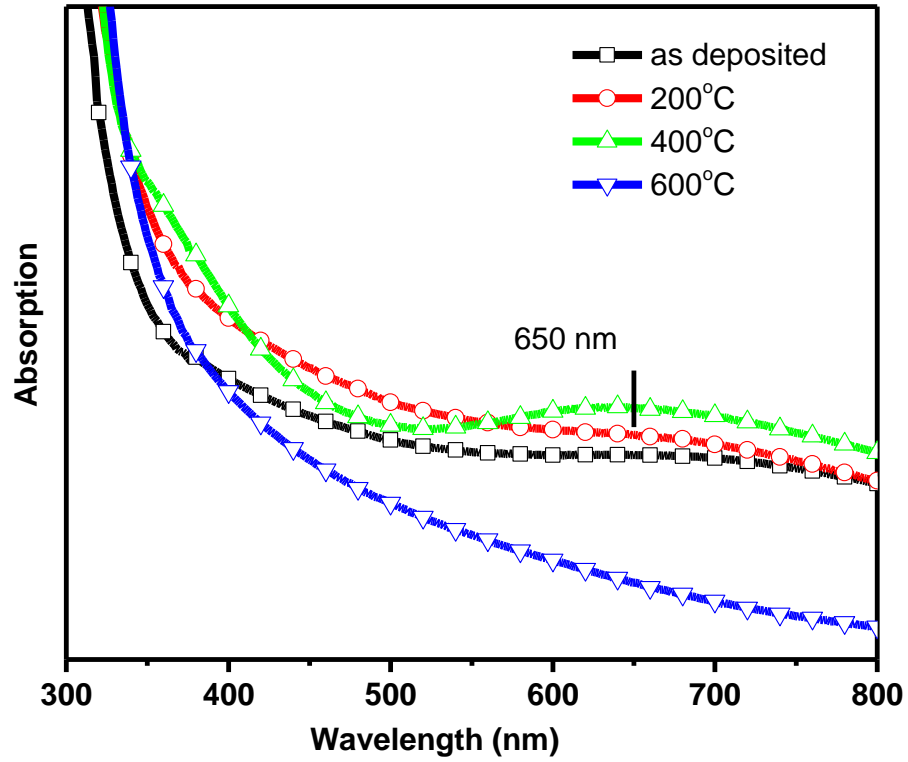


Fig 6.2 UV-visible absorption spectroscopy of Ag(24%)-TiO₂ nanocomposite thin film as-deposited and annealed at 200 °C, 400 °C, 600 °C.

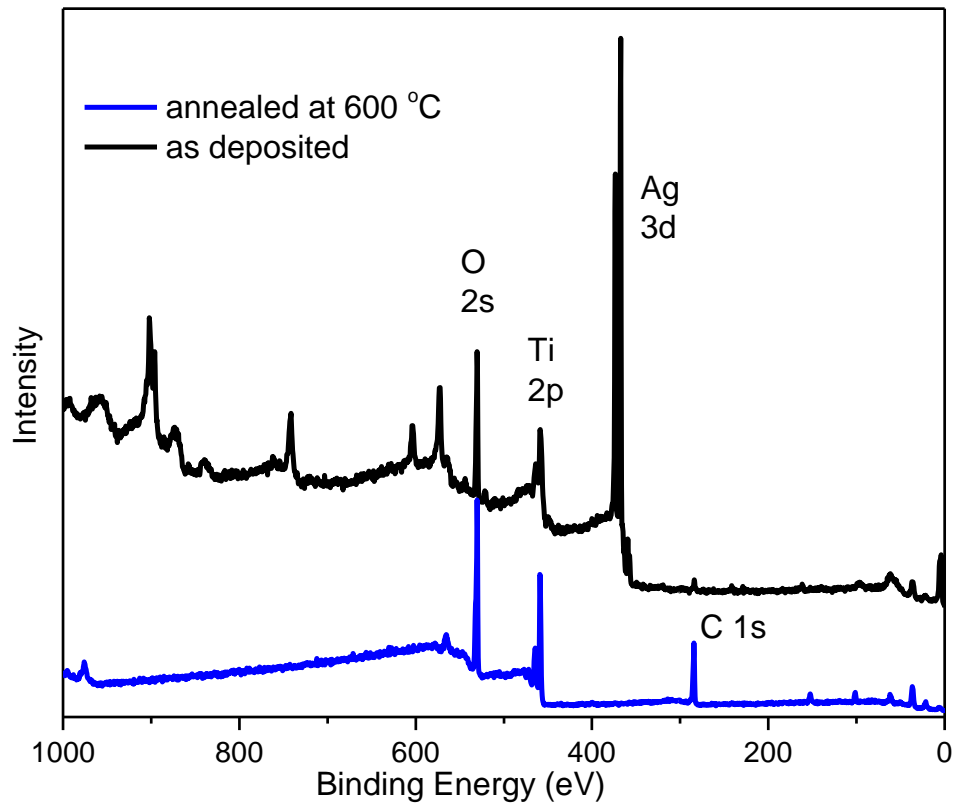


Fig 6.3 XPS of Ag(24%)-TiO₂ nanocomposite thin film as-deposited and annealed at 600 °C.

The occurrence of this SPR can be explained by agglomeration of silver nanoparticles to form bigger and improvement in the crystallinity of host matrix. The effect of both increased nanoparticle size and crystallinity cause the appearance of SPR at that position. Annealing at 600 °C decreased the absorption, this decrement in the absorption of thin film was assumed to be due to the sublimation of silver nanoparticle, as the reported sublimation temperature of silver nanoparticle is around 450 °C. This sublimation of silver nanoparticle is supported by XRD and XPS (fig 6.3). From XRD the silver phase vanishes completely and no signature of silver or silver oxide was detected. In XPS analysis, the intensity of Ag 3d peak decreased drastically, which is the clear signature of the absence of silver in the TiO₂ matrix.

6.2.3 Thermal annealing of Ag(33%)-TiO₂ thin film

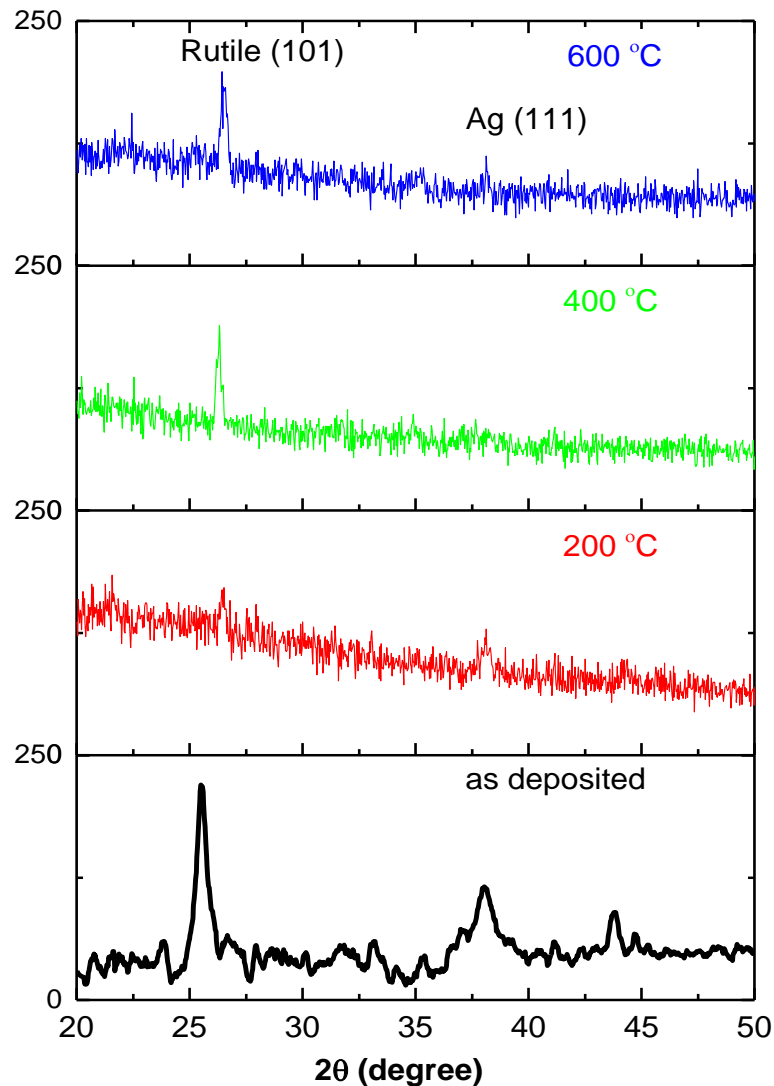


Fig 6.4 XRD of Ag(33%)-TiO₂ nanocomposite thin film as-deposited and annealed at 200 °C, 400 °C, 600 °C.

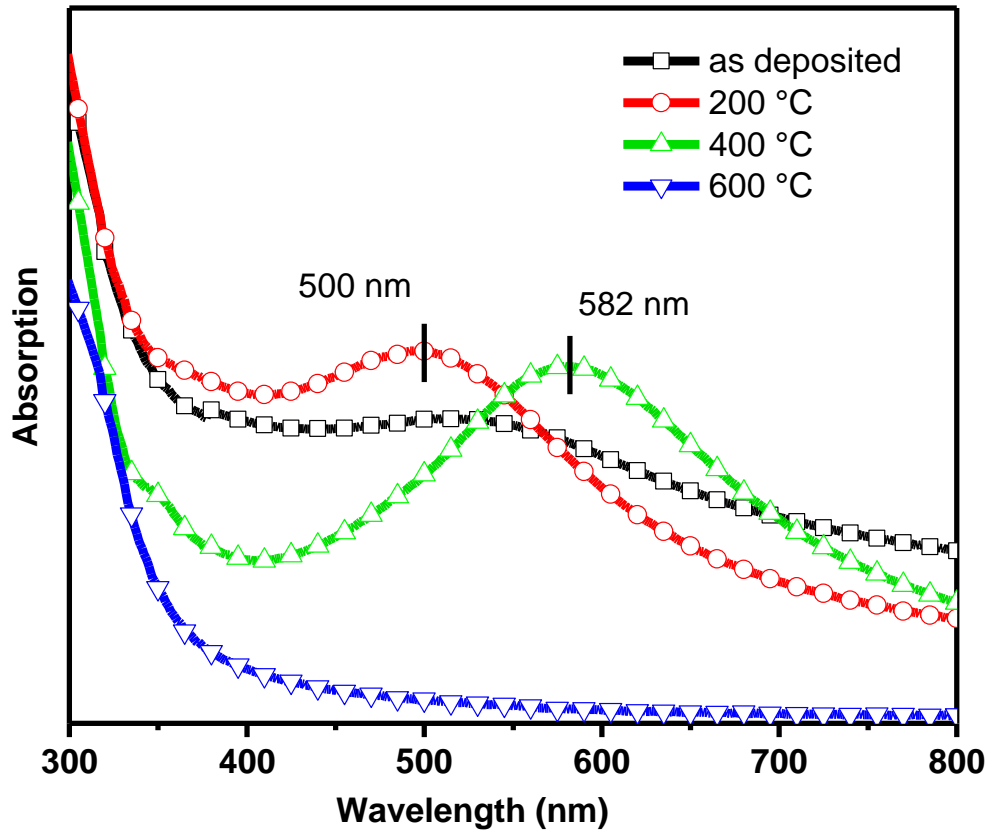


Fig 6.5 UV-visible absorption spectroscopy of Ag(33%)-TiO₂ nanocomposite thin film as-deposited and annealed at 200 °C, 400 °C, 600 °C.

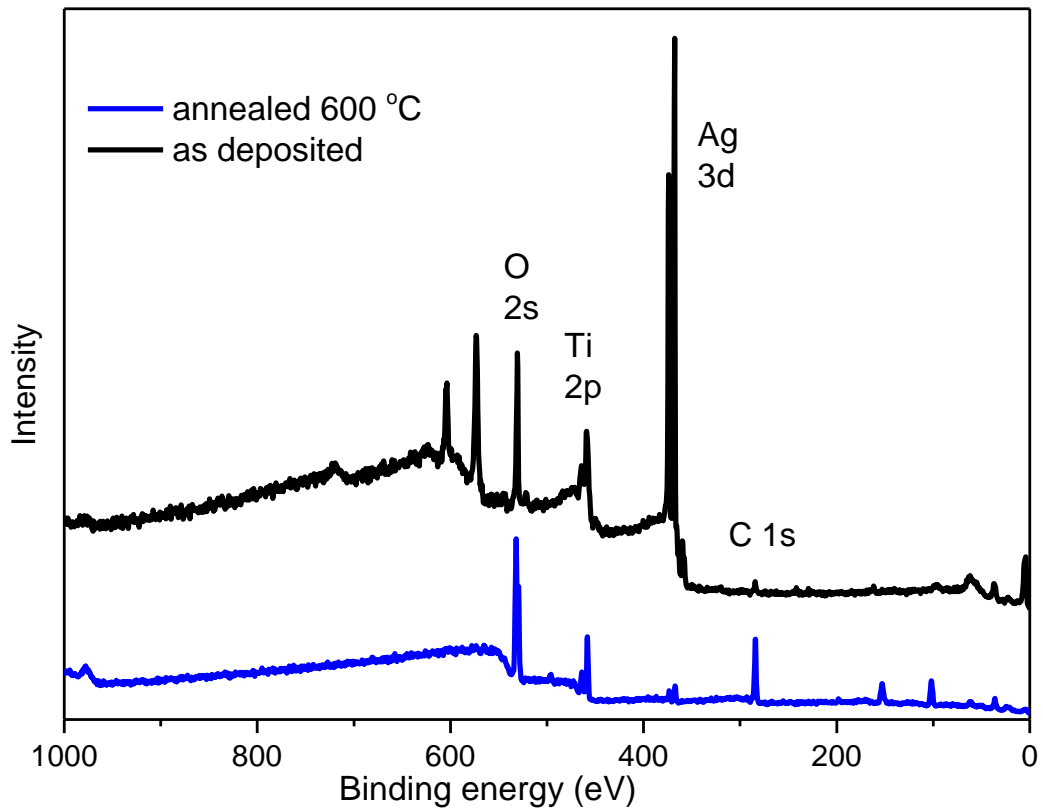


Fig 6.6 XPS of Ag(33%)-TiO₂ nanocomposite thin film as-deposited and annealed at 600 °C.

Fig 6.4 shows the XRD for Ag(33%)-TiO₂ annealed thin film with as-deposited thin film. Annealing at temperature 200 °C amorphized the matrix and the anatase phase vanishes completely, a small peak of rutile TiO₂ was observed. The intensity of this rutile peak increases with increasing the annealing temperature. As the rutile was stable at high temperature but here growth of rutile observed at 200 °C. Crystallization in the TiO₂ matrix is affected by the filler material silver. Ag hindered the growth of anatase phase. Ag is also affecting the rutile phase. Annealing at temperature 600 °C makes Ag peak disappear entirely. This disappearance of Ag peak is explained on behalf of the sublimation of silver. As in fig 6.5, where the absorption of a thin film highly decreased, is the signature for the absence of silver nanoparticle in the thin film. It was also supported by XPS analysis given in fig 6.6, which shows that after annealing at 600 °C Ag3d peak vanishes completely. No silver oxide peak was observed in XRD. These results reveal the sublimation of silver nanoparticle. For the UV-visible absorption spectroscopy shown in fig 6.5, when the annealing treatment was given at 200 °C, an LSPR at position 500 nm was observed. The occurrence of LSPR is due to the combined effect of silver nanoparticle agglomeration and change in the matrix phase of TiO₂. The absorption due to host matrix was shifted to a lower wavelength which shows the improvement in crystallinity of rutile phase. A broad absorbance in the as-deposited thin film is due to the interparticle coupling effect. Agglomeration of the nanoparticle by thermal annealing increase the interparticle separation, which results in a decrement in the interparticle plasmonic coupling effect. Annealing at temperature 400 °C the LSPR shows redshift by value 82 nm. This redshift was due to the combined effect of silver nanoparticle agglomeration and increased the dielectric constant of host matrix^{147,148}. Dielectric constant¹⁴⁹ of rutile is greater than dielectric constant for anatase. In the region, 350 nm to 450 nm decrement in absorption observed which was due to the reduced quantity of small silver nanoparticle as they agglomerate to form a bigger particle. The LSPR at 400 °C is broad and cover almost the whole visible region.

6.2.4 Thermal annealing of Ag(45%)-TiO₂ thin film

XRD analysis for as-deposited and annealed Ag(45%)-TiO₂ thin film is shown in fig 6.7. Such a high concentration of silver affects the crystallinity of the host matrix and promote amorphisation¹⁵⁰, as the deposited thin film shows no diffraction peak for TiO₂.

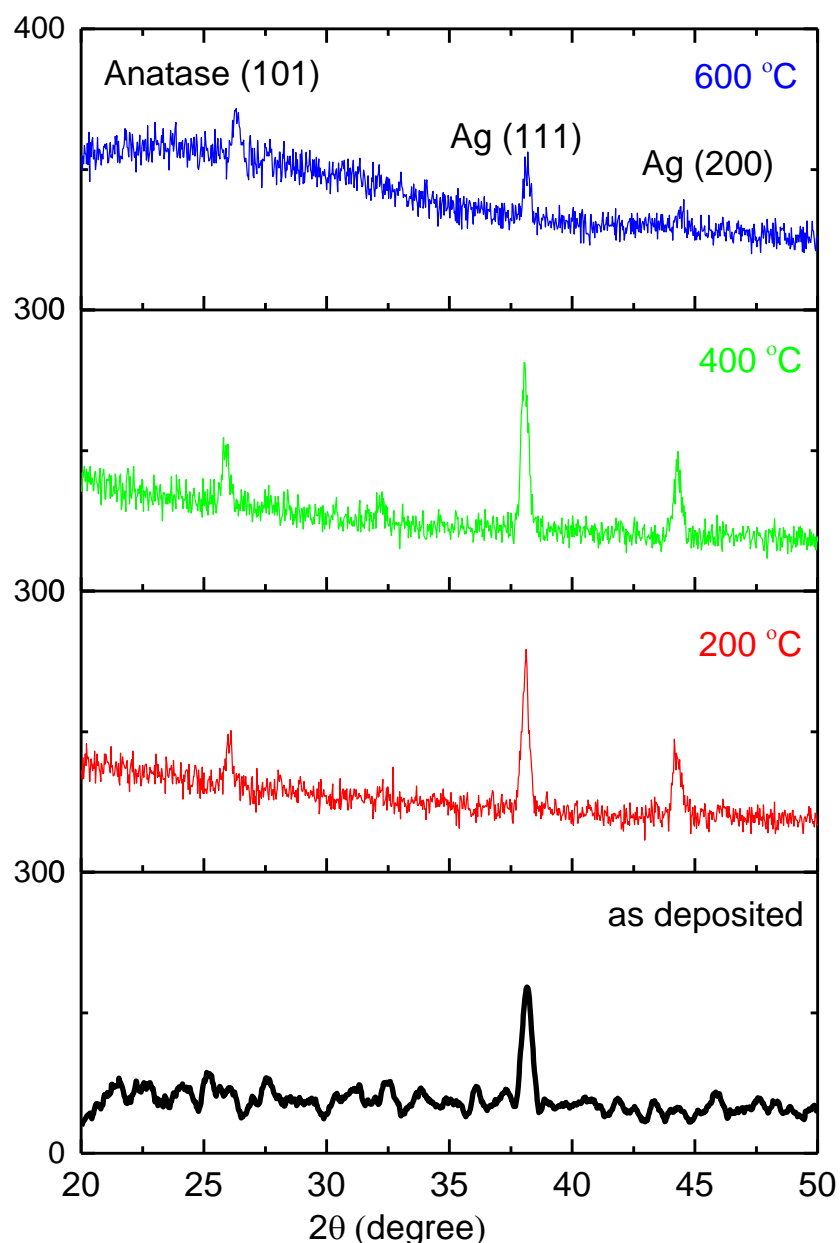


Fig 6.7 XRD of Ag(45%)-TiO₂ nanocomposite thin film of as-deposited and annealed at 200 °C, 400 °C, 600 °C.

Annealing at 200 °C crystallization of silver increases and a small diffraction peak related to the anatase phase was observed. Increasing the annealing temperature to 400 °C marginally changes were observed, but after annealing at 600 °C, intensity of Ag(111) decreases and anatase phase remain same with marginally changes. From the UV-visible absorption spectroscopy shown in fig 6.8 confirm the existence of two LSPR for the annealing temperature 200 °C, which was rare to obtain in the case of

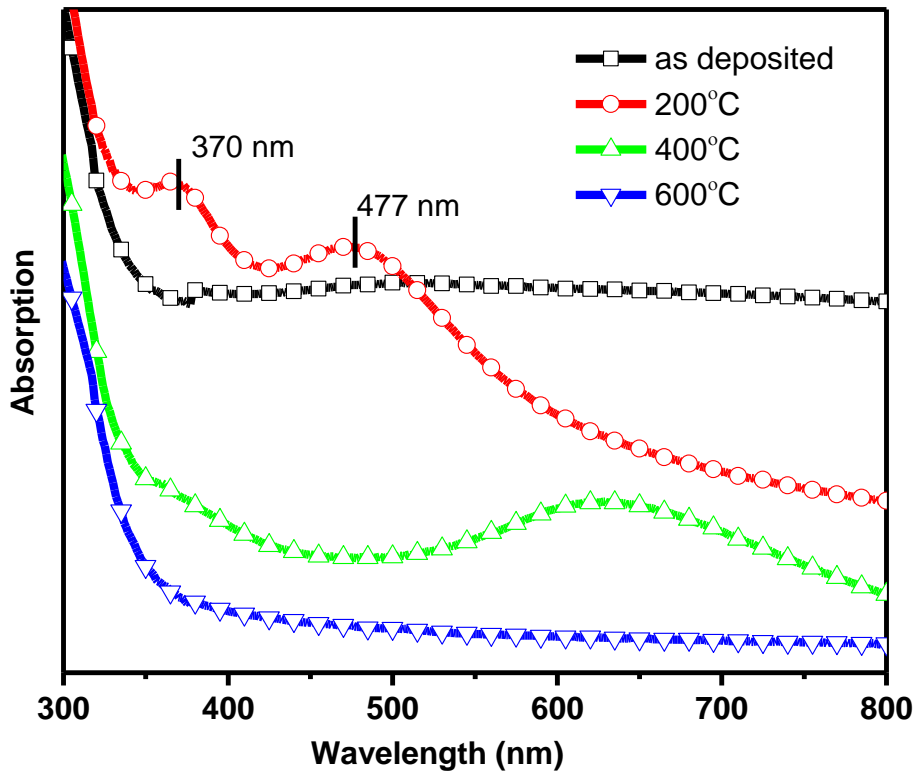


Fig 6.8 UV-visible absorption spectroscopy of Ag(45%)-TiO₂ nanocomposite thin film as-deposited and annealed at 200 °C, 400 °C, 600 °C.

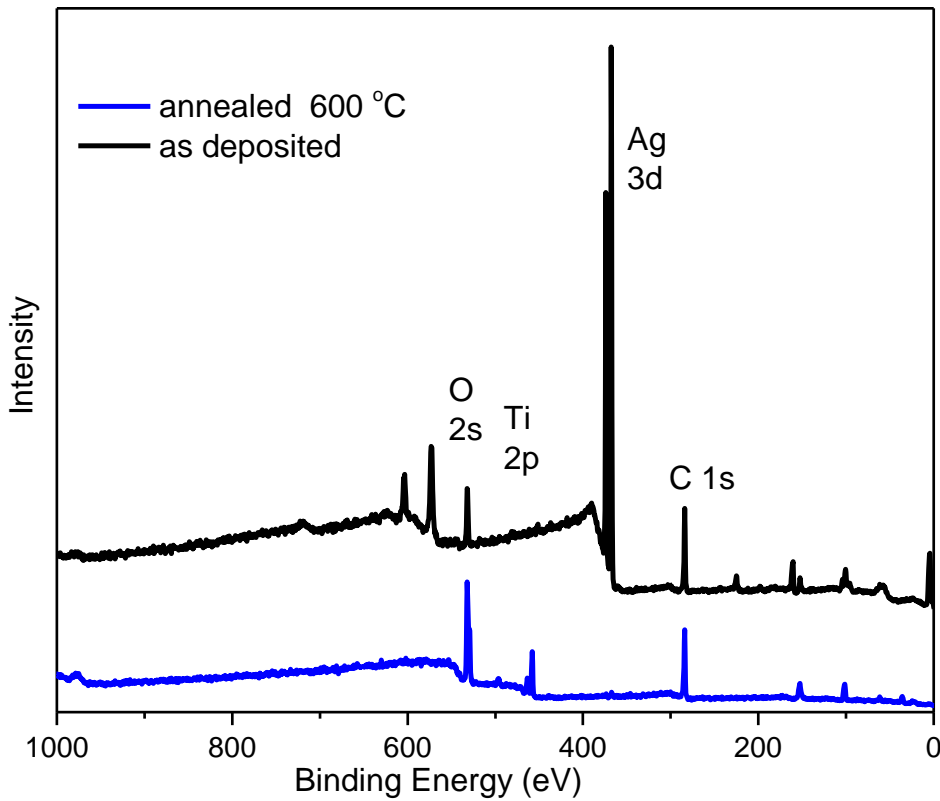


Fig 6.9 XPS of Ag(45%)-TiO₂ nanocomposite thin film as-deposited and annealed at 600 °C.

thermally annealed thin films. This existence of two LSPR at 370 nm and 477 nm can be explained by formation of nanoparticle of different size or irregular shape of Ag nanoparticle which form after agglomeration. Increasing the annealing temperature to 400 °C shows a high decrement in absorption and shifting of LSPR to the position 630 nm. This decrement in absorption was due to the formation of a large nanoparticle by agglomeration of a small one. Thus some small nanoparticle decreases and interparticle separation increases which results in reducing the interparticle plasmonic coupling effect. This reduced plasmonic coupling effect results decrement in absorption 350 nm to 600 nm. The SPR observed at 525 nm for as-deposited thin film was disappear after annealing. Its intensity was very low and it was very broad due to the interparticle plasmonic coupling effect. Annealing at 600 °C shows the sublimation of Ag nanoparticle, which was supported by the XPS analysis shown in fig 6.9. Increasing the annealing temperature shift the absorption edge of TiO₂ to lower wavelength. This happens due to increment in crystallinity, but in XRD only marginal change was observed.

6.2.5 Thermal annealing of Ag(56%)-TiO₂ thin film

For Ag(56%)-TiO₂ thin film, XRD is shown in fig 6.10. Initially, for as-deposited thin film, the only Ag(111) phase was obtained. There is diffraction peak corresponding to any phase related to TiO₂. As the annealing treatment is given at temperature, 200 °C mixed phases of anatase and brookite appear. After annealing treatment, crystallization of Ag was also increased. Brookite(200) phase intensity was increased after annealing at 400 °C, but there was no change in anatase(101). Annealing at 600 °C shows the conversion of anatase phase to rutile phase, but for silver, no diffraction peaks were observed. Like all previous results sublimation of silver can be assumed. This sublimation was supported by XPS (fig 6.12) analysis in which the intensity of Ag 3d peak decreases drastically. UV-visible absorption graph is shown in fig 6.11. For the as-deposited thin film, there is no LSPR, the absorption increases continuously with increment in wavelength. This was explained by the occurrence of strong interparticle coupling effect of silver nanoparticle in the nanocomposite thin film. The interparticle separation was less than the size of the nanoparticle (discussed in chapter 4) makes plasmonic coupling effect more effective. After annealing treatment at 200 °C only marginally change observed in absorption. Annealing at 400 °C shows a very broad and

low-intensity LSPR in the region 550 nm to 750 nm. Sublimation of silver was observed after annealing at 600 °C supported with XPS result (fig 6.12). Thermal annealing provides enough energy to promote agglomeration, but here the concentration of silver is very high it was assumed that after agglomeration the interparticle separation was not increased too much to promote a reduction in the plasmonic coupling. That is why we have high intensity of absorption for the whole visible region.

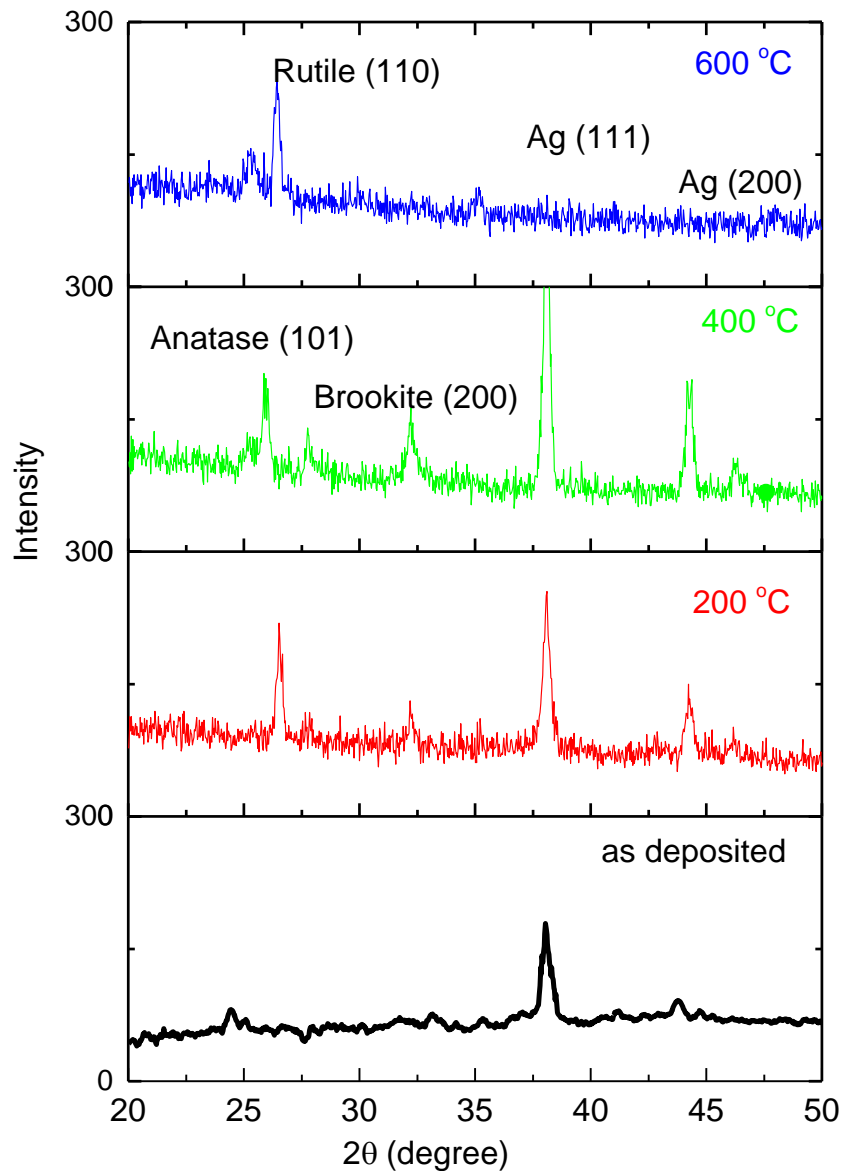


Fig 6.10 XRD of Ag(56%)-TiO₂ nanocomposite thin film as-deposited and annealed at 200 °C, 400 °C, 600 °C.

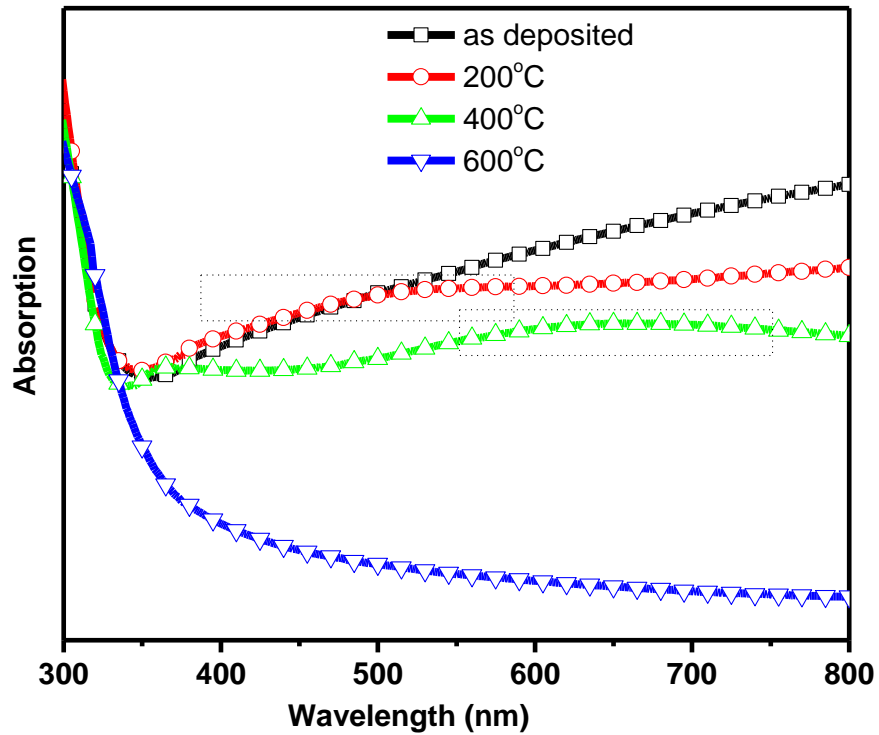


Fig 6.11 UV-visible absorption spectroscopy of Ag (56%)-TiO₂ nanocomposite thin film as-deposited and annealed at 200 °C, 400 °C, 600 °C.

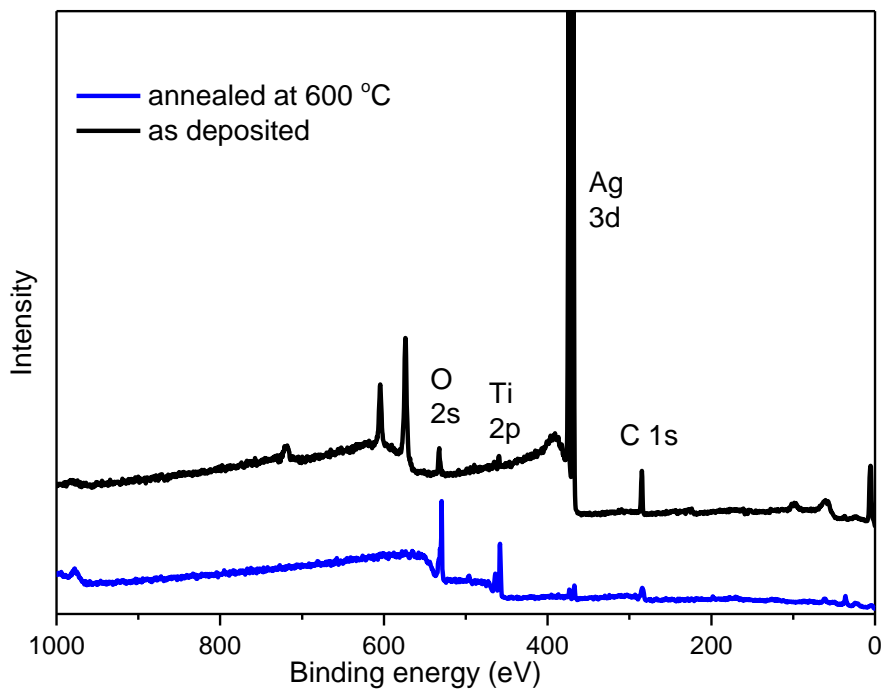


Fig 6.12 XRD of Ag(56%)-TiO₂ nanocomposite thin film of as-deposited and annealed at 200 °C, 400 °C, 600 °C.

A comparison of LSPR position with temperature effect is shown in table 6 given below for all concentration.

Table 6

Temperature dependence of LSPR position for all concentration.

Temp.	Ag (24%) - TiO ₂	Ag (33%)- TiO ₂	Ag (45%)- TiO ₂	Ag (56%)- TiO ₂
Pristine	-----	-----	-----	-----
200 °C	-----	500 nm	370, 477 nm	-----
400 °C	650 nm	582 nm	630 nm	-----
600 °C	-----	-----	-----	-----

6.3 Conclusion

Thermal annealing treatment modified the optical and structural properties of nanocomposite thin film. For thin film with Ag content (24%, 33%, 45%), LSPR was observed and one can tune the LSPR position of LSPR by thermal annealing. However, for concentration 56 at.%, thermal treatment to the thin film was unable to modify the LSPR position compared to the other results. Better results were observed for the 33 at.% and 45 at.%. For 45 at.% two LSPR was observed after annealing at 200 °C which may be due to the multimode absorption of nanoparticles having non-symmetric shape other than a sphere. Modifications in structural properties were observed which was also responsible for the redshift observed in the thin film samples. The defects were created when an Ag atom leaves its position and agglomerate to the other atoms. These defects cause for the large redshift observed after annealing because its refractive index was also changing. Annealing at 600 °C shows sublimation of silver nanoparticle for all the nanocomposite thin film. The absorption for all composition downs drastically by silver sublimation.

Chapter Seven

Conclusion and future aspects

7.1 Conclusion

This thesis summarizes the investigation carried out on the synthesis of nanocomposite thin film. This thesis also includes their modifications by SHI beam irradiation and thermal annealing. Following the conclusion has been made from the study

1. Synthesize the nanocomposite thin film by RF co-sputtering technique. High concentration of silver deposited in the matrix of TiO_2 . The band gap of the thin film varies with the concentration of Ag in the host matrix.
2. Absorption increases with increasing silver concentration, a very broad SPR and low intense observed for the concentration Ag 45% without giving any heat treatment to them.
3. Interparticle separation was affected by the concentration of silver, which leads to the interparticle plasmonic coupling effect. Plasmonic coupling shows broad absorption in the visible region.
4. Crystallinity of host matrix TiO_2 was affected by the filler material silver. Crystallinity decreases while increasing the concentration.
5. Interaction of Ag nanoparticle with TiO_2 was observed, which decrease the electron-hole recombination rate.
6. Nanocomposite thin film prepared by ion implantation technique shows LSPR in the visible region. This confirms the formation of Ag nanoparticle and Ag in metallic form. Whereas in literature oxidation of silver was reported by ion implantation.
7. Defects created during implantation and interaction of Ag nanoparticle with the TiO_2 reveals the decrease in the recombination rate of electron and hole pair.
8. The SHI irradiation tunes the LSPR properties due to Ag nanoparticle, whereas the host matrix remained almost unaffected by it which was due to the difference in thermal conductivity of Ag and TiO_2 .
9. Significant changes were observed in the morphological properties of nanocomposite thin film after irradiation average particle size and interparticle separation increased which results in enhancement of LSPR intensity. The

broadening in the SPR due to the interparticle coupling effect as the concentration of silver is high to ignore this effect.

10. FDTD simulation has been done for both pristine and irradiated thin film. This simulation explains results more explicit about the existence and position of LSPR.
11. For a high concentration of Ag (45%, 56%) in TiO₂ SHI irradiation act as an effective technique to modifies optical properties.
12. Thermally annealed nanocomposite thin film provides structural changes in the matrix of TiO₂ as well as in the crystallinity of silver nanoparticle. The silver nanoparticle agglomerate to form a bigger particle. The combined effect of crystalline TiO₂ and silver nanoparticle size directly affect the position and intensity of LSPR.
13. Mixed phases (anatase and rutile) of TiO₂ observed in the thermal annealing process.
14. Sublimation of Ag was observed after annealing at 600 °C.
15. SHI irradiation provides far better control over the modification of tuning of LSPR for the high concentration of silver, whereas thermal annealing provides good control over the crystallinity of matrix in nanocomposite thin film.

7.2 Future aspects

There are many unresolved properties, modification and ideas about nanocomposite thin film, on this we can extend this study in future.

1. The SPR can be tuned by SHI irradiation, by the selection of irradiation parameter one can tune the SPR properties. Multiple SPR (as obtained in thermal annealing) can be obtained by selecting irradiation condition.
2. More than one filler material (more than one noble metal) can be used to achieve desired optical properties, which can not be achieved by single noble metal. One can study the effect of irradiation on optical properties.
3. The core-shell nanoparticle can also be used as filler material to achieve the new level of optical properties which needs optimization of synthesis and irradiation parameter.
4. This nanocomposite can show potential application as photoelectrochemical water splitting¹⁵¹ and photocatalytic properties¹⁵².

5. The different structure of nanocomposite thin film can be tried for the modification of optical properties by ion irradiation.

References

- (1) Peter, R. *Nanoscience and technology*; World Scientific.
- (2) Narlikar, A. V.; Fu, Y. Y. *The Oxford handbook of nanoscience and nanotechnology*; Oxford University press, 2010; Vol. 3.
- (3) Manzoor, U.; Islam, M.; Tabassam, L.; Rahman, S. U. *Phys. E Low-dimensional Syst. Nanostructures* **2009**, *41* (9), 1669–1672.
- (4) Smith, A. M.; Nie, S. *Acc. Chem. Res.* **2010**, *43* (2), 190–200.
- (5) Chellammal, S.; Manivannan, S. *Adv. Mater. Res.* **2014**, *1051*, 17–20.
- (6) Haug, H.; Koch, S. W. *Quantum Theory of the Optical and Electronic Properties of Semiconductors*; WORLD SCIENTIFIC, 2009.
- (7) Bhattacharya, S.; Samanta, S. K. *Chem. Rev.* **2016**, *116* (19), 11967–12028.
- (8) Sahay, R.; Reddy, V. J.; Ramakrishna, S. *Int. J. Mech. Mater. Eng.* **2014**, *9* (1), 25.
- (9) Müller, K.; Bugnicourt, E.; Latorre, M.; Jorda, M.; Echegoyen Sanz, Y.; Lagaron, J.; Miesbauer, O.; Bianchin, A.; Hankin, S.; Bölz, U.; Pérez, G.; Jesdinszki, M.; Lindner, M.; Scheuerer, Z.; Castelló, S.; Schmid, M. *Nanomaterials* **2017**, *7* (4), 74.
- (10) Camargo, P. H. C.; Satyanarayana, K. G.; Wypych, F. *Mater. Res.* **2009**, *12* (1), 1–39.
- (11) Guisbiers, G. *Nanoscale Res. Lett.* **2010**, *5* (7), 1132–1136.
- (12) Guisbiers, G.; Mejía-Rosales, S.; Leonard Deepak, F.; a-Rosales, S.; Leonard Deepak, F. *J. Nanomater.* **2012**, *2012*, 1–2.
- (13) Singh, M.; Lara, S.; Tlali, S. *J. Taibah Univ. Sci.* **2016**.
- (14) Schmid, G.; Decker, M.; Ernst, H.; Fuchs, H.; Grünwald, W.; Grunwald, A.; Hofmann, H.; Rathgeber, W.; Simon, U.; Wyrwa, D. *Small Dimensions and Material Properties A Definition of Nanotechnology*; 2003.
- (15) Buzea, C.; Pacheco, I. Springer, New Delhi, 2017; pp 3–45.
- (16) Twardowski, T. E. *Introduction to nanocomposite materials : properties, processing, characterization*; Destech Publications, Inc, 2007.
- (17) Manocha, L. M.; Valand, J.; Patel, N.; Warriar, A.; Manocha, S. *Indian J. Pure Appl. Phys.* **2006**, *44*, 135–142.
- (18) Calebrese, C.; Hui, L.; Schadler, L.; Nelson, J. *IEEE Trans. Dielectr. Electr. Insul.* **2011**, *18* (4), 938–945.

- (19) Singhal, R.; Agarwal, D. C.; Mishra, Y. K.; Kabiraj, D.; Mattei, G.; Pivin, J. C.; Chandra, R.; Avasthi, D. K. *J. Appl. Phys.* **2010**, *107* (10), 103504.
- (20) Singhal, R.; Agarwal, D. C.; Mishra, Y. K.; Singh, F.; Pivin, J. C.; Chandra, R.; Avasthi, D. K. *J. Phys. D. Appl. Phys.* **2009**, *42* (15), 155103.
- (21) Tjong, S. C. *Mater. Sci. Eng. R Reports* **2006**, *53* (3–4), 73–197.
- (22) Quaresimin, M.; Salviato, M.; Zappalorto, M. *Compos. Part B Eng.* **2012**, *43* (5), 2290–2297.
- (23) Crosby, A. J.; Lee, J. *Polym. Rev.* **2007**, *47* (2), 217–229.
- (24) Liu, Y.; Wu, H.; Chen, G. *Polym. Compos.* **2016**, *37* (4), 1190–1197.
- (25) Tjong, S. C. *Carbon nanotube reinforced composites : metal and ceramic matrices*; Wiley-VCH, 2009.
- (26) Yang, J. K.; Park, D. J.; Kim, J.; Chang, S. Y.; Lee, C. H.; Sekino, T.; Niihara, K.; Choa, Y. H. *Key Eng. Mater.* **2006**, *317–318*, 869–872.
- (27) Sun, Y.-F.; Liu, S.-B.; Meng, F.-L.; Liu, J.-Y.; Jin, Z.; Kong, L.-T.; Liu, J.-H. *Sensors* **2012**, *12* (12), 2610–2631.
- (28) Tripathy, A.; Pramanik, S.; Manna, A.; Shasmin, H.; Radzi, Z.; Abu Osman, N. *Sensors* **2016**, *16* (12), 2029.
- (29) Bao, D. *Nippon seramikusu kyokai gakujuitsu ronbunshi* **2009**, *117* (9), 929–934.
- (30) Petronella, F.; Fanizza, E.; Mascolo, G.; Locaputo, V.; Bertinetti, L.; Martra, G.; Coluccia, S.; Agostiano, A.; Curri, M. L.; Comparelli, R. *J. Phys. Chem. C* **2011**, *115* (24), 12033–12040.
- (31) Xiao Feng Zhang, *, †; Gabriel Harley, †, ‡ and; Lutgard C. De Jonghe †, ‡. **2005**.
- (32) Magnfält, D.; Melander, E.; Boyd, R. D.; Kapaklis, V.; Sarakinos, K. *J. Appl. Phys.* **2017**, *121* (17), 171918.
- (33) Sergeev, V. P.; Panin, V. E.; Psakhie, S. G.; Chernyavskii, A. G.; Svechkin, V. P.; Khristenko, Y. F.; Kalashnikov, M. P.; Voronov, A. V. 2014; pp 563–566.
- (34) Tang, Y.; Zeng, X.; Liang, J. *J. Chem. Educ.* **2010**, *87* (7), 742–746.
- (35) Tang, Y.; Zeng, X.; Liang, J. *J. Chem. Educ.* **2010**, *87* (7), 742–746.
- (36) Jatschka, J.; Dathe, A.; Csáki, A.; Fritzsche, W.; Stranik, O. *Sens. Bio-Sensing Res.* **2016**, *7*, 62–70.
- (37) Victoria, S. *J. Bacteriol. Parasitol.* **2012**, *3* (7).
- (38) Canovi, M.; Lucchetti, J.; Stravalaci, M.; Re, F.; Moscatelli, D.; Bigini, P.;

- Salmona, M.; Gobbi, M. *Sensors (Basel)*. **2012**, *12* (12), 16420–16432.
- (39) Reza, A.; M. Noor, A. S.; Maarof, M. In *Plasmonics - Principles and Applications*; InTech, 2012.
- (40) Li, Y.; Liu, X.; Lin, Z. *Food Chem.* **2012**, *132* (3), 1549–1554.
- (41) Horvath, H. J. *Quant. Spectrosc. Radiat. Transf.* **2009**, *110* (11), 787–799.
- (42) Kumar, C. S. S. R. (Challa S. S. R. . *UV-VIS and photoluminescence spectroscopy for nanomaterials characterization*; Springer, 2013.
- (43) Chen, X.; Mao, S. S. *Chem. Rev.* **2007**, *107* (7), 2891–2959.
- (44) Zhu, T.; Gao, S.-P. *J. Phys. Chem. C* **2014**, *118* (21), 11385–11396.
- (45) Liu, Q.-J.; Ran, Z.; Liu, F.-S.; Liu, Z.-T. *J. Alloys Compd.* **2015**, *631*, 192–201.
- (46) Gopinath, K.; Kumaraguru, S.; Bhakayaraj, K.; Thirumal, S.; Arumugam, A. *Superlattices Microstruct.* **2016**, *92* (20), 100–110.
- (47) Gopinath, K.; Kumaraguru, S.; Bhakayaraj, K.; Thirumal, S.; Arumugam, A. *Superlattices Microstruct.* **2016**, *92*, 100–110.
- (48) Matsuoka, M.; Anpo, M.; Matsuoka, M.; Anpo, M. In *Handbook of Green Chemistry*; Wiley-VCH Verlag GmbH & Co. KGaA: Weinheim, Germany, 2010.
- (49) Chou, W.-C.; Liu, W.-J. In *2016 International Conference on Electronics Packaging (ICEP)*; IEEE, 2016; pp 664–668.
- (50) Roy, P.; Kim, D.; Lee, K.; Spiecker, E.; Schmuki, P. *Nanoscale* **2010**, *2* (1), 45–59.
- (51) Fan, K.; Zhang, W.; Peng, T.; Chen, J.; Yang, F. *J. Phys. Chem. C* **2011**, *115* (34), 17213–17219.
- (52) Sun, Y.; Wang, G.; Yan, K. *Int. J. Hydrogen Energy* **2011**, *36* (24), 15502–15508.
- (53) Chiarello, G. L.; Dozzi, M. V.; Selli, E. *J. Energy Chem.* **2017**, *26* (2), 250–258.
- (54) Lee, J.-K.; Choi, D.-S.; Jang, I.; Choi, W.-Y. *Int. J. Nanomedicine* **2015**, *10*, 1145–1154.
- (55) Kulkarni, M.; Mazare, A.; Gongadze, E.; Perutkova, Š.; Kralj-Iglič, V.; Milošev, I.; Schmuki, P.; A Iglič; Mozetič, M. *Nanotechnology* **2015**, *26* (6), 62002.
- (56) Bagheri, S.; Muhd Julkapli, N.; Bee Abd Hamid, S. *Sci. World J.* **2014**, *2014*, 1–21.

- (57) Zhang, C.; He, H.; Tanaka, K. *Appl. Catal. B Environ.* **2006**, *65* (1–2), 37–43.
- (58) Braun, J. H.; Baidins, A.; Marganski, R. E. *Prog. Org. Coatings* **1992**, *20* (2), 105–138.
- (59) Luttrell, T.; Halpegamage, S.; Tao, J.; Kramer, A.; Sutter, E.; Batzill, M. *Sci. Rep.* **2015**, *4* (1), 4043.
- (60) Zhang, J.; Zhou, P.; Liu, J.; Yu, J. *Phys. Chem. Chem. Phys.* **2014**, *16* (38), 20382–20386.
- (61) González, A. L.; Noguez, C.; Beránek, J.; Barnard, A. S. *J. Phys. Chem. C* **2014**, *118* (17), 9128–9136.
- (62) Kiss, F. D.; Miotto, R.; Ferraz, A. C. *Nanotechnology* **2011**, *22* (27), 275708.
- (63) Liu, R.; Wang, P.; Wang, X.; Yu, H.; Yu, J. *J. Phys. Chem. C* **2012**, *116* (33), 17721–17728.
- (64) Guo, G.; Yu, B.; Yu, P.; Chen, X. *Talanta* **2009**, *79* (3), 570–575.
- (65) Wu, W.-Y.; Hsu, C.-F.; Wu, M.-J.; Chen, C.-N.; Huang, J.-J. *Appl. Phys. A* **2017**, *123* (5), 357.
- (66) Hwang, S. H.; Song, H.; Lee, J.; Jang, J. *Chem. - A Eur. J.* **2014**, *20* (40), 12974–12981.
- (67) Zhang, H.; Chen, G. *Environ. Sci. Technol.* **2009**, *43* (8), 2905–2910.
- (68) Wei, L.; Wang, H.; Wang, Z.; Yu, M.; Chen, S. *RSC Adv.* **2015**, *5* (91), 74347–74352.
- (69) Evanoff, D. D.; Chumanov, G. *J. Phys. Chem. B* **2004**, *108* (37), 13957–13962.
- (70) Jain, I. P.; Agarwal, G. *Surf. Sci. Rep.* **2011**, *66* (3–4), 77–172.
- (71) Avasthi, D. K.; Mehta, G. K. *Swift Heavy Ions for Materials Engineering and Nanostructuring*; Springer Series in Materials Science; Springer Netherlands: Dordrecht, 2011; Vol. 145.
- (72) Prakash, J.; Kumar, P.; Harris, R. A.; Swart, C.; Neethling, J. H.; van Vuuren, A. J.; Swart, H. C. *Nanotechnology* **2016**, *27* (35), 355707.
- (73) Borges, J.; Rodrigues, M. S.; Kubart, T.; Kumar, S.; Leifer, K.; Evaristo, M.; Cavaleiro, A.; Apreutesei, M.; Pereira, R. M. S.; Vasilevskiy, M. I.; Polcar, T.; Vaz, F. *Thin Solid Films* **2015**, *596*, 8–17.
- (74) Lin, Z.; Wang, X.; Liu, J.; Tian, Z.; Dai, L.; He, B.; Han, C.; Wu, Y.; Zeng, Z.; Hu, Z. *Nanoscale* **2015**, *7* (9), 4114–4123.
- (75) Gültekin, A. *Mater. Sci.* **2014**, *20* (1), 10–14.
- (76) Ahmed, M. H.; Keyes, T. E.; Byrne, J. A. *J. Photochem. Photobiol. A Chem.*

2013, 254, 1–11.

- (77) Viana, M. M.; Mohallem, N. D. S.; Miquita, D. R.; Balzuweit, K.; Silva-Pinto, E. *Appl. Surf. Sci.* **2013**, 265, 130–136.
- (78) Ahmed, M. H.; Keyes, T. E.; Byrne, J. A.; Blackledge, C. W.; Hamilton, J. W. *J. Photochem. Photobiol. A Chem.* **2011**, 222 (1), 123–131.
- (79) Torrell, M.; Cunha, L.; Kabir, M. R.; Cavaleiro, A.; Vasilevskiy, M. I.; Vaz, F. *Mater. Lett.* **2010**, 64 (23), 2624–2626.
- (80) Torrell, M.; Machado, P.; Cunha, L.; Figueiredo, N. M.; Oliveira, J. C.; Louro, C.; Vaz, F. *Surf. Coatings Technol.* **2010**, 204 (9–10), 1569–1575.
- (81) Sangpour, P.; Hashemi, F.; Moshfegh, A. Z. *J. Phys. Chem. C* **2010**, 114 (33), 13955–13961.
- (82) Uddin, M. J.; Cesano, F.; Scarano, D.; Bonino, F.; Agostini, G.; Spoto, G.; Bordiga, S.; Zecchina, A. *J. Photochem. Photobiol. A Chem.* **2008**, 199 (1), 64–72.
- (83) Xu, J.; Sun, Y.; Zhao, Y.; Huang, J.; Chen, C.; Jiang, Z. *Int. J. Photoenergy* **2007**, 2007.
- (84) Tian, Y.; Tatsuma, T. *J. Am. Chem. Soc.* **2005**, 127 (20), 7632–7637.
- (85) Hou, X.; Ma, H.; Liu, F.; Deng, J.; Ai, Y.; Zhao, X.; Mao, D.; Li, D.; Liao, B. *J. Hazard. Mater.* **2015**, 299, 59–66.
- (86) Xu, J. X.; Xiao, X. H.; Stepanov, A. L.; Ren, F.; Mei, F.; Wu, W.; Cai, G. X.; Jiang, C. Z. *Nucl. Instruments Methods Phys. Res. Sect. B Beam Interact. with Mater. Atoms* **2013**, 307, 373–376.
- (87) Stepanov, A. L. *Rev. Adv. Mater. Sci.* **2012**, 30 (2), 150–165.
- (88) Chang, Y.-Y.; Shieh, Y.-N.; Kao, H.-Y. *Thin Solid Films* **2011**, 519 (20), 6935–6939.
- (89) Verma, A.; Srivastav, A.; Sharma, D.; Banerjee, A.; Sharma, S.; Satsangi, V. R.; Shrivastav, R.; Avasthi, D. K.; Dass, S. *Nucl. Instruments Methods Phys. Res. Sect. B Beam Interact. with Mater. Atoms* **2016**, 379, 255–261.
- (90) Chakravadhanula, V. S. K.; Mishra, Y. K.; Kotnur, V. G.; Avasthi, D. K.; Strunskus, T.; Zaporotchenko, V.; Fink, D.; Kienle, L.; Faupel, F. *Beilstein J. Nanotechnol.* **2014**, 5 (1), 1419–1431.
- (91) Rath, H.; Dash, P.; Som, T.; Satyam, P. V.; Singh, U. P.; Kulriya, P. K.; Kanjilal, D.; Avasthi, D. K.; Mishra, N. C. *J. Appl. Phys.* **2009**, 105 (7), 1–5.
- (92) Chakravadhanula, V. S. K.; Mishra, Y. K.; Kotnur, V. G.; Hrkac, T.; Kienle,

- L.; Avasthi, D. K.; Fink, D.; Zaporotchenko, V.; Faupel, F. In *CLEO/Europe - EQEC 2009 - European Conference on Lasers and Electro-Optics and the European Quantum Electronics Conference*; IEEE, 2009; Vol. 3, pp 1–1.
- (93) Mishra, Y. K.; Avasthi, D. K.; Kulriya, P. K.; Singh, F.; Kabiraj, D.; Tripathi, A.; Pivin, J. C.; Bayer, I. S.; Biswas, A. *Appl. Phys. Lett.* **2007**, *90* (7), 1–4.
- (94) Borges, J.; Kubart, T.; Kumar, S.; Leifer, K.; Rodrigues, M. S.; Duarte, N.; Martins, B.; Dias, J. P.; Cavaleiro, A.; Vaz, F. *Thin Solid Films* **2015**, *580*, 77–88.
- (95) Kumar, M.; Kumar, T.; Avasthi, D. K. *Scr. Mater.* **2015**, *105* (MAY), 46–49.
- (96) Reymond-Laruinaz, S.; Saviot, L.; Potin, V.; Lopes, C.; Vaz, F.; Marco De Lucas, M. C. *Thin Solid Films* **2014**, *553*, 138–143.
- (97) Adochite, R. C.; Munteanu, D.; Torrell, M.; Cunha, L.; Alves, E.; Barradas, N. P.; Cavaleiro, A.; Riviere, J. P.; Le Bourhis, E.; Eyidi, D.; Vaz, F. *Appl. Surf. Sci.* **2012**, *258* (8), 4028–4034.
- (98) Torrell, M.; Kabir, R.; Cunha, L.; Vasilevskiy, M. I.; Vaz, F.; Cavaleiro, A.; Alves, E.; Barradas, N. P. *J. Appl. Phys.* **2011**, *109* (7).
- (99) Torrell, M.; Cunha, L.; Cavaleiro, A.; Alves, E.; Barradas, N. P.; Vaz, F. *Appl. Surf. Sci.* **2010**, *256* (22), 6536–6542.
- (100) Kelly, P. . J.; Arnell, R. . D. *Vacuum* **2000**, *56* (3), 159–172.
- (101) Musil, J.; Baroch, P.; Vlček, J.; Nam, K. H.; Han, J. G. *Thin Solid Films* **2005**, *475* (1–2 SPEC. ISS.), 208–218.
- (102) Doolittle, L. R. *Nucl. Instruments Methods Phys. Res. Sect. B Beam Interact. with Mater. Atoms* **1985**, *9* (3), 344–351.
- (103) Cullity, B. D.; Stock, S. R. *Elements of X-ray diffraction, 3rd edition*; 2001.
- (104) Degen, T.; Sadki, M.; Bron, E.; König, U.; Nénert, G. *Powder Diffr.* **2014**, *29* (S2), S13–S18.
- (105) Stenzel, O. *The Physics of Thin Film Optical Spectra*; Springer Series in Surface Sciences; Springer International Publishing: Cham, 2016; Vol. 44.
- (106) Mathew, S.; Kumar Prasad, A.; Benoy, T.; Rakesh, P. P.; Hari, M.; Libish, T. M.; Radhakrishnan, P.; Nampoore, V. P. N.; Vallabhan, C. P. G. *J. Fluoresc.* **2012**, *22* (6), 1563–1569.
- (107) Kaufmann, E. N. *Characterization of Materials*; 2008.
- (108) Ohring, M.; Ohring, M. In *Materials Science of Thin Films*; 2002; pp 559–640.
- (109) Mishra, Y. K.; Mohapatra, S.; Singhal, R.; Avasthi, D. K.; Agarwal, D. C.;

- Ogale, S. B. *Appl. Phys. Lett.* **2008**, 92 (4), 43107.
- (110) Epifani, M.; Giannini, C.; Tapfer, L.; Vasanelli, L. *J. Am. Ceram. Soc.* **2004**, 83 (10), 2385–2393.
- (111) Lambert, M.; May, A.; Akkan, C. K.; Agarwal, N.; Aktas, O. C. *Mater. Lett.* **2014**, 137, 405–408.
- (112) Hariprasad, E.; Radhakrishnan, T. P. *Langmuir* **2013**, 29 (42), 13050–13057.
- (113) Gupta, S. M.; Tripathi, M. *Chinese Sci. Bull.* **2011**, 56 (16), 1639–1657.
- (114) Yang, Y.; Flatebo, C.; Liang, J.; Dong, P.; Yuan, J.; Wang, T.; Zhang, J.; Chen, W.; Wu, J.; Ajayan, P. M.; Ci, L.; Li, Q.; Lou, J. *Appl. Mater. Today* **2016**, 3, 57–62.
- (115) Rathee, D.; Arya, S. K.; Kumar, M. *Front. Optoelectron. China* **2011**, 4 (4), 349–358.
- (116) Euvananont, C.; Junin, C.; Inpor, K.; Limthongkul, P.; Thanachayanont, C. *Ceram. Int.* **2008**, 34 (4), 1067–1071.
- (117) Richards, B. S. *Sol. Energy Mater. Sol. Cells* **2003**, 79 (3), 369–390.
- (118) He, C.; Yu, Y.; Hu, X.; Larbot, A. *Appl. Surf. Sci.* **2002**, 200 (1–4), 239–247.
- (119) Mogensen, K. B.; Kneipp, K. *J. Phys. Chem. C* **2014**, 118 (48), 28075–28083.
- (120) Zhang, H.; Banfield, J. F. *J. Mater. Chem.* **1998**, 8 (9), 2073–2076.
- (121) Ghosh, S. K.; Pal, T. *Chem. Rev.* **2007**, 107 (11), 4797–4862.
- (122) Mayer, K. M.; Hafner, J. H. *Chem. Rev.* **2011**, 111 (6), 3828–3857.
- (123) Alam, M. J.; Cameron, D. C. *J. Sol-Gel Sci. Technol.* **2002**, 25 (2), 137–145.
- (124) Zuo, J. *Appl. Surf. Sci.* **2010**, 256 (23), 7096–7101.
- (125) Gupta, K.; Singh, R. P.; Pandey, A.; Pandey, A. *Beilstein J. Nanotechnol.* **2013**, 4 (1), 345–351.
- (126) Su, C.; Liu, L.; Zhang, M.; Zhang, Y.; Shao, C. *CrystEngComm* **2012**, 14 (11), 3989.
- (127) Pal, U.; Pea, O. In *Ion Implantation*; InTech, 2012.
- (128) Meldrum, A.; Haglund, R. F. J.; Boatner, L. A.; White, C. W. *Adv. Mater.* **2001**, 13 (19), 1431–1444.
- (129) Gardner, P. R. *Mater. Des.* **1987**, 8 (4), 210–219.
- (130) Meldrum, A.; Lopez, R.; Magruder, R. H.; Boatner, L. A.; White, C. W. Springer Berlin Heidelberg, 2009; pp 255–285.
- (131) Noguez, C. *J. Phys. Chem. C* **2007**, 111 (10), 3806–3819.
- (132) Kelly, K. L.; Kelly, K. L.; Coronado, E.; Zhao, L.; Coronado, E.; Schatz, G. C.;

- Zhao, L. L.; Schatz, G. C. *J. Phys. Chem. B* **2003**, *107* (3), 668–677.
- (133) Yu, B.; Leung, K. M.; Guo, Q.; Lau, W. M.; Yang, J. *Nanotechnology* **2011**, *22*, 115603.
- (134) Mishra, Y. K.; Jebril, S.; Agarwal, D. C.; Mohapatra, S.; Singhal, R.; Avasthi, D. K.; Adelung, R. *CLEO/Europe - EQEC 2009 - Eur. Conf. Lasers Electro-Optics Eur. Quantum Electron. Conf.* **2009**, *189* (2006), 43107.
- (135) Hou, X.; Ma, H.; Liu, F.; Deng, J.; Ai, Y.; Zhao, X.; Mao, D.; Li, D.; Liao, B. *J. Hazard. Mater.* **2015**, *299*, 59–66.
- (136) Chang, Y.-Y.; Shieh, Y.-N.; Kao, H.-Y. *Thin Solid Films* **2011**, *519* (20), 6935–6939.
- (137) Xu, J. X.; Xiao, X. H.; Stepanov, A. L.; Ren, F.; Mei, F.; Wu, W.; Cai, G. X.; Jiang, C. Z. *Nucl. Instruments Methods Phys. Res. Sect. B Beam Interact. with Mater. Atoms* **2013**, *307*, 373–376.
- (138) Möller, W.; Eckstein, W. *Nucl. Instruments Methods Phys. Res. Sect. B Beam Interact. with Mater. Atoms* **1984**, *2* (1–3), 814–818.
- (139) Chen, Y.; Cao, Y.; Bai, Y.; Yang, W.; Yang, J. *Symp. A Q. J. Mod. Foreign Lit.* **1997**, *15* (4), 1442–1444.
- (140) Zhang, Y.; Schwartzberg, A. M.; Xu, K.; Gu, C.; Zhang, J. Z. Burda, C., Ellingson, R. J., Eds.; International Society for Optics and Photonics, 2005; Vol. 5929, p 592912.
- (141) Kim, D. J.; Kim, D. S.; Cho, S.; Kim, S. W.; Lee, S. H.; Kim, J. C. *Int. J. Thermophys.* **2004**, *25* (1), 281–289.
- (142) <https://www.lumerical.com/tcad-products/fdtd/>
- (143) Davis, K. O.; Jiang, K.; Habermann, D.; Schoenfeld, W. V. *IEEE J. Photovoltaics* **2015**, *5* (5), 1265–1270.
- (144) Jain, P. K.; El-Sayed, M. A. *Chem. Phys. Lett.* **2010**, *487* (4–6), 153–164.
- (145) Hagemann, H.-J.; Gudat, W.; Kunz, C. *J. Opt. Soc. Am.* **1975**, *65* (6), 742.
- (146) Link, S.; El-Sayed, M. A. *Int. Rev. Phys. Chem.* **2000**, *19* (3), 409–453.
- (147) Klabunde, K. J. *Nanoscale materials in chemistry*; Wiley-Interscience, 2001.
- (148) Huang, X.; El-Sayed, M. A. *J. Adv. Res.* **2010**, *1* (1), 13–28.
- (149) Martin, P. *Thin Solid Films* **2001**, *394* (1–2), 1–14.
- (150) Sharma, H.; Singhal, R.; Siva Kumar, V. V.; Asokan, K. *Appl. Phys. A* **2016**, *122* (12), 1010.
- (151) Alenzi, N.; Liao, W.-S.; Cremer, P. S.; Sanchez-Torres, V.; Wood, T. K.;

Ehlig-Economides, C.; Cheng, Z. *Int. J. Hydrogen Energy* **2010**, *35*, 11768–11775.

- (152) Zhao, Z.-J.; Hwang, S. H.; Jeon, S.; Hwang, B.; Jung, J.-Y.; Lee, J.; Park, S.-H.; Jeong, J.-H. *Sci. Rep.* **2017**, *7* (1), 8915.

Publication:-

1. Sharma, H., Singhal, R., Siva Kumar, V.V. et al. Appl. Phys. A (2016) 122: 1010. Structural, optical and electronic properties of Ag–TiO₂ nanocomposite thin film. <https://doi.org/10.1007/s00339-016-0552-3>
2. Synthesis of Ag metallic nanoparticles by 120 KeV Ag⁻ ion implantation in TiO₂. Radiation Effects and Defects in Solids, 172:11-12, 896-902.
3. SHI Irradiation induced modifications of Plasmonic properties of Ag-TiO₂ thin film and study using FDTD simulation. (Accepted)

Bio-Data

Himanshu Sharma

Contact No. 8279587476

Email ID: himanshumnit86@gmail.com



Academic Qualification:

1. Ph.D Pursuing, Department of Physics, Malaviya National Institute of Technology (MNIT), Jaipur.
3. M.Sc Physics from C.C.S. University, Meerut 2011
4. B.Sc (PCM) from University of Rajasthan, Jaipur 2007

Publications:

1. "Structural, optical and electronic properties of Ag–TiO₂ nanocomposite thin film" Himanshu Sharma, R. Singhal, V. V. Siva Kumar, K. Asokan Appl. Phys. A (2016) 122:1010. <https://doi.org/10.1007/s00339-016-0552-3>
2. "Synthesis of Ag metallic nanoparticles by 120 keV Ag⁻ ion implantation in TiO₂ matrix" Himanshu Sharma, Rahul Singhal, Radiation Effects & Defects In Solids, 2018, 172:11-12, 896-902, <https://doi.org/10.1080/10420150.2017.1418349>
3. "SHI Irradiation induced modifications of Plasmonic properties of Ag-TiO₂ thin film and study using FDTD simulation" Himanshu Sharma, Rahul Singhal, Material Science Poland. (Accepted).

Conferences/ Workshops/ School/ Academic Programs Attended:

1. Presented a poster in national workshop on "Advanced Functional Materials (AFM-2014)" on 5th September 2014 held at MNIT Jaipur organized jointly by Department of Metallurgical and Materials Engineering and Department of Physics MNIT Jaipur.
2. Attended DST - SERB school on "Ion Interaction with Matter" will be held during March 2 - 21, 2015 at Department of Physics, Saurashtra University, Rajkot (Gujarat).

3. Participated in INUP familiarization workshop on “Nanofabrication Technologies” held at Malaviya National Institute of Technology Jaipur from 26-27 August 2016.

Personal Particulars:

Name: Himanshu Sharma
Date of Birth: 10-Dec-1986
Father’s Name: Mr. Budh Prakash Sharma
Mother’s Name: Mrs. Pushpa Sharma
Nationally: Indian
Permanent Address: Himanshu Sharma
229, Subhash Puri, Kankarkhera
Dist. – Meerut, Uttar Pradesh (India)
Pin- 250001.
Mob: 8279587476

Declaration

I hereby declare that all information provided above are correct.

Place: Jaipur

Date

(Himanshu Sharma)